# Year-Round Supraglacial Lake Monitoring in Northeast Greenland Using Synthetic Aperture Radar

by

Connor Dean
BSc., University of Victoria, 2022

A thesis submitted in partial fulfillment of the requirements for the degree of

MASTER OF SCIENCE

in the Department of Geography



We acknowledge and respect the Lək̓ʷəŋən (Songhees and Xʷsepsəm/Esquimalt) Peoples on whose territory the university stands, and the Lək̓ʷəŋən and W̱SÁNEĆ Peoples whose historical relationships with the land continue to this day.

# Supervisory Committee

**Year-Round Supraglacial Lake Monitoring in Northeast Greenland Using Synthetic Aperture Radar**

by

Connor Dean
BSc., University of Victoria, 2022

## Supervisory Committee

---

Dr. Randall K. Scharien, Supervisor
Department of Geography

---

Dr. Maycira Costa, Department Member
Department of Geography

## Abstract

The Greenland Ice Sheet (GrIS) is one of largest contemporary contributors to global mean sea-level rise. Observations beginning in 1972 indicate its mass loss is accelerating and projected to continue throughout the century. Mitigating its impacts could require trillions of dollars, while the resulting higher seas may place hundreds of millions of people below the high-tide line by 2100. Mass loss of the GrIS results from surface mass balance (SMB) and dynamic ice discharge. Supraglacial lakes affect both processes by modulating albedo and surface melt water routing and contribute to enhanced basal sliding by delivering melt water to the bed during drainage events.

Firstly, a novel C-band synthetic aperture radar (SAR) based methodology using Sentinel-1 and the RADARSAT Constellation Mission (RCM) data was developed to detect winter supraglacial lake drainage events at Nioghalvfjerdsbræ (79NG) and Zachariæ Isstrøm (ZI) in Northeast (NE) Greenland at high temporal resolutions. This enabled a decade long analysis of the spatiotemporal frequency of winter drainage events from 2014/2015 to 2023/2024 seasons. Winter drainage events occur during each winter season with substantial inter-seasonal variability. Approximately half of all winter drainage events (46 out of 90) were involved in cascade events. Short increases in ice velocity resulting from drainage events were observed, while there was little evidence for the ability of drainage events to drive seasonal or interannual ice velocity increases. These findings advance our understanding of winter supraglacial lake dynamics, a phase that remains far less studied than melt-season processes.

Secondly, we conducted a melt season analysis to identify optimal SAR parameters for supraglacial lake detection in C- and L-band. Pairs of fully-polarimetric and compact-polarimetric images were compared and found that SAR parameters VV/HH and the linear polarization ratio (LPR) enabled enhanced capability for the detection of supraglacial lakes relative to single polarization channels. Additionally, L-band VV/HH and LPR exhibited a unique signature for snow and ice lids that bury portions of lakes, discriminating them from open water and surrounding ice sheet.

# Table of Contents

## List of Tables

# List of Figures

## Acknowledgements

As I look back on my master’s thesis, I can’t help but think of what a whirlwind it’s been! It’s hard to grasp everything I’ve learned and all the amazing experiences I’ve had.

Firstly, I would like to thank Randy for everything he has done as my supervisor over the past several years. Beginning with my Honours thesis and continuing through to my master's, his support and openness to letting me explore topics that sparked my curiosity helped me find my way into the field of ice-sheet hydrology and supraglacial lakes. Without this support, I’m not sure I would have ever discovered my place in glaciology. His expertise in microwave remote sensing and his emphasis on mastering the fundamentals and geophysics that underpin remote sensing have given me confidence in my current and future scientific endeavors. In addition to his guidance, I am grateful for all the experiences he facilitated, including the privilege to attend numerous international conferences and participate in the Sikunnguaq field campaign in Qikiqtarjuaq, Baffin Island. I am truly thankful for everything he has taught me.

I am thankful to those with whom I had the opportunity to work alongside. Dr. Ian Willis and Dr. Rebecca Dell from the Scott Polar Research Institute, your feedback and guidance on the glaciological aspects of my work have been invaluable. Jackie from the Lancaster University, our shared passion and curiosity for supraglacial lakes continues a source of motivation.

To the current and former members of the ICELab including Kali McDougall, Aikaterini Tavri, Grant Macdonald, Adrià Blanco-Cabanillas, Kalum Delaney, and Neil Brubacher, your friendship, support, and camaraderie have helped drive me to see this thesis through to the finish.

To all my family, thank you for always being loving and a constant source of happiness. To my Mom and Dad, who nurtured my curiosity from a young age and instilled in me a passion for the well-being of our planet. To my Omi, who supported and guided me through the many challenging forks in the road of life and times when I felt uncertain. If it weren’t for you all, I may not have achieved what I have today.

To Kali, for being there each step of the way from the low to high points. Without you, this journey would’ve been much more difficult (and far less exciting).

# Chapter 1. Introduction

## 1.1. Research context

Observations of the Greenland Ice Sheet (GrIS) in recent decades indicate an accelerating trend in mass loss, leading to increased contributions to global sea level rise (Mouginot et al., 2019; Shepherd et al., 2020). While the ice sheet remained in a near-equilibrium state from 1972 to 1992, it has since experienced consistent decadal mass losses across all regions. Cumulative mass loss from the GrIS results from two main components: surface mass balance, which reflects the net difference between snow accumulation and ablation, and ice dynamics, which includes ice loss through calving into the ocean. The inherent complexity involved in accurately modeling and observing these processes has introduced significant uncertainties in projections of future contributions to sea-level rise (Slater et al., 2020).

As a critical contributor to contemporary global sea-level rise, the GrIS holds enough ice to elevate global sea level by approximately 7 meters. Observational data since 1992 indicate an accelerated rate of mass loss, with recent projections suggesting the GrIS could contribute roughly 274 mm to global sea-level rise by the end of this century (Box et al., 2022). This contribution is greater than those projected from the Antarctic ice sheet (Otosaka et al., 2023). A rise in sea level of just 10 to 20 cm could double the frequency of extreme water-level events in coastal regions and major cities worldwide (Vitousek et al., 2017). The financial implications of mitigating sea-level rise exceeding 1 meter are substantial, potentially exceeding 70 billion dollars annually in flood protection infrastructure alone, posing a direct threat to the livelihoods of hundreds of millions of people (Hinkel et al., 2014). Between approximately 190 million people under low carbon emission scenarios and roughly 630 million under high carbon emission scenarios are projected to live below the high-tide line by 2100 (Kulp & Strauss, 2019). To improve predictions of Greenland's future mass loss and its impacts, it is essential to continue enhancing our understanding of the processes driving SMB and ice dynamic losses (Hanna et al., 2024).

Supraglacial lakes represent a significant component of the complex mass balance of the GrIS, affecting ice loss through both SMB and ice dynamics. Each melt season, meltwater from snow percolates downward until encountering saturated firn or impermeable ice layers, halting further infiltration (Irvine-Fynn et al., 2011; Pitcher & Smith, 2019). This meltwater accumulates and subsequently incises underlying ice or firn, forming supraglacial rivers whose patterns depend on surface slope and ice characteristics (Hambrey, 1977; Mantelli et al., 2015; Yang et al., 2016). These rivers often transport meltwater into depressions, where supraglacial lakes develop over periods of days to weeks (Smith et al., 2017; Yang et al., 2019; Smith et al., 2021). The locations of these depressions, and thus lakes, are primarily governed by basal topography, surface roughness, ice velocity, and ice thickness (Lampkin & VanderBerg, 2011; Ignéczi et al., 2018). Such depressions typically remain fixed over time, with the highest concentrations occurring in northeastern and eastern Greenland, predominantly within 50 km of the ice margin (Ignéczi et al., 2016).

Regarding SMB, supraglacial lakes influence the GrIS by altering surface albedo and affecting surface meltwater routing (Tedesco et al., 2012; Smith et al., 2015). Albedo decreases on the ice sheet surface are driven largely by the accumulation of light absorbing impurities and the exposure of bare ice (Tedesco et al., 2016). Supraglacial lakes, which have roughly half the albedo of surrounding snow and ice, further amplify this reduction (Tedesco, 2014; Arthur et al., 2020). Tedesco et al. (2012) observed ablation rates beneath two supraglacial lakes of approximately 6 cm/day, compared to approximately 3 cm/day on adjacent ice surfaces. Furthermore, supraglacial lakes influence meltwater routing through the process of hydrofracturing, which can form moulins which are vertical conduits connecting the ice surface to the bed (Smith et al., 2015; Hoffman et al., 2018). In areas with high moulin density, surface meltwater efficiently drains into subglacial systems, facilitating ice mass loss (Smith et al., 2015; Yang et al., 2021). Conversely, regions lacking moulins typically direct surface meltwater toward the ice sheet margins (Li et al., 2022). Meltwater delivered to the subglacial environment via moulins induces increased melt rates within subglacial channels (Young et al., 2022). Undrained supraglacial lakes may also refreeze, thereby limiting mass loss from the ice sheet (Koenig et al., 2015; Schröder et al., 2020; Benedek & Willis, 2021). Due to their critical roles in controlling melt rates and meltwater routing pathways, supraglacial lakes are important to monitor and accurately represent in modeling efforts aimed at quantifying GrIS dynamics and mass balance.

In addition to their role in the supraglacial hydrologic system, supraglacial lakes also significantly influence ice dynamics by affecting ice flow velocities by influencing the subglacial hydrologic system. Supraglacial lakes have been documented to drain through two primary mechanisms: a slower process where lakes overflow their banks, gradually incising drainage channels over periods greater than one day, and a rapid process occurring in less than one day, triggered by hydrofracturing (Das et al., 2008; Tedesco et al., 2013). During rapid drainage, meltwater is swiftly transferred to the bed of the ice sheet, causing elevated basal water pressures. These elevated pressures can enhance basal lubrication, consequently increasing ice velocity. Furthermore, the hydrofracturing process frequently results in the formation of moulins, which may persist for several years (Banwell et al., 2016; Hoffman et al., 2018; Poinar & Andrews, 2021). These moulins serve as important surface-to-bed connections that continue to influence ice dynamics beyond the initial drainage event. Consequently, the impacts of rapid lake drainage on ice flow velocities are not limited to the short-term response following immediate meltwater injection but extend over subsequent years as supraglacial streams continue to deliver meltwater into these persistent moulins.

The majority of research on supraglacial lakes to date has utilized optical remote sensing imagery (Sundal et al., 2009; Johansson et al., 2013; Morriss et al., 2013; Fitzpatrick et al., 2014; Yang et al., 2021; Otto et al., 2022). The widespread availability of optical sensors, such as Landsat, MODIS, and Sentinel-2, often with extensive archives spanning several decades, has provided researchers with a comprehensive understanding of supraglacial lake formation and melt-season phenology. Numerous studies have applied optical data to examine lake drainage behaviour and melt-season evolution (Selmes et al., 2011; Morriss et al., 2013; Fitzpatrick et al., 2014; Wang & Sugiyama, 2024), investigate multi-decadal trends in drainage behaviour and distribution (Howat et al., 2013; Otto et al., 2022; Fan et al., 2025), and support detailed observations and modeling of surface melt rates in Greenland (Yang et al., 2019; Yang et al., 2021). Although these satellite-based studies have significantly advanced our fundamental understanding of supraglacial lakes, there remain gaps and observational biases introduced by limitations inherent to optical remote sensing, such as cloud cover, lakes hidden by snow- and ice-covered surfaces, and polar darkness. Specific limitations include potential underestimation of observed drainage events in years with greater cloudiness, underestimation of lake areas, and the inability to monitor lake dynamics during the polar winter (Cooley & Christofferson, 2017; Schröder et al., 2020; Benedek & Willis, 2021).

More recently, synthetic aperture radar (SAR) has emerged as a valuable tool that complements optical remote sensing by addressing the limitations imposed by optical systems. SAR sensors provide observations independent of daylight conditions and are capable of penetrating cloud cover, making them particularly well-suited to studying regions frequently obscured by clouds or experiencing polar night. The rise in the use of SAR imagery has led to novel insights into supraglacial lake dynamics beyond the melt season. Recent studies employing SAR data have documented instances of winter drainage events (Benedek & Willis, 2021) and enabled the mapping of buried lake extents during winter months (Miles et al., 2017; Dunmire et al., 2021; Zheng et al., 2023), thereby expanding our understanding of supraglacial lake processes and highlighting the potential of SAR to fill observational gaps left by optical sensors.

While SAR sensors have provided valuable new insights into supraglacial lake dynamics, sensing approaches differ fundamentally from optical sensors, presenting unique challenges in lake detection. SAR sensors operate by emitting pulses of polarized electromagnetic radiation in the microwave region of the spectrum and measuring the return signal, typically in the same polarization or a perpendicular polarization relative to the transmitted pulse. This returned signal, known as backscatter intensity, depends on factors such as target geometry, surface roughness, dielectric properties, and sensor-specific parameters such as frequency, polarization, and incidence angle. Recent studies utilizing SAR for supraglacial lake observations have highlighted difficulties arising from the similarity of backscatter signatures between lakes and surrounding ice sheet facies during various melt stages (Johansson & Brown, 2012; Miles et al., 2017; Schröder et al., 2020). Furthermore, the influence of the SAR incidence angle remains poorly constrained, causing many studies to rely solely on imagery from specific orbit paths to minimize geometric uncertainties. Consequently, the temporal resolution of these analyses is restricted by the repeat acquisition intervals of specific satellite orbits, often exceeding six days for satellites such as Sentinel-1 (Schröder et al., 2020; Benedek & Willis, 2021; Dirscherl et al., 2021). Additionally, SAR-based studies of supraglacial lakes have primarily utilized sensors operating at C-band frequency, including the ENVISAT Advanced Synthetic Aperture RADAR (ASAR) and, predominantly, Sentinel-1. This reliance on C-band sensors has resulted in a gap in understanding the potential improvements in detection capabilities offered by other frequencies such as L-band. Due to its longer wavelength, L-band SAR provides greater penetration depth under both dry and wet surface conditions, potentially enhancing the discrimination of lakes from surrounding ice facies. With upcoming missions such as the NASA-ISRO SAR (NISAR) in 2025 and the ESA Radar Observing System for Europe–L-band (ROSE-L) in 2028, L-band SAR is anticipated to become a crucial data source for supraglacial lake studies.

### 1.2. Research objectives

The primary objective of this research is to advance the application of SAR data for monitoring supraglacial lakes during both the melt and winter seasons. The research is structured around specific objectives corresponding to lake properties associated with each seasonal context. Firstly, for the winter season when supraglacial lake behaviour is least understood, this research aims to:

1. develop a novel methodology enabling the detection of winter supraglacial lake drainage events at high temporal resolution by integrating SAR imagery from multiple orbit paths and sensor acquisition modes at C-band; and
2. apply the methodology in 1 to examine the frequency and spatiotemporal distribution of winter supraglacial lake drainage events in NE Greenland and their impacts on ice sheet dynamics.

Secondly, for the melt season where robust optical methods exist but observations are often limited by cloud cover and persistent snow or ice lids, the research aims to:

3. identify optimal SAR backscatter and texture parameters from compact-polarimetric and fully-polarimetric C-band and L-band acquisitions for reliable detection of supraglacial lakes including those covered by ice lids; and
4. evaluate the capability of decision tree-based machine learning classifier algorithms, specifically Random Forest and XGBoost, for accurately classifying supraglacial lakes.

### 1.3. Thesis structure

This thesis consists of four chapters. Chapter 1 introduces the research, providing essential context regarding supraglacial lakes and their significance in ice sheet environments, and outlines the research objectives. Chapter 2, titled "A decade of winter supraglacial lake drainage across Northeast Greenland using C-band SAR," focuses on objectives 1 and 2 in Section 1.2. Chapter 3, titled "Melt season C- and L-band SAR backscatter observations of supraglacial lakes in Northeast Greenland," addresses objectives 3 and 4 in Section 1.2. Chapter 4 summarizes the main findings and suggests potential directions for future research. Chapter 2 will be submitted for review in the journal The Cryosphere. Chapter 3 will be submitted for review in the journal Remote Sensing of Environment.

# Chapter 2. A decade of winter supraglacial lake drainage across Northeast Greenland using C-band SAR

## 2.1. Abstract

his study presents the first comprehensive, multi-year analysis of winter supraglacial lake drainage frequency on the GrIS, detailing cascading drainage events, examining links to melt-season conditions, and evaluating implications for ice dynamics. Supraglacial lakes can rapidly drain, delivering meltwater to the ice-sheet bed, increasing basal water pressure, lubrication, and ice flow. Such drainage events are well-documented across Greenland during the melt season using optical satellite imagery. Recent research using satellite and airborne radar data indicates that many supraglacial lakes persist into winter and also drain, potentially affecting ice dynamics similarly to melt-season drainages. Here, we use Sentinel-1 and RADARSAT Constellation Mission (RCM) C-band SAR imagery from ten consecutive winters (2014/2015–2023/2024). We develop a normalization method to integrate images from varying acquisition geometries, enabling high-temporal-resolution monitoring. Our analysis identifies 90 winter drainage events across 55 unique lakes, with significant interannual variability: a maximum of 18 events occurred in the 2018/2019 winter and a minimum of four events in both the 2020/2021 and 2021/2022 winters. Drainages were most frequent in early winter, decreasing as winter progressed. Approximately half of the winter drainages were part of 13 cascading events, each involving two to seven lakes over distances up to ~33 km. Comparisons with preceding melt-season conditions reveal negative correlations between winter drainage frequency and both melt-season intensity and melt-season drainage frequency. Ice velocity analyses over the ten-year period show no sustained seasonal or annual velocity increases clearly associated with winter drainages, although isolated increases on shorter (6–12-day) timescales were observed.

## 2.2. Introduction

In recent decades contributions from the GrIS to global-mean sea level rise have accelerated through SMB and glacier dynamics losses (Mouginot et al., 2019; Shepherd et al., 2020; Box et al., 2022). Supraglacial lakes hereafter lakes, anticipated to expand further inland under climate change (Leeson et al., 2015; Ignéczi et al., 2016, Fan et al., 2025), contribute to SMB losses by modifying the ice sheet surface albedo (Tedesco et al., 2012). In the GrIS ablation zone, lakes form during the melt season and drain either slowly by overtopping their banks and incising an outlet channel, or rapidly (within 24 hours) via hydrofracture

(Sundal et al., 2009; Selmes et al., 2011; Tedesco et al., 2013). Drainage events that are caused by hydrofracture drive melt water through cracks formed by stresses at the surface of the ice sheet to the subglacial system, where it can enhance basal lubrication and increase ice velocities in the summer and, particularly in inland regions away from the glacier margins, over annual timescales (Das et al., 2008; Doyle et al., 2014; Stevens et al., 2015; Christoffersen et al., 2018; Hoffman et al., 2018). At the end of the melt season, lakes that remain can either freeze completely (Selmes et al, 2011; Koenig et al., 2015; Miles et al., 2017) or, as recent research has shown, drain during the winter and trigger ice dynamical responses similar to those observed during the melt season (Schröder et al., 2020; Benedek & Willis, 2021; Maier et al., 2023).

The remoteness and spatiotemporal variability of lakes has made earth observation satellites a crucial source for tracking changes and conducting process studies. Early studies employed optical remote-sensing satellites for phenological analyses (Sneed & Hamilton, 2007; Sundal et al., 2009; Selmes et al., 2011; Johansson et al., 2013; Morriss et al., 2013). This class of sensors remains popular due to the extensive historical archives available. For example, the LANDSAT program dates back to 1972, and the two Moderate Resolution Imaging Spectroradiometer (MODIS) sensors, aboard Terra and Aqua spacecraft, have been providing observations since 2000 and 2002, respectively, allowing for multi-year and decadal studies (Liang et al., 2012; Williamson et al, 2017; Gledhill & Williamson, 2018; Poinar & Andrews, 2021; Otto et al., 2022). More recent optical sensors, notably the Sentinel-2A & 2B constellation, have both a high-temporal resolution (daily) and a high spatial resolution (10 m), a combination that was not possible with previous sensors (Dirscherl et al., 2020; Hochreuther et al., 2021). Additionally, optical sensor data can be used to estimate lakes volume (Georgiou et al., 2009; Fitzpatrick et al., 2014; Legleiter et al., 2014; Pope et al., 2016; Williamson et al., 2017; Williamson et al., 2018). While satellite optical imagery has been instrumental in establishing our understanding of lakes during the melt season, the winter period remains understudied since the presence of snow and ice lids, and lack of solar illumination, render optical sensors ineffective. Furthermore, even during melting conditions, optical datasets are susceptible to temporal aliasing of drainage dates, introducing bias into the interpretation of drainage mechanisms (Cooley & Christoffersen et al., 2018; Stevens et al., 2024). Addressing these gaps is crucial for understanding the year-round impact of lakes on ice dynamics.

SAR sensors emit electromagnetic (EM) radiation in the microwave region of the EM spectrum, allowing the illumination of targets without sunlight, as well as penetration through clouds and surface snow and ice layers. Incident radar pulses interact with ice sheet surface and shallow subsurface ‘volume’ features, resulting in a backscattered signal that is influenced by geometry, roughness, dielectrics, and SAR system parameters including frequency, polarization, and incidence angle (Ulaby et al., 1984; Hallikainen et al., 1986; König et al., 2001). Since the launch of the Copernicus Sentinel-1 mission, involving Sentinel-1A in 2014 and Sentinel-1B in 2016, the number of SAR-based studies of lakes has seen a marked increase, in part due to the open availability of Copernicus data. To date, the C-band frequency of Sentinel-1 and predecessor SAR missions including Envisat (European Space Agency) and RADARSAT-1/2 (Canadian Space Agency), among others, is the frequency used most often for winter lake studies. Early techniques involved manual delineation and interpretation of winter SAR scenes (Johansson & Brown, 2012; Poinar et al., 2015). Other approaches have used histogram thresholding to map lake extent, first by using a single threshold across one scene (Miles et al., 2017), later enhanced through an adaptive thresholding approach in a pan-Greenland study (Zheng et al., 2023). Other recent lake mapping approaches have included convolutional neural networks (CNNs) trained on dual-polarization Sentinel-1 HH and HV imagery, where H represents horizontal polarization and V represents vertical (and combinations refer to transmit-receive polarizations), for regional and ice sheet-scale lake distribution studies in both winter and summer seasons (Dirscherl et al., 2021; Dunmire et al., 2021; Jiang et al., 2022).

Other studies have used time series of Sentinel-1 HH and HV backscatter to analyze lake behaviour (Dunmire et al., 2020; Schröder et al., 2020; Benedek & Willis, 2021; Hossain et al., 2024). Approaches for detecting drainage differ from those mapping distribution in that they rely on anomalies in backscatter values between subsequent images. Schröder et al. (2020) mapped lake extent using a Bayesian classification scheme applied to time-series of Sentinel-1 HH and HH-HV band images and also detected winter drainage events by tracking backscatter anomalies. Dunmire et al. (2020) paired *in-situ* ground penetrating radar observations with Sentinel-1 HH backscatter to identify the winter drainage of a buried lake on the Antarctic ice sheet. Over southwest GrIS, Benedek & Willis (2021) conducted a multi-year study of winter drainage events by identifying anomalous increases in Sentinel-1 HV backscatter using a statistical thresholding method. More recently, Hossain et al. (2024) developed a Gaussian Mixture Model-based time series classification to characterize different lake evolution behaviors, including drainage. These approaches classifies lakes based on behavior types rather than explicitly identifying the timing of drainage events. With the exception of Hossain et al. (2024), who included data from multiple orbits and applied a temporal smoothing filter to reduce variability, all of these studies controlled for the influence of SAR incidence angle on backscatter intensity by selecting imagery from a single orbit, thus sacrificing temporal resolution. For Sentinel-1 the repeat time is 6-days with a two-satellite constellation (Sentinel-1A and Sentinel-1B), and 12-days with a single satellite. While drainage events well detected with temporal resolutions of 6 to 12 days with Sentinel-1 (Schröder et al., 2020; Benedek & Willis, 2021), accurately resolving the timing of individual drainage events and determining the sequence of cascading events requires higher temporal resolution. Cascading events are chain reactions of lake drainages that often unfold over just a few days, in which the rapid injection of meltwater from one lake into subglacial pathways generates transient stresses capable of forming a crevasse (Christoffersen et al., 2018). Such events have been documented in multiple regions of the GrIS and are likely a common mechanism of lake drainage (Liang et al., 2012; Fitzpatrick et al., 2014; Otto et al., 2022; Maier et al., 2023). High temporal resolution is also necessary for detecting rapid drainage events and distinguishing these from slow drainage.

In this study, we investigate winter drainage events in Northeast Greenland at sub-daily temporal resolution by combining Sentinel 1 images with data from the RADARSAT Constellation Mission (RCM), a three-satellite C-band SAR system launched in 2019. We enhance temporal resolution by applying a novel incidence angle normalization technique that enables the integration of SAR images from multiple overlapping orbits. This method minimizes backscatter variability associated with incidence angle differences - both between orbits and within individual images - allowing for consistent analysis across a wider range of acquisitions.

Using this approach, we identify winter lake drainage events spanning the 2014/2015 to 2023/2024 winter seasons, detecting 90 events in total. These include individual lakes that drained as many as six times over the ten-year period, as well as cascading drainage sequences involving up to seven interconnected lakes. We examine interannual variability in the frequency of winter drainage events and assess whether preceding summer melt conditions - such as melt intensity and the number of rapid summer drainages - influence the likelihood of winter drainage. For cascading events, we analyze their sequence, spatiotemporal dynamics, prevalence, and evaluate their proximity to modeled subglacial drainage pathways. Finally, we investigate whether winter drainage events influence ice flow dynamics, assessing both short-term (< 6 to 12 days) velocity changes and longer-term impacts on seasonal and annual ice motion.

### 2.3. Study area

The study region in Northeast (NE) Greenland includes elevations below 1500 m on the marine-terminating outlet glaciers Nioghalvfjerdsbræ (79NG) and Zachariæ Isstrøm (ZI) according to their basins defined by Mouginot & Rignot, 2019 (Figure 2.1). The total basin areas of 79NG and ZI are 112,677 km² and 92,576 km², of which 16,306 km² and 8,704 km², respectively, lie below 1500 m elevation (Mouginot and Rignot, 2019). Near terminus elevations of 79NG and ZI are each approximately 100 m. This area contains one of the most inland-reaching ice streams of the GrIS, transporting ice from the interior to 79NG and ZI at near-terminus velocities of ~1350 m/yr and 1800 m/yr, respectively (Joughin et al., 2016; Hvidberg et al., 2020; Fig. 2.1). During the melt season, from early June to late August, expansive networks of supraglacial rivers and lakes form at elevations between ~400 and 1500 m (Sundal et al., 2009; Lu et al., 2021; Hochreuther et al., 2021; Turton et al., 2021; Kanzow et al., 2025). NE Greenland currently holds approximately 18% of the total GrIS lake volume, with projections indicating this may increase to 30-35% by the end of the century (Ignéczi et al., 2016). Studies using data acquired by the Center for Remote Sensing of Ice Sheets (CReSIS) ultra-wideband Snow Radar flown during the Operation Ice Bridge campaign detected numerous lakes throughout 79NG and ZI persisting into late winter, some remaining buried for several years (Koenig et al., 2015; Lampkin et al., 2020). Schröder et al. (2020) used Sentinel-1 to document widespread occurrences of lakes into winter months and several suspected drainage events in the region. Drainage events have also been documented in the region during the melt season (Neckel et al., 2020; Hochreuther et al., 2021; Humbert et al., 2025; Lutz et al., 2025). The region has widespread ice slabs, and no documented firn aquifers (Miège et al., 2016; Miller et al., 2022; Culberg et al., 2024).

### 2.4. Data and methods

#### 2.4.1. Optical imagery

Lake locations were determined from Landsat 8 and 9 Operational Land Imager (OLI) sensor imagery acquired between late July and end of August in each year spanning 2014 to 2023. Tier 1 Level 1 Precision Terrain (L1TP) processed images were acquired and filtered to include only those with less than 50% cloud cover. Final selections were made manually after visual inspection for those with minimal cloud presence. Lake masks were created using a version of the Normalized Difference Water Index modified for the ice sheet environment ($NDWI_{ice}$; Yang & Smith., 2013):

$$NDWI_{ice} = \frac{BLUE - RED}{BLUE + RED} \qquad (1)$$

where BLUE and RED correspond to OLI bands 2 and 4. $NDWI_{ice}$ threshold values between 0.25 and 0.4 are considered sufficient to detect deep bodies of water and minimize slush detection (Yang & Smith., 2013; Miles et al., 2017; Williamson et al., 2018). We chose a threshold of 0.4 empirically, finding it excluded most of slush while including deep bodies of water during manual inspection of RGB (true-colour) images. Landsat RGB image composites were inspected manually to mask out false positive lake locations due to cloud-covered areas and shadowed ice-margin areas. Rectilinear and curvilinear features were identified and removed to avoid the inclusion of supraglacial rivers (Lampkin & VanderBerg, 2011; Gledhill & Williamson, 2018). The ArcticDEM (Porter et al., 2023) was then used to mask out elevations above 1500 m, and the MEaSUREs Greenland Ice Mapping Project (GIMP) grounded ice mask was used to mask out land areas (Howat et al., 2014; Howat, 2017). Figure 2.2 shows a workflow diagram of all steps including data processing and subsequent analysis.

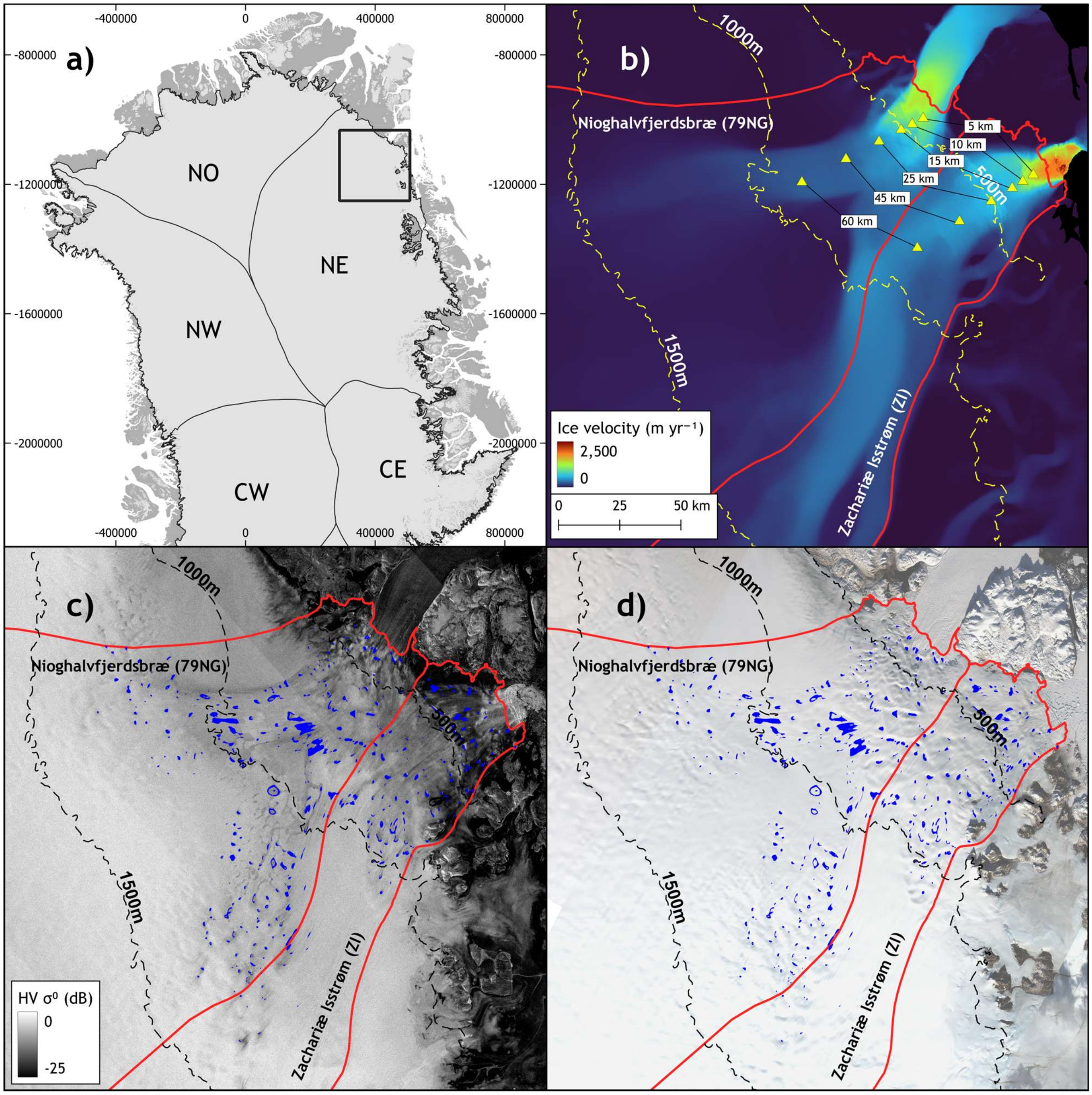


**Figure 2.1**. (a) Study area location in NE Greenland. (b) MEaSUREs multi-year ice sheet velocity mosaic (1995 - 2015) with the sampling points used to sample the monthly velocity data from 2015 to 2024, which are shown in Figure 2.12 (Joughin et al., 2016). (c) Sentinel-1 extra wide mode HV image on October 10th, 2016. (d) Landsat RGB mosaic from September 25th, 2016. Blue polygons are the 10-year melt season lake mask. Red polygons are the outlines of Nioghalvfjerdsbræ (79NG) and Zachariæ Isstrøm (ZI) glaciers (Mouginot & Rignot, 2019).

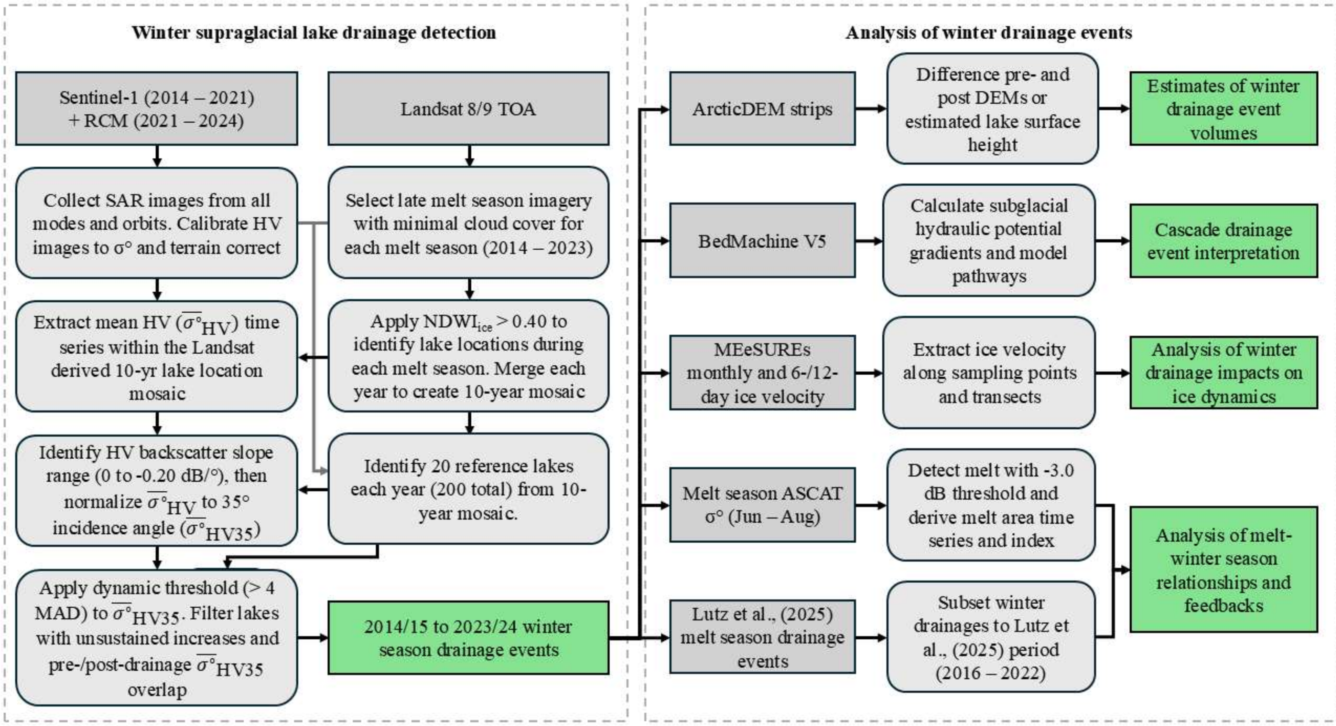


**Figure 2.2.** Workflow diagram of winter lake drainage event detection and subsequent analyses.

### 2.4.2. Synthetic aperture radar imagery

We used C-band SAR images from both Sentinel-1 and RCM, both operating in near-polar, sun-synchronous orbits and having the same center frequency of 5.405 GHz (Table 2.1). Sentinel-1A was launched in 2014, followed by Sentinel-1B in 2016; when operating together they were spaced 180° apart on the same orbit, providing a 6-day revisit time. Prior to the launch of Sentinel-1B, and after its failure in December 2021, Sentinel-1A had a 12-day revisit time. RCM, composed of three identical satellites spaced 120° apart on the same orbit, was launched in 2019, primarily as a successor to the RADARSAT-2 mission and to support the core needs of the Canadian Government (Kroupnik et al., 2021). Following the failure of Sentinel-1B, the RCM acquisition plan was altered to compensate for the data loss, significantly increasing the RCM acquisition frequency over the GrIS. For this study, Sentinel-1 images are used between 2014 and 2021, after which RCM imagery is used. An overview of the sensors can be seen in Table 2.1.

To characterize winter lake drainage activity, we analysed imagery spanning each September to May from 2014/15 through 2023/24. This time frame captures the onset of freeze up - when lakes may be obscured by ice lids and fresh snow - and extends until the onset of surface melt water production. While this period is slightly longer than that used in a comparable study in southwest Greenland (Benedek & Willis, 2021), it is appropriate given the shorter melt season in Northeast Greenland and prior evidence from optical imagery indicating typical lake burial timing (Sundal et al., 2009; Turton et al., 2021; Lutz et al., 2023).

All available Sentinel-1 Ground Range Detected (GRD) images collected in Interferometric Wide swath (IW) and Extra Wide swath (EW) modes were acquired from the Alaska Satellite Facility (Table 2.1). All RCM GRD images collected in ScanSAR medium, high, and low noise modes were obtained from the Earth Observation Data Management System (EODMS) operated by Natural Resources Canada (Table 2.1). To reduce redundancy from repeated ascending or descending passes on the same day, we excluded images acquired less than two hours apart. After this filtering, the mean duration between lake observations across all winter seasons ranged from 2.7 days in 2014/2015 to 0.7 days in 2017/2018.

We pre-processed all images using the following workflow implemented in the ESA Sentinel Application Platform (SNAP): the HV image band (see Section 3.3 for rationale) was calibrated to the normalized radar cross-section sigma naught ($\sigma°_{HV}$), then terrain corrected using the ArcticDEM Version 4.1 (Porter et al., 2023) and projected to NSIDC Sea Ice Polar Stereographic North (EPSG:3413) with a 40 m pixel spacing using the nearest neighbor method for resampling. The pre-processed data is referred to $\overline{\sigma°}_{HV}$ hereafter.

**Table 2.1.** Overview of C-band SAR sensors and modes used.

| **Sensor & mode** | **Sentinel-1 IW** | **Sentinel-1 EW** | **RCM ScanSAR50** | **RCM ScanSAR100** | **RCM SCLN** |
|---|---|---|---|---|---|
| Frequency (GHz) | 5.405 GHz | 5.405 GHz | 5.405 GHz | 5.405 GHz | 5.405 GHz |
| Polarization | HH + HV | HH + HV | HH + HV | HH + HV | HH + HV |
| Resolution (*r* & *a*) | 20.0 m x 5.0 m | 40.0 m x 20.0 m | 20.0 m x 20.0 m | 40.0 m x 40.0 m | 40.0 m x 40.0 m |
| GRD pixel spacing | 10.0 m | 40.0 m | 20.0 m | 40.0 m | 40.0 m |
| Swath width | 250 km | 400 km | 350 km | 500 km | 350 km |
| Operational years | April 2014 - present | April 2014 - present | June 2019 - present | June 2019 - present | June 2019 - present |

### 2.4.3. Detecting drainage events

C-band SAR, with a penetration depth of approximately 1 to 3 meters in glacial media (Rignot et al., 2001), can be used to detect subsurface meltwater in buried lakes. Lake drainage events were detected using the HV polarization channel due to its greater sensitivity to volume scattering and deeper penetration compared to the HH channel (Fischer et al., 2020), making it a preferred choice in lake studies (Miles et al., 2017; Benedek & Willis, 2021; Zheng et al., 2023; Hossain et al., 2024). Following a drainage event, the lakebed composed of firn and glacial ice is revealed, both of which have a lower dielectric constant compared to lake water. Furthermore, the lakebed has a higher surface roughness compared to water or the surrounding firn or ice, due to the collapsed lid (Russel, 1993). These changes lead to a significant increase in backscatter. This contrasts with the low backscatter from winter lakes buried beneath snow and ice lids, which is due to the high dielectric constant of water combined with low surface roughness, resulting in dominant specular scattering (Hallikainen et al., 1986).

#### 2.4.3.1. Melt season supraglacial lake mask

To detect winter drainage events, we identified lakes from optical imagery using $NDWI_{ice}$ in each melt season from 2014 to 2023 (Section 2.4.1) and then merged all summer boundaries into a single 10-year mosaic (Figure 2.3c and 2d). For each individual lake in this mosaic, we tracked mean $\overline{\sigma°}_{HV}$ values over time. By using a 10-year mosaic rather than separate yearly maps, we account for lakes that remain partially or entirely buried for multiple years (Koenig et al., 2015; Lampkin et al., 2020), minimizing the risk of missing winter drainage events (Benedek & Willis, 2021). Examples of individual lake extents can be seen in Figure 2.3. Lakes smaller than 0.1 $km^2$ were excluded due to low signal-to-noise ratios. We suspect that winter drainage of these smaller lakes is unlikely, and that they are more prone to freeze-through because of their smaller volumes and shallower depths (Lampkin et al., 2020; Law et al., 2020).

#### 2.4.3.2. Incidence angle correction

The Sentinel-1 and RCM image dataset includes acquisitions obtained along various orbits, which introduces incidence-angle-induced variations in $\overline{\sigma°}_{HV}$ for the same target. In both sea ice and ice sheet studies, this effect has been described for various frequencies, transmit-receive polarizations, and second-order texture parameters using linear models that normalize a SAR image swath to a common incidence angle (Mahmud et al., 2018; Scharien & Nasonova, 2022; Culberg et al., 2024). We used the least-squares linear regression data fitting approach to determine the slopes of $\overline{\sigma°}_{HV}$ versus incidence angle at monthly intervals, within the boundaries of 10 non-draining and 10 empty reference lakes from each winter season for a total of 200 across the 10-years. The reference lakes ranged in size from 95 to 14,678 pixels, with an average of 1,290 pixels. These lakes were identified using a combination of manual interpretation of winter-period SAR images; melt season optical images showing evidence of lake lid collapse (Schröder et al., 2020; Benedek & Willis, 2021; Maier et al., 2023); and uncorrected winter backscatter time series.

To correct incidence-angle-induced variations in $\overline{\sigma°}_{\mathrm{HV}}$ that arise from seasonal geophysical changes through winter and differences between pre- and post-drainage conditions, we applied a multi-slope normalization method. This method identifies the optimal slope value by constraining it within the full range of values. The optimal slope is determined by calculating the variance across all potential slopes ranging from 0 to -0.20 dB/1°, in increments of -0.005, using a 7-observation moving window. The slope resulting in the lowest variance is then applied to normalize the mean backscatter to 35° for the observation at the center of the window (Equation 2).

$$\overline{\sigma}^{\circ}_{\mathrm{HV35}} = \overline{\sigma}^{\circ}_{\mathrm{HV}} + \mathrm{Slope}_{\mathrm{opt}} \cdot (\theta_{\mathrm{ref}} - \theta_{\mathrm{meas}}) \tag{2}$$

Where $\overline{\sigma°}_{\mathrm{HV35}}$ is the incidence angle corrected backscatter value, $\overline{\sigma°}_{\mathrm{HV}}$ is the uncorrected backscatter, $\mathrm{Slope}_{\mathrm{opt}}$ is the optimal slope $\overline{\sigma°}_{\mathrm{HV35}}$ determined using the seven-observation variance window, $\theta_{\mathrm{ref}}$ is the reference incidence angle of 35°, and $\theta_{\mathrm{meas}}$ is the incidence angle at which the observation was made. Examples of $\overline{\sigma°}_{\mathrm{HV}}$ and $\overline{\sigma°}_{\mathrm{HV35}}$ time series are shown in Figure 2.3.

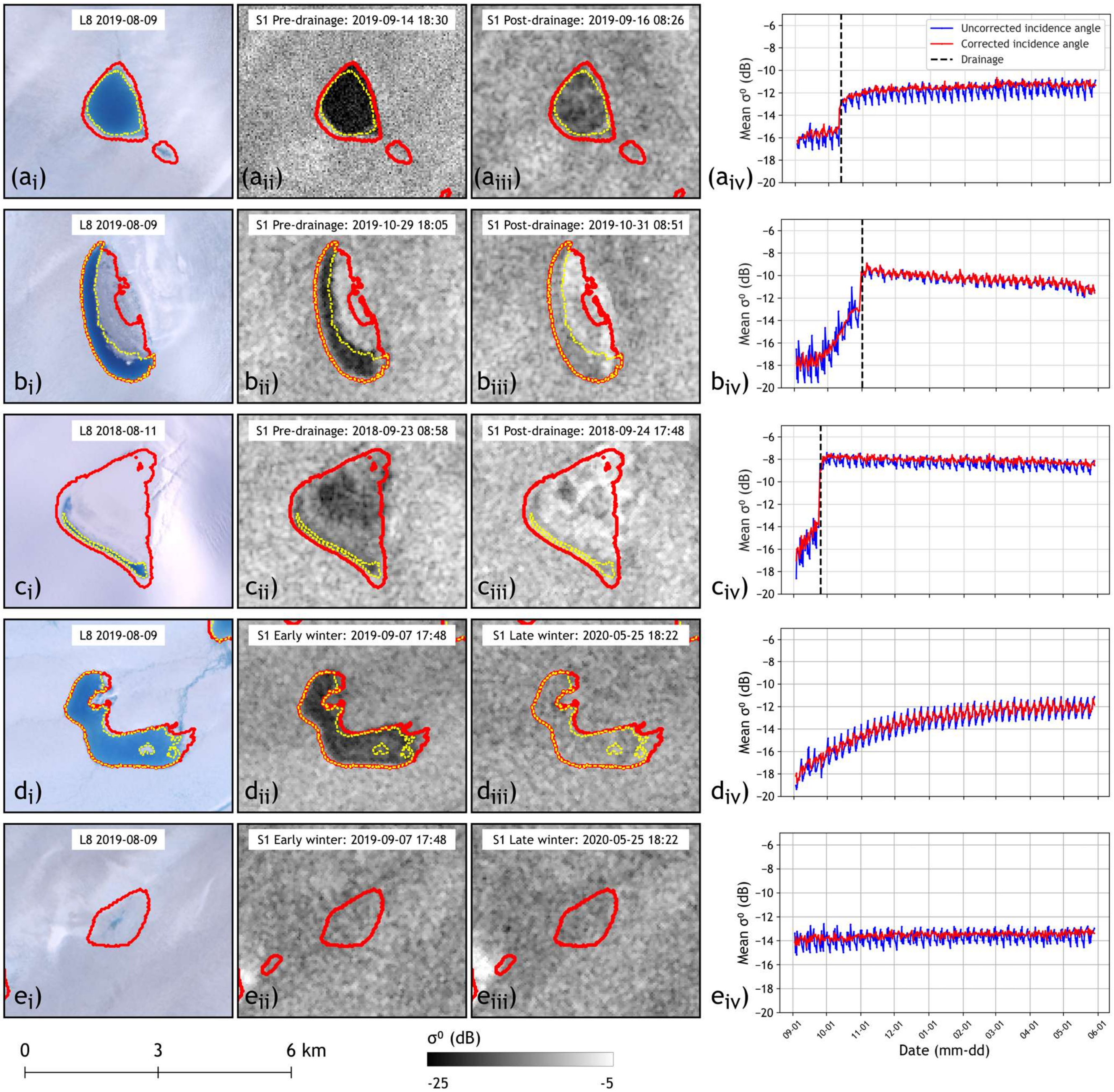


**Figure 2.3.** Examples of winter lake behaviour and their Sentinel-1 HV backscatter signal: (a) a subaerial supraglacial lake, which drains; (b) a lake partially covered by a perennial ice lid, which drains; (c) a lake with little to no surface expression, which drains; (d) a subaerial supraglacial lake that freezes through; and (e) a lake basin that remains empty of meltwater during the melt season and subsequent winter. Column (i) shows Landsat RGB images. C-band SAR images are shown in columns (ii) and (iii). The 10-year Landsat-derived melt season lake mosaic masks (red polygon) and annual masks (yellow dotted polygon) are overlaid on the satellite images. Column (iv) shows the mean uncorrected and corrected $\sigma^o_{HV}$ backscatter time series from the start (September 1) to the end (May 31) of winter.

### 2.4.3.3. Dynamic threshold and drainage event detection

After applying the incidence angle correction, noise remains in the $\overline{\sigma^\circ}_{\mathrm{HV35}}$ time series. This noise arises from factors such as varying SAR modes (e.g., Sentinel-1 IW vs. EW), differences across and between ScanSAR sub-swaths, and positional errors. We quantify this remaining noise with the same reference lakes described in Section 3.3.2 (10 non-draining lakes and 10 seasonally empty basins for each winter). For every month in each winter season, we compute all one-, two-, and three-observation cumulative increases in $\overline{\sigma^\circ}_{\mathrm{HV35}}$ inside the 20 lakes. These multi-step differences capture instances in our data set, where up to three observations can be made over a lake within approximately 36 hours. The distribution of these $\overline{\sigma^\circ}_{\mathrm{HV35}}$ increases provides an estimate of the remaining noise.

From that distribution we derive a dynamic threshold, four times the monthly median absolute deviation. We then apply this threshold to all lakes in the 10-year mask. An increase in $\overline{\sigma^\circ}_{\mathrm{HV35}}$ that exceeds this threshold is flagged as a potential drainage. An additional filter is applied where maximum pre-event $\overline{\sigma^\circ}_{\mathrm{HV35}}$ must be lower than the minimum post-event $\overline{\sigma^\circ}_{\mathrm{HV35}}$ with a 14-day window before and after. If multiple one-, two-, and three-step increases in $\overline{\sigma^\circ}_{\mathrm{HV35}}$ satisfy those criteria a drainage window start is set to the first image largest cumulative increase, and the window end is the subsequent inflection point of $\overline{\sigma^\circ}_{\mathrm{HV35}}$.

Each candidate time series is subsequently inspected to remove false positives, most of which are associated with $\overline{\sigma^\circ}_{\mathrm{HV35}}$ increases during the freeze-up period from September to early October. For the purposes of analyzing annual and seasonal trends, we define a single representative drainage date as the midpoint of the automatically identified drainage window. For suspected cascading events where neighboring lakes drain close in time and proximity, we manually inspected the $\overline{\sigma^\circ}_{\mathrm{HV35}}$ time series to identify the most likely drainage date within the automatically detected drainage window. Specifically, we selected the first observation at which $\overline{\sigma^\circ}_{\mathrm{HV35}}$ exceeds the dynamic threshold, and this observation along with the preceding one, defines the window of most likely drainage.

### 2.4.4. Lake depth and volume estimates

We use ArcticDEM strips (Porter et al., 2022) to estimate depth and volume of winter drained lakes. ArcticDEM strips are generated using high resolution optical image pairs processed by the Surface

Extraction with Triangulated Irregular Network-based Search-space Minimization (SETSM), with vertical error of 2.0 m and ~0.2 m after co-registration (Noh & Howat, 2015).

Estimation of winter lake volume is not possible in the absence of optical sensor data due to the presence of snow and ice lids. When ArcticDEM strips are available before and after a drainage within a winter season, they are co-registered and differenced with a vertical error of 0.28 m. Temporal coverage of ArcticDEM strips is sparse and instances of pre- and post-drainage DEMs within the same winter season are rare, as most strips date to late winter and early spring, after most lake drainages occur. For lakes where only post-drainage DEMs were available, we digitized the lake shoreline using the latest available Landsat images prior to polar night where it is visible. We then took the mean elevation of the shoreline using the earliest post-drainage DEM to represent the elevation of the lake lid and differenced it with the post-drainage DEM and assume a vertical error of 0.2 m. Similar approaches have been used previously for estimating lake volume from high resolution DEMs (Pope et al., 2016; Yang et al., 2019; Maier et al., 2023). In instances where no post-drainage DEM for a particular winter exists, the next available DEM from a subsequent winter was used. After differencing ArcticDEM strips within the 10-year lake mask, we only include pixels with negative elevation changes, as these indicate surface subsidence that would be associated with lake drainage.

Airborne radar observations across the GrIS suggest average ice lid thicknesses of 1.4 m and snow depths of 0.65 m (Koenig et al., 2015), while modeling has estimated ice lid and snow thicknesses of 0.8 m to 2.5 m under normal winter conditions (Law et al., 2020). Prior to calculating individual lake volume and mean lake depth, we subtract an assumed 1.4 m ice layer thickness from the depth of each ArcticDEM cell. For three lake drainages in the winter of 2023/2024, we were unable to find post-drainage DEMs for this year or any other year.

### 2.4.5. Modeling subglacial water pathways

To put the winter lake drainage observations into the context of subglacial melt water pathways, we calculate subglacial hydraulic potential gradients and their associated flow routing (Shreve, 1972; Livingstone et al., 2013). Assuming the subglacial water pressure equals the ice-overburden pressure ($N$ = 0), hydraulic potential ($\Phi$) is given by:

$$\Phi = \rho_w g z_b + \rho_i g z \qquad (3)$$

where $\rho w$ is water density, $\rho i$ is ice density, $g$ is the acceleration of gravity, $zb$ is the bed elevation from BedMachine Version 5 (Morlighem, 2022), and $z$ is the ice thickness. Because we are interested in subglacial water pathways rather than subglacial lakes, all sinks are filled in the hydraulic potential map (Livingstone et al., 2013; Smith et al., 2017). Then, using the D8 direction method (O'Callaghan & Mark, 1984), we model the direction of flow along the subglacial hydraulic potential gradients to produce an upstream water accumulation map.

### 2.4.6. Auxiliary data

To provide context about the intensity and extent of melt during each melt season, we used daily ASCAT C-band normalized radar cross-section sigma naught ($\sigma^o$) to define the presence or absence of surface melt for each grid cell across 79NG and ZI. We used a threshold of −3.0 dB below / above the previous winter's mean backscatter to define the presence / absence of melt (Ashcraft & Long, 2006). This was done for the 2014 to 2022 melt seasons, as at the time of analysis data for 2023 were unavailable. This threshold was developed for C-band radar with a center frequency of 5.3 GHz and it identifies wet snow conditions based on the difference in observed backscatter relative to dry snow conditions (Ashcraft & Long, 2006). For the calculations, winters are defined as 1 January to 31 March, with the melt seasons extending from 1 June to 31 August. We used the daily binary melt / no melt data to calculate the melt intensities (number of melt days) for each grid cell across the 79NG and ZI basins for each summer. We also used the daily binary melt / no melt data to calculate time series of melt extents (total area experiencing melt) across the entire region each summer. To enable comparison of melt intensity and extent between the years, we also calculated an annual melt index, defined as the sum of daily melt extents over the summer.

To investigate possible dynamic effects of the winter lake drainages, monthly ice velocities were analyzed from June 2015 to May 2024 along transects extending from near the termini to upstream of both 79NG and ZI (Figure 2.1b). The ice velocity products used were SAR- and Landsat-derived monthly MEaSUREs Version 5 (Joughin, 2023). To investigate possible short-term effects of winter lake drainages on ice dynamics, we analyzed 6- and 12-day SAR-derived MEaSUREs Version 2 data along transects around lakes involved in cascading events, focusing on periods before, during and after each event (Joughin 2022).

## 2.5. Results

### 2.5.1. Winter lake drainage at Nioghalvfjerdsbræ and Zachariæ Isstrøm

Between the 2014/2015 and 2023/2024 winter seasons, there were 90 surface lake drainage events occurring at 55 individual lakes across both 79NG (48 events) and ZI (42 events) (Figure 2.4). The minimum, mean and maximum elevation of the draining lakes were 88 m, 485 m and 1046 m respectively. There was only one drainage event above 1000 m, despite 140 of the 404 lakes identified in the 10-year optical melt-season lake mask occurring above this elevation, and despite previous documentation of lakes at elevations of up to 1500 m in the region (Schröder et al., 2020; Hochreuther et al., 2021; Lu et al., 2021) (Figure 2.4).

Of the 55 individual lakes, 34 drained once over the ten winters, 12 drained twice, six drained three times, two drained four times, and one lake drained six times. The maximum number of drainage events during a single winter was 18 during 2018/2019 and the minimum was four during both 2020/2021 and 2021/2022 (Figure 2.5a). In the winters leading to the 2018/2019 season there is an increasing number of drainages (Figure 2.5a). Following the winter of 2018/2019, there are markedly fewer drainages including the minimum count of four in 2020/2021 and 2021/2022 seasons. The most common month for drainages was September, in which approximately one third of the total (31/90) occurred (Figure 2.5b). The months with the second and third most drainages were October and November, respectively. While there is a trend of decreasing drainage frequency between September and February, there is a notable increase in March and April when nine and eight drainages occur, respectively. Seven of the eight drainages that occurred in April were associated with a single cascading event during the 2018/2019 season (see Section 4.3). In general, therefore, fewer drainages occurred as the winters progressed, with drainages picking up again in late winter.

The three winter seasons with the greatest number of drainages, 2016/2017 - 2018/2019, exhibit different lake drainage timings. In 2016/2017 all drainages occurred before the midpoint of winter in mid-January (Figure 2.5c). There is a cluster of drainages in September followed by longer periods between drainage events. Drainages were dispersed more evenly throughout the 2017/2018 winter. In 2018/2019, drainages occurred in both early and late winter but were more clustered relative to 2017/2018. In the following three winters, there were very few drainages, all occurring before mid-December in the 2020/2021 and 2021/2022 seasons (Figure 2.5c).

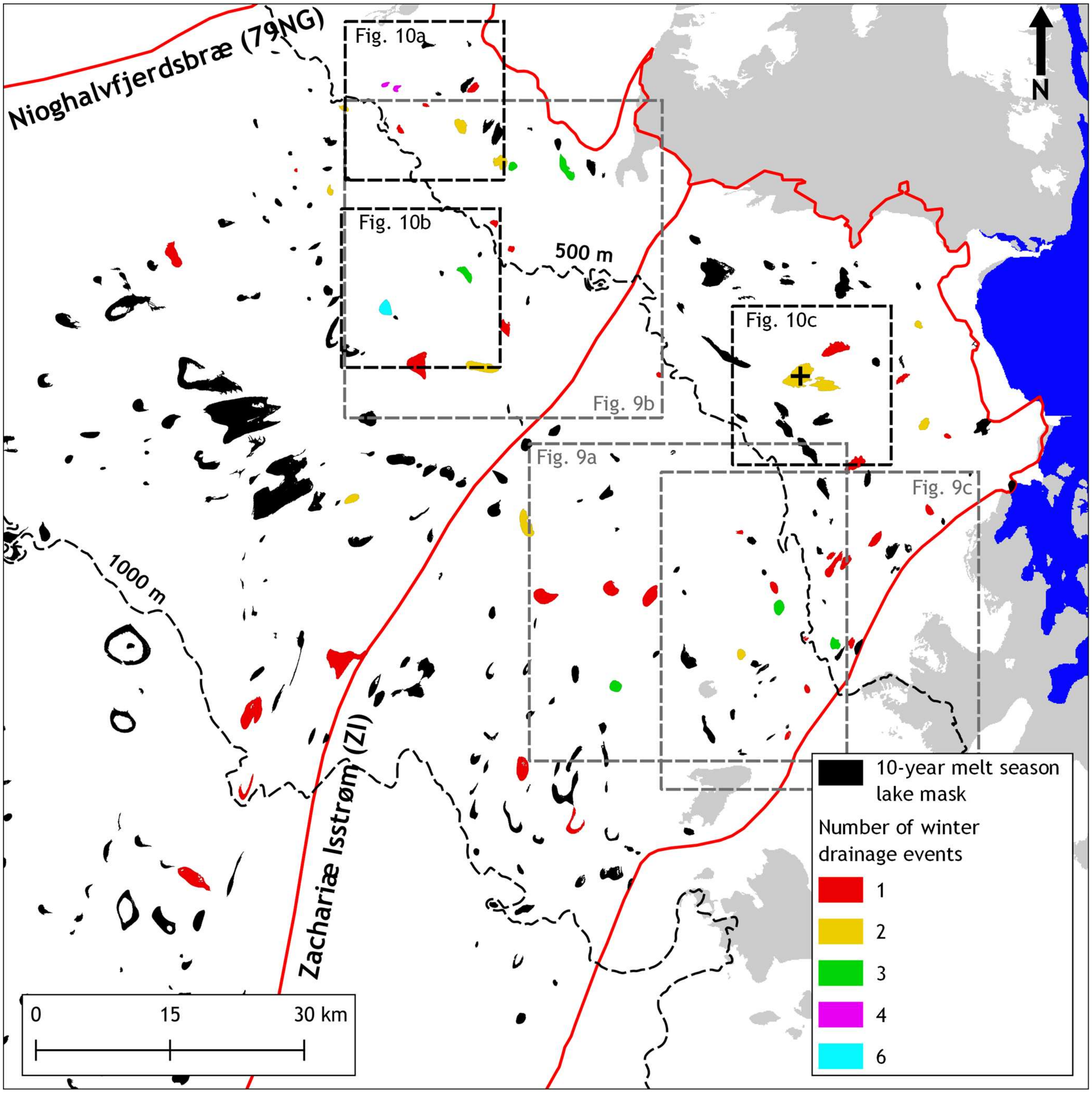


**Figure 2.4.** Lake locations from the 10-year melt season lake mask and locations and frequencies of drainage events during the 10 winter seasons between 2014/2015 and 2023/2024. A black "✚" marks the single lake near the Zachariæ Isstrøm terminus that produced two unusually large drainage volumes (0.052 km³ and 0.038 km³). Dashed rectangles show study areas expanded in Figure 2.10 to Figure 2.11. Gray shading indicates land areas, and blue represents an ocean mask, both derived from the GIMP lake, ice, and ocean classification dataset (Howat, 2017).

Although most draining lakes drain just once over a winter, there are three instances of lakes draining twice over a winter, one each in 2014/2015, 2017/2018, and 2019/2020. All three lakes were at low elevations (< 150 m), two near the termini of 79NG and one near the termini of ZI. In each case, the second drainage occurred no sooner than three months after the first, with the first happening before December, and the second happening after the start of February.

Using timestamped ArcticDEM strips, we estimated the volumes and mean depths of 87 of the 90 winter lake drainages (Figure 2.6). The remaining three lakes drained during the 2023/2024 season, for which data were unavailable at the time of analysis. The mean depth of the 87 drained lakes is 4.10 m. 85 of the 87 lakes had volumes < ~0.02 $km^3$. There are two outlier drainage volumes of 0.052 ± 0.0096 $km^3$ and 0.038 ± 0.0008 $km^3$, attributed to two separate drainages of  a single lake at an elevation of 259 m near the terminus of ZI (marked in Figure 2.4). The mean volume of drained lakes excluding the two outliers is 0.0039 ± 2.8e-5 $km^3$.

### 2.5.2. ASCAT melt season variability

The nine melt seasons preceding the 2014/2015 to 2022/2023 winters exhibited varying melt intensities (Appendix A Figure. A.1), melt extents (Figure 2.7a, Appendix A Figure. A.2), and melt indices (Figure 2.7b). From the 2015 to the 2018 melt season, there is a decrease in the melt index from $1.88 \times 10^6$ $km^2$-days to $4.61 \times 10^5$ $km^2$-days (Figure 2.7b). This is due to a decrease in the average melt intensity and melt extent during these years (Appendix A Figure A.1 and A.2). Following 2018, the melt index of the 2019 and 2020 melt seasons increased to $1.33 \times 10^6$ $km^2$-days and $1.41 \times 10^6$ $km^2$-days respectively. Thus, the winter seasons of 2017/2018 and 2018/2019, which were among the seasons with the greatest number of lake drainages, 13 and 18 respectively (Figure 2.5a), were preceded by melt seasons with the two lowest melt indices (Figure 2.7b). Conversely, the winter seasons of 2019/2020 and 2020/2021, when just six and four drainages occurred (Figure 2.5a), were preceded by summers with high melt intensities and extents (Figure 2.7a). A comparison of the 2017 to 2020 summer melt extent time series shows that melt extent was typically less in 2017 and 2018 than in 2019 and 2020 (Figure 2.7a). The time series for 2019 and 2020 show greater maximum melt extents and more sustained periods of melt extents > 20,000 $km^2$, compared to the 2017 and 2018 series (Figure 2.7a).

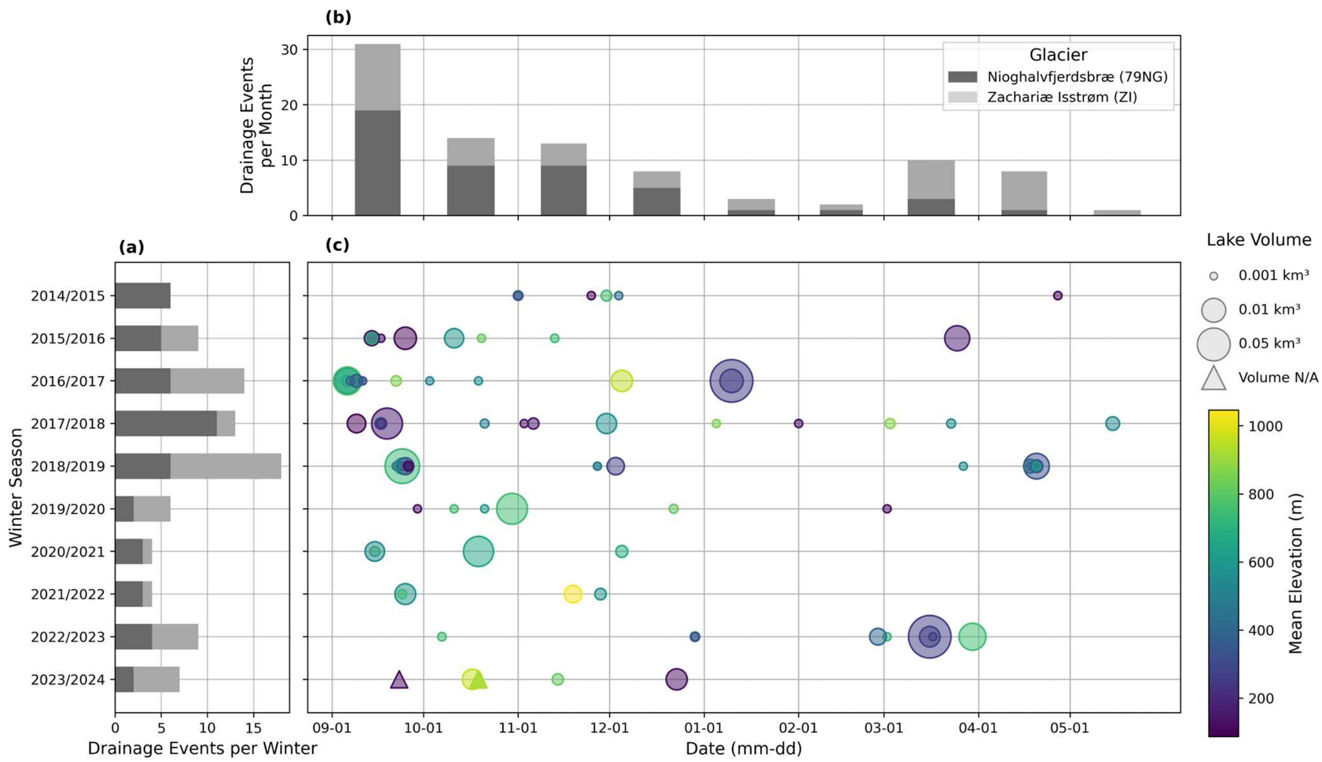


**Figure 2.5.** (a) The total number of drainage events to occur over the 10 winter seasons shown for each month September to May. (b) The total number of lake drainages shown for each winter season 2014/15 to 2023/24. (c) The timing, mean elevation and volume of each drainage event for each winter season. In the histograms (a) and (b), drainages of Nioghalvfjerdsbræ (79NG) and Zachariæ Isstrøm (ZI) are symbolized in dark grey and light grey respectively.

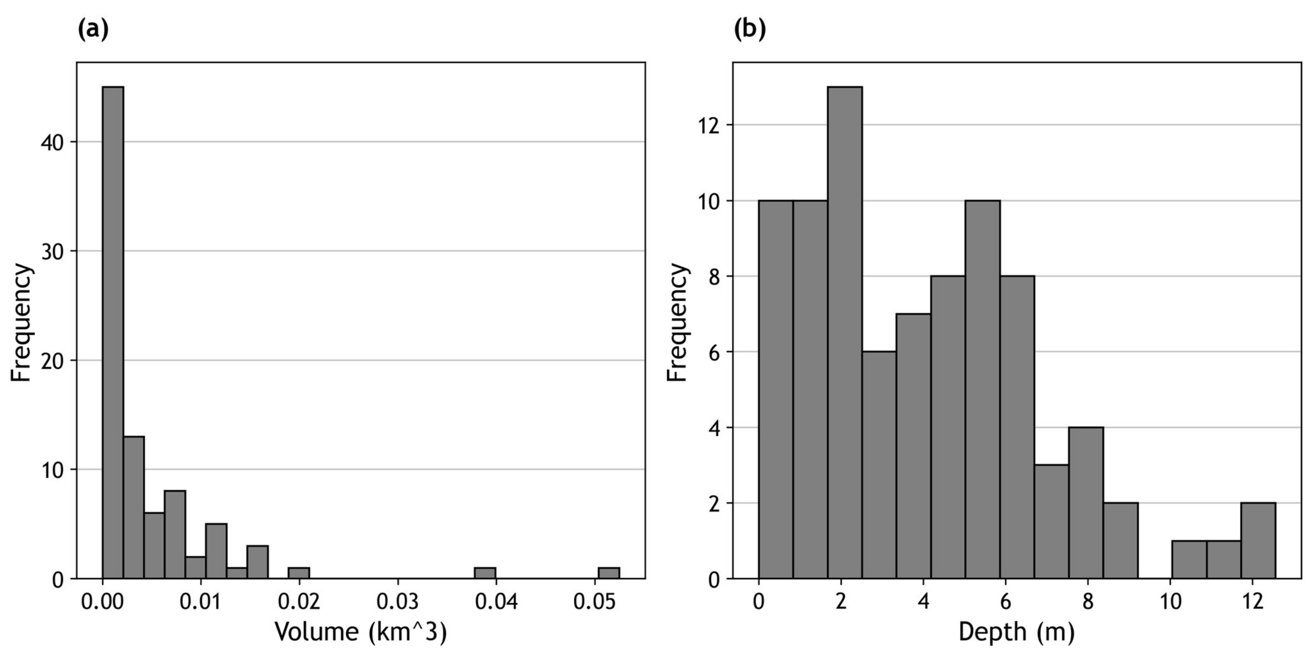


**Figure 2.6.** Histograms of (a) lake volumes and (b) mean lake depths for 87 winter-draining lakes derived from ArcticDEM timestamped strips.

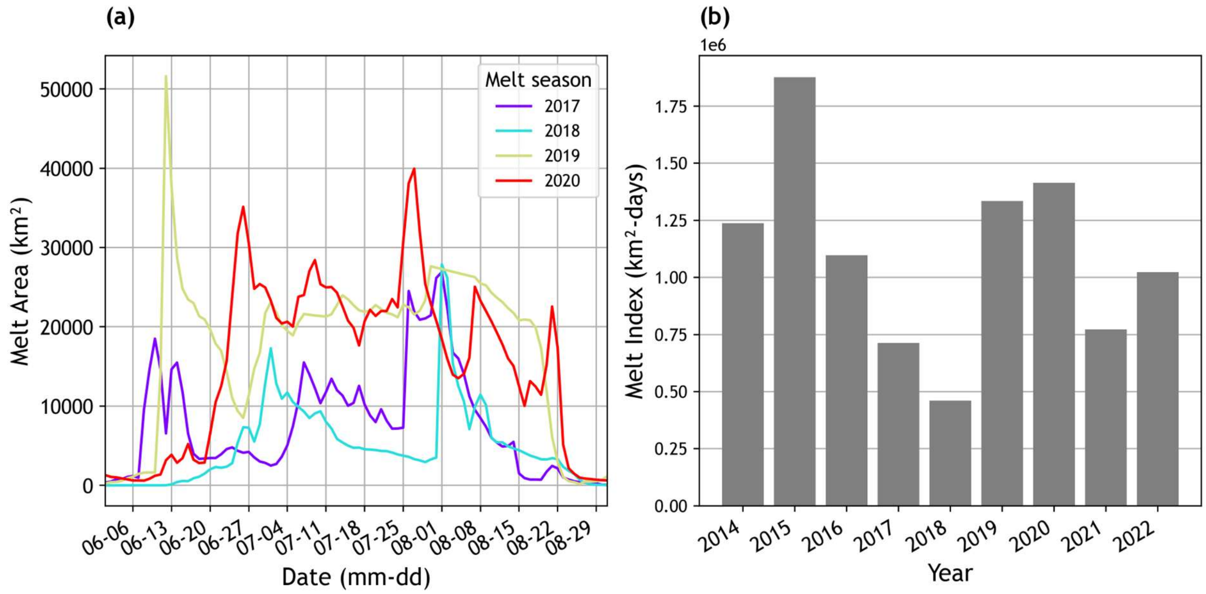


**Figure 2.7.** (a) Melt index for summers 2014 to 2022, where ASCAT-derived melt area of each day during the melt season is summed. (b) Time series of ASCAT-derived melt extent from 1 June to 31 August for the 2017 to 2019 melt seasons.

### 2.5.3. Comparison of winter and summer lake drainage occurrence

To enable a comparison between winter and summer rapid lake drainages, we subset our data to include just the seven 2016/2017 to 2022/2023 winter seasons and their preceding 2016 to 2022 melt seasons (June to August), for which rapid drainage events over NE Greenland are available from Lutz et al., (2024) (Figure 2.8, Appendix A Figure A.3). Over this period, there were 306 summer and 68 winter drainage events (summer-to-winter drainage ratio of 4.5:1), involving 129 and 42 unique lakes respectively (summer-to-winter lake ratio of just over 3:1). The mean elevation of summer draining lakes was 458 m, lower than the 515 m mean elevation of winter draining lakes (Figure 2.8).

The ratio of summer to winter drainages ranged from nearly ~1.3:1 in 2018/2019 to ~11.5:1 in 2019/2020. The 2018 melt season was notably cool, with a low melt index (Figure 2.7b), and the fewest drainages (25) of any melt season. In contrast, the subsequent 2018/2019 winter had the greatest number of drainages (18) of any winter over the seven years. The 2019 melt season was uncharacteristically warm, with a relatively high melt index (Figure 2.7b) and high melt intensities extending to higher elevations (~1500 m) than in other years (Appendix A Figure A.2). It had the greatest number of drainages (71), while the subsequent 2019/2020 winter had just six. Between the 2016 and 2018 melt seasons, the number of summer drainages decreased, while the number of subsequent winter drainages remained relatively constant (Figure 2.8a). After 2018, summers had comparatively more drainages while winters had fewer.

While for most lakes, rapid drainages recurred across multiple melt seasons (Lutz et al., 2025) and for some lakes, drainages were frequently observed across several winters in our study, drainage of a lake in both a melt season and its subsequent winter was very rare. There were two such instances: one in 2016/2017, and another in 2018/2019. Similarly, most lakes that drained during winter did not drain again the following summer. There were 13 such instances of lake drainage in winter and the subsequent melt season. Once in 2016/2017, 2018/2019, and 2020/2021. Twice in 2019/2020 and 2021/2022; and six times in 2018/2019.

Several lakes drained during multiple summer and winter seasons and displayed several types of behaviour. The most common type, affecting 39 lakes, was lakes that drained during one melt season but did not drain in any winter (Figure 2.8b). Another 21 lakes drained in one winter and between zero and three times separate melt seasons across the seven year period. Only six lakes drained in multiple melt and winter seasons (two or three seasons each). Two lakes drained a total of six times across four winters and two summers (Figure 2.8b).

To assess potential associations between winter drainage frequency, summer drainage frequency, and melt intensity / area (represented by the ASCAT melt index), we conducted least-squares regression analysis (Figure 2.9). The analysis covers seven pairs of summer and winter seasons (df = 6), where each winter is paired with the preceding summer. We report the correlation coefficient (r), coefficient of determination ($R^2$), and slope (s). Due to our small sample size, we set a significance threshold of $p \leq 0.1$. Results are summarized in Table 2. The number of winter drainages in the 25th, 50th, and 75th elevation quartiles was negatively correlated with the number of preceding summer drainages (Figure 2.9a), although the 25th quartile correlation was non-significant ($p$ = 0.27). Conversely, high-elevation lakes in the fourth quartile exhibited a significant positive correlation ($p$ = 0.085).

The summer to winter ratio showed a significant negative correlation with the melt index ($r$ = -0.83, $p$ = 0.02) (Figure 2.9b). This indicates that the frequency of winter drainages compared to previous summer drainages decreases as melt-season intensity and / or area go up. Both the number of summer drainages and the total number of drainages annually were positively correlated with the melt index, and both correlations were statistically significant ($p$ = 0.001 and $p$ = 0.02, respectively) (Figure 2.9c). Conversely, the number of winter drainages was negatively correlated with the melt index; this relationship was not statistically significant although it approached the threshold ($p$ = 0.11) (Figure 2.9 c).

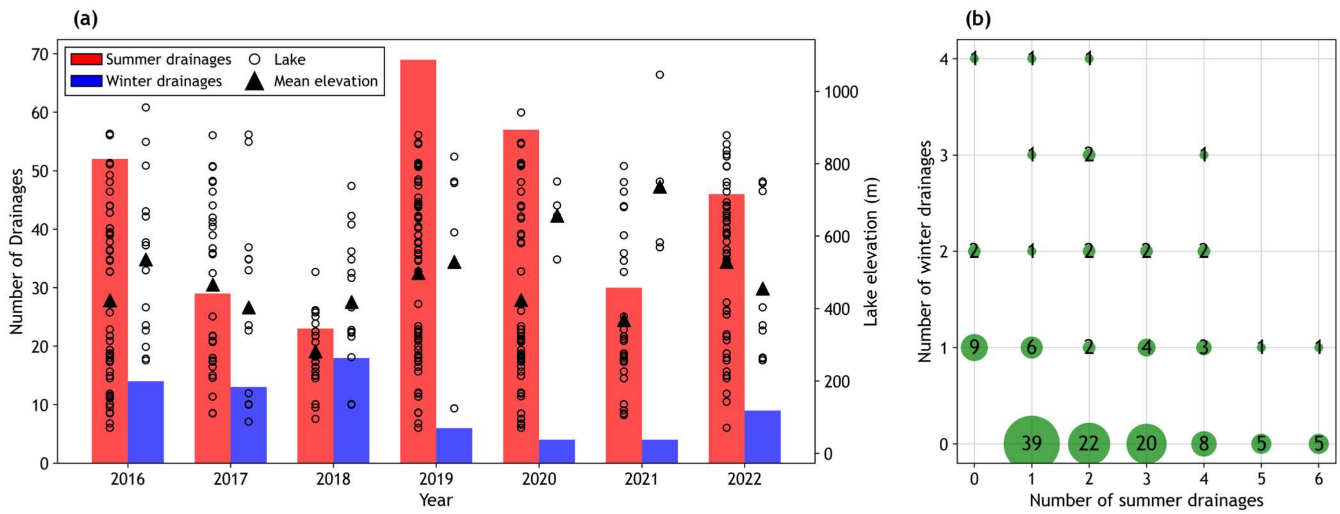


**Figure 2.8.** (a) Number of rapid lake drainages during the melt season (red bars) and winter (blue bars) by year. The melt season is defined as June to August, while winter is September to May of the following year. Melt season lake drainages are from Lutz et al. (2024). For each year, individual lake elevations are shown as hollow circles, with mean elevations for each season shown as triangles. (b) Relationship between the number of winter and melt season drainages for individual lakes. The green circle size is scaled to the number of lakes with a given combination of melt season and winter drainages, with the count also labelled within each circle.

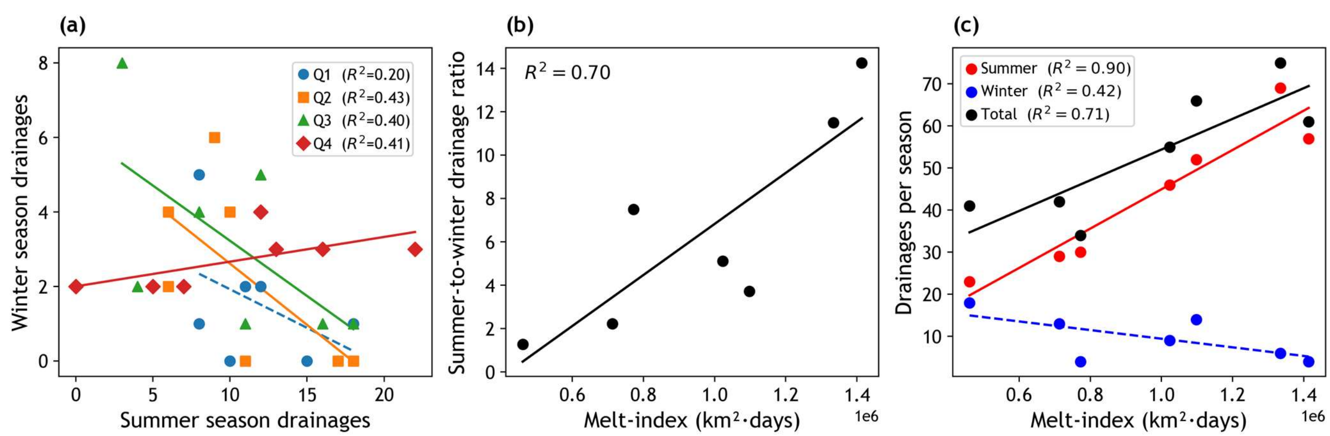


**Figure 2.9.** Linear regression plots showing relationships between various drainage parameters and the summer melt index for the years 2016/2017 to 2022/2023. Solid lines indicate statistically significant correlations ($p \leq 0.1$), dashed lines indicate non-significant correlations. (a) Number of winter drainages (September–May) versus number of drainages in the preceding melt season (June–August), with data separated by lake elevation quartiles. (b) Ratio of summer to winter drainages versus melt index. (c) Number of winter, melt-season, and total annual drainages (combined winter and preceding melt-season drainages) versus melt index.

**Table 2.2.** Linear regression results for winter and summer drainage frequencies and melt index shown graphically in Figure 2.9. Regressions are based on seven paired seasons (df = 6), where each winter season (September–May) is paired with the preceding summer season (June–August). For each comparison we report the coefficient of determination ($R^2$), Pearson's correlation coefficient ($r$), slope ($s$), and $p$ value. Rows 1–4 show winter versus summer drainages by elevation quartile (Q1–Q4). Subsequent rows show the summer to winter drainage ratio versus melt index, summer drainages versus melt index, winter drainages versus melt index, and total annual drainages (winter plus preceding summer) versus melt index.

| Regression pair | $R^2$ | $r$ | $s$ | $p$ |
|---|---|---|---|---|
| Winter vs. summer drainages Q1 (71–261 m) | 0.20 | -0.44 | -0.21 | 0.27 |
| Winter vs. summer drainages Q2 (262–393 m) | 0.43 | -0.65 | -0.33 | 0.08 |
| Winter vs. summer drainages Q3 (394–655 m) | 0.40 | -0.63 | -0.30 | 0.09 |
| Winter vs. summer drainages Q4 (656–1046 | 0.41 | 0.64 | 0.07 | 0.09 |
| Summer-to-winter ratio vs. melt index | 0.70 | 0.84 | $1.18 \times 10^{-5}$ | 0.02 |
| Summer drainages vs. melt index | 0.90 | 0.95 | $4.67 \times 10^{-5}$ | 0.001 |
| Winter drainages vs. melt index | 0.42 | -0.65 | $-1.03 \times 10^{-5}$ | 0.11 |
| Total drainages vs. melt index | 0.71 | 0.84 | $3.65 \times 10^{-5}$ | 0.02 |

### 2.5.4. Cascading winter drainage events

We analyzed the timing and proximity of neighboring lake drainages in relation to the maps of hydraulic potential and subglacial water pathways to identify lakes that may have been triggered by the drainage of neighboring lakes via either stress coupling through the ice or hydrologic coupling along the subglacial drainage pathway. We refer to these occurrences as cascading drainage events (Christoffersen et al., 2018). The analysis revealed that 46 of the 90 lake drainages over the ten winter seasons may have been part of cascading drainage events. Of these, 18 occurred in three separate events, involving between five and seven lakes, with the most distant lakes in each event separated by ~25-33 km. The remaining 28 occurred across 12 events, involving two to three lakes in close (<10 km) proximity. Therefore, cascade events involving large clusters are less common than those involving small clusters. Below we present the results from the three events involving between five and seven lakes and follow this with three examples of events involving two or three lakes.

The first instance of cascading lake drainage involving between five and seven lakes occurred during the 2016/2017 winter. Between 5 September 08:43 and 6 September 17:32, five lakes drained on ZI (Figure 2.10a$_i$). The highest lake elevation was ~795 m and the lowest was ~400 m. The distances between the respective lakes were 8 km from L1A to L1B, 4.8 km from L1B to L1C, 12 km from L1C to L1D, and 10.5 km from L1D to L1E. Thus, the two most distant lakes, L1A and L1E, were ~33 km apart. All lakes are connected along a modeled subglacial melt water pathway (Figure 2.10a$_i$). Other lakes at distances comparable to those between the drained lakes, did not drain and were also not hydrologically connected through subglacial pathways.

The two other cascading drainage events involving large clusters occurred during the 2018/2019 winter (Figure 2.10$b_i$ and $c_i$). The first group of lakes drained on 79N. Within a ~36-hour period between 23 September 08:58 and 24 September 17:47 lakes L2A and L2B drained at ~740 m and ~660 m elevation respectively (Figure 2.10$b_i$). Lakes L2A and L2B were ~4.5 km apart. In the following ~15 hours, Lake L2C and L2D drained between 24 September 17:47 and 25 September 08:42. The drainages of L2C and L2D occurred ~14 km downstream of L2B at elevations of ~410 m and ~330 m respectively. The final two lakes, L2E and L2F, both at an elevation of ~130 m, drained ~6 km downstream from L2C and L2D between 25 September 08:42 and 27 September 08:26.

The third large cluster cascading lake drainage event involved seven lakes and occurred in April of the 2018/2019 winter season on ZI (Figure 2.10$c_i$). Lakes L3A and L3B at ~400 m elevation and just 1 km apart drained between 17 April 18:29 and 19 April 08:26. Approximately 7 km downstream, and at an elevation of ~330 m, lakes L3C to L3F then drained within a 10-hour period between 19 April 08:26 and 18:12. The final lake, L3G, drained between 19 April 18:12 and 20 April 08:18. Lake L3G was at an elevation of ~630 m and situated ~12 km upstream of lakes L3A and L3B, and ~19 km upstream of lakes L3C to L3F.

Examples of cascading lake drainages involving small clusters of lakes (2 or 3 lakes) over relatively short distances are shown in Figure 2.11. The first event involved three lakes and occurred in September of the 2017/2018 winter on 79NG (Figure 2.11$a_i$). Within a ~48-hour period between 16 September 08:58 and 18 September 08:42, lakes L4A and L4B drained at an elevation of ~350 m. Lakes L4A and L4B were ~1 km apart (Figure 2.11$a_i$). In the ~24-hour period beginning 19 September 08:35, L4C drained ~8 km downstream at an elevation of ~166 m. The second event involved two lakes and occurred in September of the 2021/2022 winter season on 79NG (Figure 2.11$b_i$). Within a ~48-hour period between 24 September 18:05 and 26 September 17:49 lakes L5A and L5B drained at ~751 m and ~569 m respectively. Lakes L5A and L5B were separated by ~10 km, the maximum distance observed for small cluster drainage events involving two or three lakes. The third event occurred in March 2023, involving three lakes at ~260 m elevation on ZI (Figure 2.11$c_i$). Lake L6A to L6C drained within a ~24-hour period between 15 March 17:41 and 16 March 17:23.

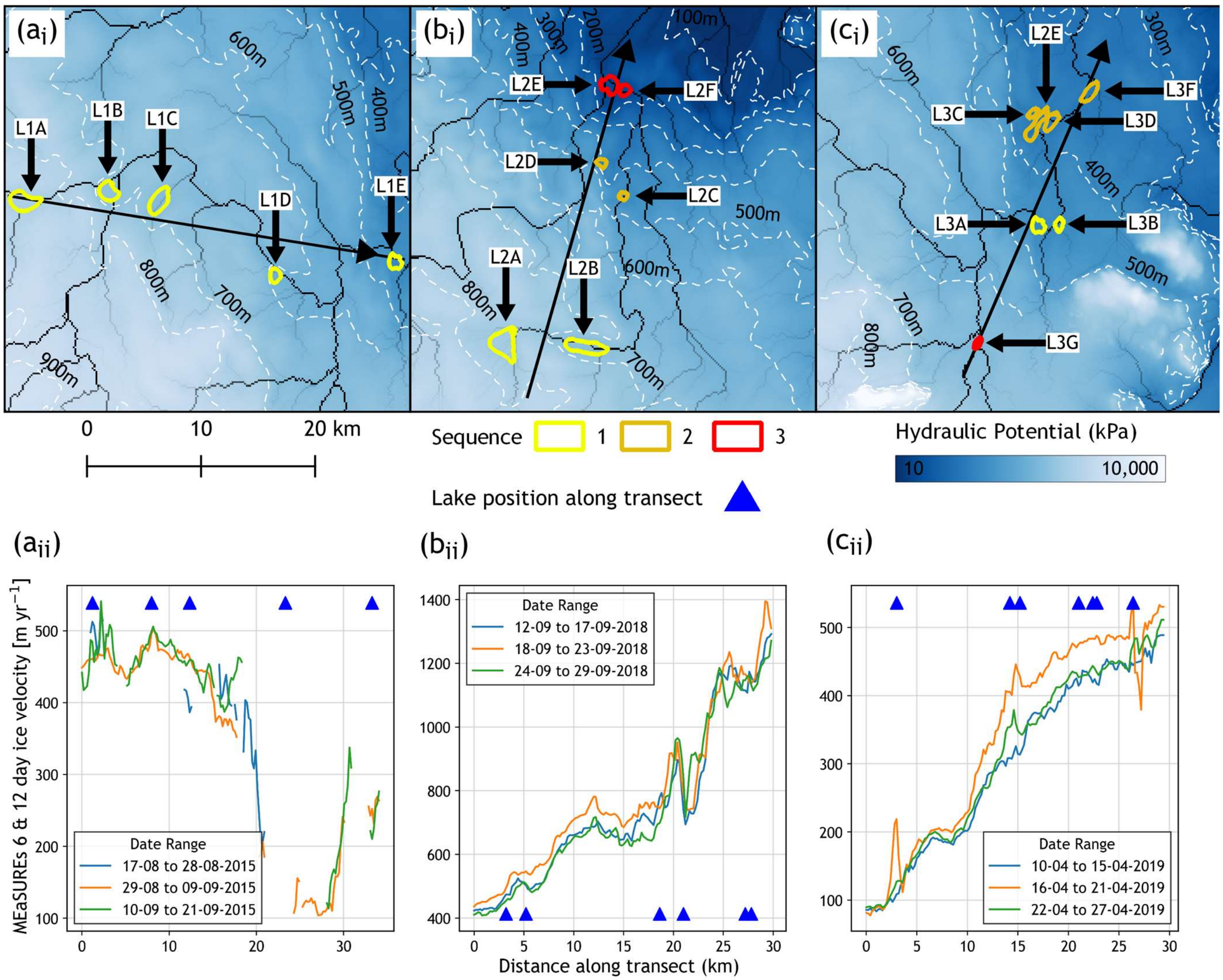


**Figure 2.10.** Location maps (i) and velocities (ii) associated with the three 'large cluster' cascading drainage events involving five to seven lakes. ($a_i$) depicts the cascade event of L1A to L1E between 5 September 08:43 and 6 September 17:32 2015, ($b_i$) shows the cascade event of L2A to L2F between 23 September 08:58 and 27 September 2018, and ($c_i$) shows the cascade event of L3A to L3G between 17 April 18:29 and 20 April 08:18 2019. The drainage sequence during the events are colored yellow, orange, and red. In the maps, lake polygons, representing drained lake locations, are overlaid on the subglacial hydraulic potential grid with modeled subglacial pathways represented as lines shaded grey to black showing low to high upstream area accumulation. Black transect lines going from higher to lower elevations closely follow lake locations. In the velocity plots, velocities are sampled from 6- and 12-day SAR MEaSUREs Version 2 data at 200 m intervals along the transects shown in the maps. Approximate lake locations are represented by blue triangles. Date ranges of the 6- and 12-day MEaSUREs image pair are included in the legends.

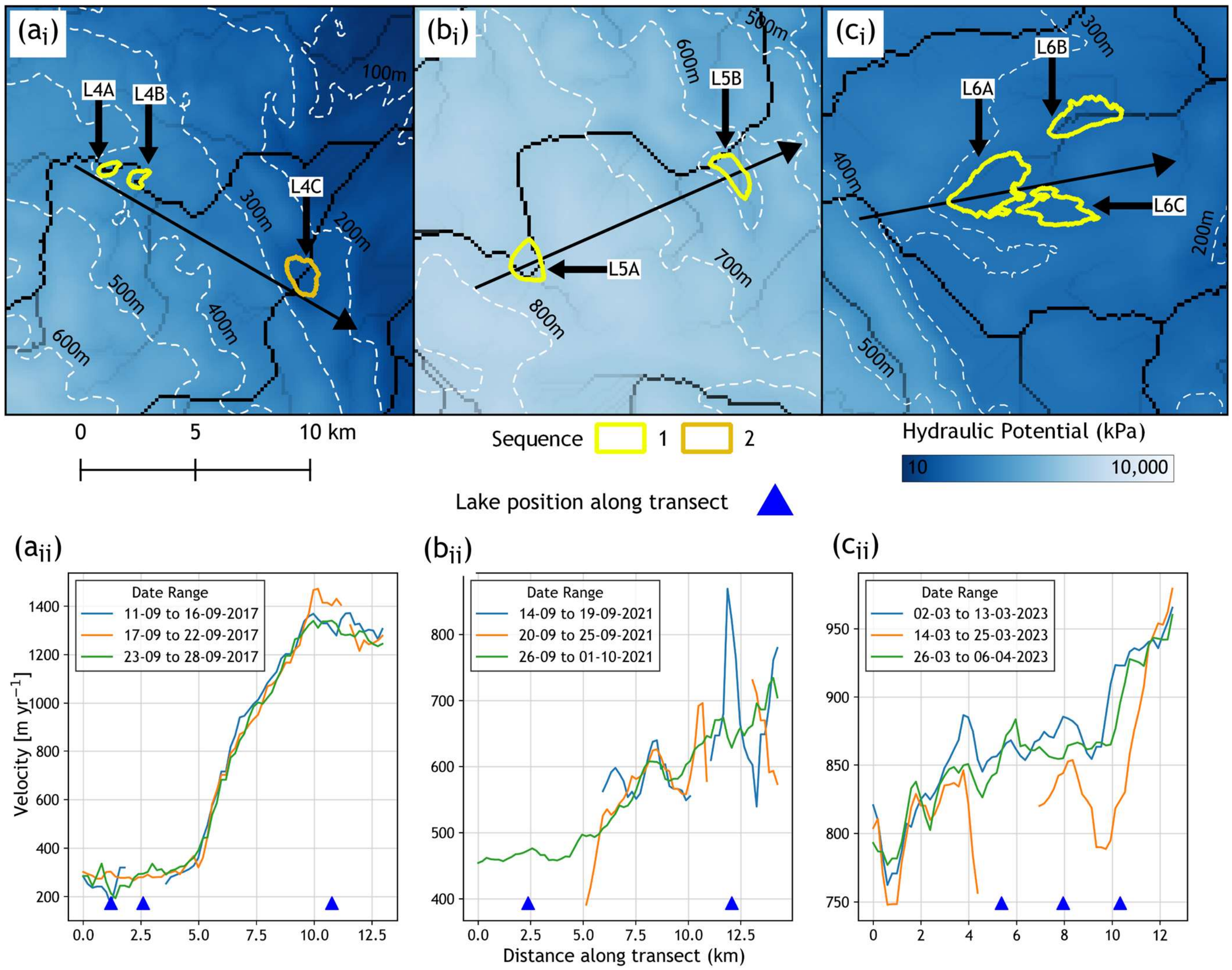


**Figure 2.11.** Location maps (i) and velocities (ii) associated with the three cascading drainage events involving between two and three lakes outlined in Section 4.4. ($a_i$) depicts the cascade event of L4A to L4E between 16 September 08:58 and 18 September 08:42 2017, ($b_i$) shows the cascade event of L5A to L5B between 24 September 18:05 and 26 September 17:49 2021, and ($c_i$) shows the cascade event of L6A to L6C between 17 April 18:29 and 20 April 08:18 2019. Sequence of drainages during the events are colored yellow, orange, and red. In the maps, lake polygons, representing drained lake locations, are overlaid on the subglacial hydraulic potential grid with modeled subglacial pathways represented as lines shaded grey to black showing low to high upstream accumulation. Black transect lines going from higher to lower elevations closely follow lake locations. In the velocity plots, velocities are sampled from 6- and 12-day SAR MEaSUREs Version 2 data at 200 m intervals along the transects shown in the maps. Approximate lake locations are represented by blue triangles. Date ranges of the 6- and 12-day MEaSUREs image pair are included in the legends.

### 2.5.5. Ice velocities

Monthly ice velocity series between 2015 and 2024 for transects along 79NG and ZI are shown in Figure 2.12. Near terminus velocities are highest at ZI, ranging ~1600 - 2200 m yr$^{-1}$ ~5 km from the terminus, and ~1200 - 1600 m yr$^{-1}$ ~10 km from the terminus. Near terminus velocities at 79NG are slower, with velocities at both 5 km and 10 km from the terminus ranging ~1000 - 1250 m yr$^{-1}$. Seasonal cycles in ice velocity at ZI are highly pronounced. Following peaks in July, velocities decrease until September or October, in most cases to values below those that existed prior to the melt season, and to the minimum for the year. Following these late- and post-summer slowdowns, velocities gradually increase throughout the winter months. The exception is the anomalously cool 2018 melt season, when there was a minimal late- to post-summer slowdown and fairly constant winter velocities. At 79NG, seasonal ice velocity cycles are less pronounced than at ZI.

Throughout the study period, 79NG and ZI had different interannual trends. Velocities at ZI had overall increasing trends, particularly towards the terminus, whereas velocities at 79NG were relatively stable. At the monthly resolution, there were no apparent increases in ice velocity that may be attributable to the observed winter drainage events. For both glaciers, winters that had the greatest number of drainages (2016/2017 and 2018/2019) had comparable velocities to the other winters, including those with relatively few drainage events (2019/2020 to 2021/2022) (Figure 2.5a and Figure 2.12).

The 6- and 12-day SAR-derived MEaSUREs velocities were sampled at 200 m intervals along transects following the large cluster cascade events of between five to seven lakes (Figure 2.10$a_i$ to $c_i$) and the small cluster events of two or three lakes (Figure 2.11$a_i$ to 10$c_i$). During the first large cluster cascade between 5 September 08:43 and 6 September 17:32 2015, there was poor ice velocity coverage, but the available data show no evidence for any ice velocity changes associated with the event (Figure 2.10$a_{ii}$). For the second large cluster cascade between 23 September 08:58 and 27 September 2018 08:26, there was good ice velocity coverage (Figure 2.10$b_{ii}$). There were relatively high velocities along the transect between 18 and 23 September, particularly from 0 and 15 km and, to a lesser extent, from 25 and 35 km. These high velocities appear to be associated with the drainages of L2A and L2B that occurred between 23 September 08:58 and 24 September 17:47 (Figure 2.10$b_{ii}$). It is not possible to link the velocity increase to the lake drainages conclusively, as the latter occur between the 18 - 23 September and 24 - 29 September 6-day MEaSUREs velocity image pairs. Elsewhere along the transect, velocities are largely similar before, during and after the drainage of subsequent lakes of the cascade. The third large cluster cascade between 17 April 18:29 and 20 April 08:18 2019 appears to be associated generally with an increase in ice velocity, as captured by the 16 - 21 April 2019 MEaSUREs image pair (Figure 2.10$c_{ii}$). At ~3 km along the transect, near L3G, there is an isolated velocity spike during the drainage event, after which velocity returns to pre-event values. From ~10 km along the transect, the velocity increase during the event is even more apparent, with velocities greater than pre drainage ones by ~40 to 100 m $yr^{-1}$. During the drainage event, there is a prominent spike in velocity located ~15 km along the transect, which is directly adjacent to L3A and L3B. During the event, there is a sharp velocity increase at ~26 km and a marked decrease at ~27 km compared to before the event. These areas are close to the L3C to L3E lakes, and to lake L3F respectively (Figure 2.10$c_i$). After the cascade event, ice velocities generally return to pre drainage values.

During the small cluster cascades involving two or three lakes (Figure 2.11$a_i$ to 10$c_i$), there is no clear evidence of a consistent velocity response before, during or after the lake drainages, in part, perhaps, due to gaps in the ice velocity maps. During the cascade between 16 September 08:58 and 20 September 08:26 2017, there is only an isolated spike approximately 11 km along the transect adjacent to L4C (Figure 2.11$a_{ii}$). There is poor coverage of the event between 24 September 18:05 and 26 September 17:49 but the data do not reveal any clear velocity anomaly, except, perhaps, for a spike followed by sudden drop in velocity ~12 km along the transect at the location of L5B prior to its drainage (Figure 2.11$b_{ii}$). For the event between 15 March 17:41 and 17 March 17:31, there is a velocity decrease along the transect, with a significant drop at ~9 km (Figure 2.11$c_{ii}$).

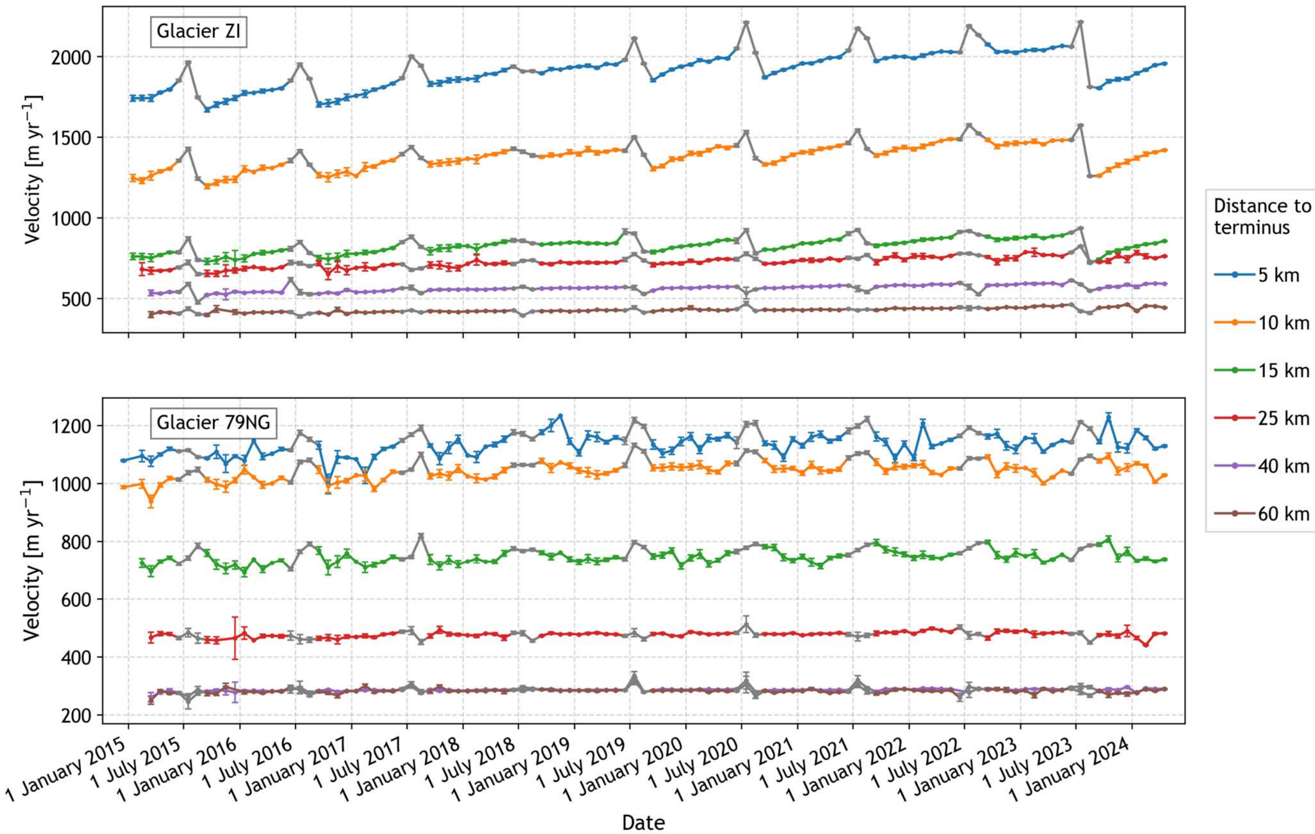


**Figure 2.12.** MEaSUREs monthly ice velocity series between June 2015 and January 2024 for Nioghalvfjerdsbræ (79NG) and Zachariæ Isstrøm (ZI) at points along transects shown in Figure 2.1b.

## 2.6. Discussion

### 2.6.1. A new method for detecting winter supraglacial lake drainages

We developed a semi-automated method to observe winter lake drainage events at high temporal resolution using incidence-angle-normalized C-band SAR. This allowed for observations of winter lake behaviour, that had previously not been made. In particular, incorporating images from different sensor geometries allowed us to detect drainages at up to sub-daily temporal resolution, permitting the timing of lake drainages to be identified with greater precision compared to the 6- and 12-day revisit times for the same orbits with Sentinel-1, or the 4-day revisit times with RCM. For cascading drainage events involving multiple lakes over periods of several days, a more precise succession of drainages could be determined, compared to the temporal aliasing that is introduced with longer revisit time, causing cascades to appear as a synchronous event (Cooley & Christoffersen et al., 2018; Stevens et al., 2024). Furthermore, by focusing on winter, when active meltwater production and lake filling are absent, minimized the influence of slow drainage processes, such as overtopping and channel incision, allowing us to focus on rapid drainages, likely caused by hydrofracture.

We used a Landsat-derived 10-year summer lake mask for tracking the mean $\overline{\sigma^\circ}_{HV35}$ of lakes throughout the winters (as in Benedek & Willis, 2021). This allowed us to detect drainages of lakes that remained buried for one or more years, which have been documented throughout Greenland, including at 79NG and ZI (Koenig et al., 2015; Lampkin et al., 2020). Additionally, it allowed us to include portions of lakes covered by snow and ice lids. Many winter drainage events would likely have been missed if just annual summer lake masks had been used, especially, e.g., following the low-melt summer of 2018, when many lakes showed little to no surface expression (Dunmire et al., 2021; Zheng et al., 2023).

Using the 10-year lake mask introduced large variability in the magnitude of observed $\overline{\sigma^\circ}_{HV35}$ increases between drainage events. Depending on melt season intensity and lake basin bathymetry, some lakes will fill up to or close to their 10-year mask extent, while others will fill only a portion of it. The latter will have greater $\overline{\sigma^\circ}_{HV35}$ in SAR imagery before drainage than the former, due to their lower meltwater to ice facies ratio. Such lakes will then exhibit a smaller backscatter increase during drainage, compared to larger lakes with a higher pre-drainage meltwater to ice facies ratio. Thus, the drainage of small lakes within the large 10-year mosaic extent may go undetected. We suspect such occurrences to be rare, however, because small lakes are less likely to retain water into the winter (Lampkin et al., 2020), and their typically shallower depths make them more prone to freeze through (Law et al., 2020) Another factor affecting the magnitude $\overline{\sigma^\circ}_{HV35}$ increase is the lake elevation, which affects its underlying glacier surface properties. For example, at lower elevations, where the underlying lakebed is crevassed or fracture roughened, $\overline{\sigma^\circ}_{HV35}$ will be greater than at higher elevations, for a lake in the wet snow zone, where ice slabs are present, or where there is dry firn.

Challenges remain in developing a fully-automated method for detecting winter lake drainages, without the need for some manual screening to remove false positives. The early winter freeze up, when there are widespread increases in backscatter across all glacier surface facies poses a particular challenge. While our method can detect rapid winter drainages and cascading events at high temporal resolution, it cannot map the areal extent of buried lakes in the winter, as has been done in previous studies (Miles et al., 2017; Schröder et al., 2020; Dunmire et al., 2021, Zheng et al., 2023). Thus, we are unable to compare differences in stored meltwater between winter seasons or assess the completeness of drainage events.

### 2.6.2. Implications of winter lake drainage at Nioghalvfjerdsbræ and Zachariæ

To date, relatively few studies have documented winter lake drainages on the GrIS (Schröder et al., 2020; Benedek & Willis, 2021; Maier et al., 2023). Our study, spanning 10 consecutive winters and using SAR images at a temporal resolution ranging from twice daily to 12-days, presents the first evidence that winter drainage events are common. Thus, winter drainage is an important potential fate for lakes, in addition to summer drainage (Das et al., 2008; Selmes et al., 2011; Tedesco et al., 2013), freeze-over, burial by snow but survival through the winter (Koenig et al., 2015; Lampkin et al., 2020; Law et al., 2020), or complete winter freeze-through (Miles et al., 2017; Hossain et al., 2024).

Lakes have been forming (Howat et al, 2013) and draining (Otto et al, 2022) at increasingly higher elevations in the summer over the last 40 years and are projected to do so under future climate scenarios, with some of the greatest rates of expansion in NE Greenland (Leeson et al., 2015; Ignéczi et al., 2016, Fan et al., 2025). Inland lake expansion could increase the likelihood of surface to bed water transfer to regions that are currently relatively stable (Doyle et al., 2014). This would have hydrological and ice dynamic consequences (Mayaud et al., 2014), although the likelihood of this has been questioned (Poinar et al., 2015). Our 10-year study shows that winter drainage is confined predominantly to lower elevations (<600 m), with no obvious trend towards higher elevations, despite the up glacier summer expansion of lakes at 79NG and ZI glaciers since 1985 (Fan et al., 2025).

Our analysis of melt season conditions using ASCAT-derived melt products and the summer lake drainage dataset of Lutz et al., (2024), indicate that summer conditions influence winter lake drainage occurrence. Specifically, winters following higher melt index summers with more frequent summer drainage events, tend to exhibit fewer lake drainages (Figure 2.9; Table 2.2). Conversely, winters following lower melt index summers show a greater number of drainages across all but the highest elevations (Figure 2.11; Table 2.2). Two linked factors may provide an explanation. First, during higher intensity melt seasons, greater surface to bed melt water inputs may promote water pressurization at the bed, drive higher ice flow velocities, and create more perturbations to the stress field capable of triggering summer drainages. This would likely result in fewer lakes remaining at the end of the summer, decreasing the probability of subsequent winter drainage. This explanation is supported by the positive (negative) correlation between summer (winter) drainages and the melt index (Figure 2.9; Table 2.2). Second, following lower intensity melt seasons, more of the bed would likely remain hydraulically inefficient, with fewer efficient channels

(Banwell et al., 2016; Andrews et al., 2018). After the relatively cool summer of 2018, and the early winter of 2018/19, the subglacial hydrological system is likely to have been particularly inefficient, making it highly sensitive to melt water inputs.

Two of the three cascade events that involved large clusters in our ten-year study occurred during the 2018/2019 winter. One of these was the only late-winter cascade, a seven-lake drainage between 17 and 20 April 2019 (Figure 2.10$c_i$). No other winter had large cluster cascading events during the late winter. The 2017/2018 winter, which also followed a low-intensity melt season, did not exhibit any large cascading events and instead had drainages spaced more evenly throughout the winter. However, this winter season experienced three of the 12 small cascading events observed in this study, the highest number in any single winter. This might demonstrate the effect of cumulative subglacial memory, where the 2018/2019 melt season was preceded by two low intensity melt season while 2017/2018 was only preceded by one.

Surface to bed water transfer from winter drainages may also impact ice sheet stability near the grounding line of Greenland's marine terminating glaciers, as it does for melt season surface inputs that enter subglacial pathways terminating at calving faces (Rignot et al., 2010; How et al., 2017). Indeed Zeising et al., (2024), have suggested that submarine melt water inputs driven by summer lake drainages are an important factor controlling the rate of basal channel growth on the underside of 79NG's floating ice tongue, the largest in Greenland. The occurrence of winter lake drainages represents a potentially important but previously overlooked factor controlling the stability of ice tongues. This will be true particularly for those at low elevations and early in the winter, conditions conducive to the presence of subglacial channels, allowing water to be more likely to reach the terminus.

Although our study does not calculate winter lake areas, the findings of Dunmire et al. (2021) and Zheng et al. (2023) are relevant. In NE Greenland Dunmire et al. (2021) showed that the extent of buried lakes during the 2018/19 winter was only 17% of what it was in 2019/20. Similarly, Zheng et al. (2023) found that winter lake area in 2018/2019 was only ~9% of what it was in 2019/2020. Comparing these findings with ours suggests that a larger winter lake extent does not necessarily correspond to a greater number of winter drainages. In fact, the winter with the most drainages (2018/19) had the smaller of the two observed winter lake extents, indicating that lake presence and area alone is not necessarily a good predictor of winter drainage frequency.

### 2.6.3. Hypothesized mechanisms of cascading winter lake drainages

Over the ten winters, cascading lake drainages account for approximately half of the lake drainages. This is comparable to summer drainage events, where clusters are also common (Morriss et al., 2013; Fitzpatrick et al., 2014; Christoffersen et al., 2018; Hoffman et al., 2018). We observed two modes of winter cascading lake drainage behavior: (1) small cluster cascades involving two or three lakes over short distances (<10 km); and (2) large cluster cascades involving five to seven lakes over greater distances (~25–33 km). Below, we discuss each type of event in detail, focusing on the likely mechanisms involved.

For the small cluster cascades, we suggest that rapid basal cavity opening or slip from an initial lake drainage created horizontal tensile stresses which triggered the drainage of subsequent lakes. This has also been reported by Stevens et al., (2024). Basal uplift or slip, and the horizontal strain rate perturbations they introduce last just a few hours (Das et al., 2008; Tedesco et al., 2012; Doyle et al., 2013; Stevens et al., 2015; Chudley et al., 2019; Lai et al., 2021), and the resultant tensile stresses may be propagated to lakes up, to but no more than, a few kilometers away (Stevens et al, 2024).

The three-lake cascade in September 2017/18 supports this interpretation (Figure 2.11a$_{i}$). Within a ~48-hour period between 16 September 08:58 and 18 September 08:42, lakes L4A and L4B, separated by ~1 km, both drained. L4A and L4B drain within 48 hours of each other in four out of ten winter seasons. This is similar to the findings of Stevens at al., (2024), where two neighboring lakes drained synchronously in 50% of the summers between 2000 and 2023. Favourable ice thickness and basal topography can lead to rapid lake drainage and basal cavity opening placing a neighboring lake basin under tensile stress (Stevens et al., 2024).

Lake L4C, ~8 km down glacier, does not drain simultaneously, indicating tensile stresses during cavity opening beneath L4A and L4B do not instantly reach it. It takes another ~24-hours before L4C drains. Because the modeled drainage pathway passing beneath L4C is on a separate branch to that passing beneath L4A and L4B, it is likely that L4C drains indirectly through the transmission of horizontal stress gradients through the ice as water flows downstream from L4A and L4B rather than directly through the transmission of a high-pressure wave beneath L4C. The spike in velocity along the transect near L1C between 17 and 22 September supports this notion (Figure 2.11a$_{ii}$).

The three-lake cascade between 16 March 17:23 and 17 March 17:31 involving lakes L6A to L6C, all separated by < 3 km, likely provides another instance of tensile-stress-triggered drainages caused by basal cavity opening (Figure 2.11$c_i$). Conversely, the event involving lakes L5A and L5B, between 24 September 18:05 and 26 September 17:49, was less likely to have involved basal cavity opening associated with the first lake drainage setting up tensile stresses that then trigger the second, as the lakes are separated by ~10 km (Figure 2.11$b_i$). Instead, likely mechanisms for their near coincident drainage within ~48 hours are: (1) basal uplift and/or slip caused by subglacial water transfer from L5A to L5B if L5A drained first; or (2) ice stress coupling to L5A from downstream ice acceleration if L5B drained first.

The second and less common mode of clustered lake drainage that involved five to seven lakes over large ~25-33 km distances was observed three times, specifically in September 2018, April 2019, and September 2016. Due to the greater distances and time scales over which they generally occur, they likely result from a combination of mechanisms involving both hydrological and ice dynamic coupling. This is particularly well illustrated for the two 2018/19 winter cascade events.

During the September 2018 cascade event (Figure 2.10$b_i$), L2A and L2B, separated by ~5 km, drained first, within the same 36-hour period. This was followed by L2C and L2D, situated ~14 km downstream, in the subsequent ~15-hour period, and then by L2E and L2F, another ~6 km downstream, in the following ~16-hour period. Because L2A and L2B are sufficiently far apart for tensile stresses from basal cavity opening during one lake drainage to have triggered the second (Stevens et al, 2024), and because the lakes lie along the same subglacial pathway, we suggest that uplift and/or basal slip induced by a subglacial pressure wave moving from L2A to L2B allowed the drainage of the former to trigger the drainage of the latter. We suggest that the same mechanism then triggered the drainage of L2C and L2D, and then L2E and L2F. This interpretation is supported by evidence that elastic stresses from uplift during rapid lake drainages typically persist for only a few hours (Doyle et al., 2013; Chudley et al., 2019; Lai et al., 2021; Stevens et al., 2024). Meltwater from the drainage of L2C or L2D may have contributed to rapid basal cavity opening, helping to trigger the drainage of the other lake, if the two did not drain through the same fracture. The same may be true of lakes L2E and L2F.

The April 2019 cascade also appears to have involved a combination of lake drainage mechanisms. L3A and L3B drained between 17 April 18:29 and 19 April 08:26, with L3C to L3F, located along the modeled subglacial pathway ~8 km downstream from L3A and L3B, draining in the following 10-hour period

(Figure 2.10$c_i$). The close proximity of L3A or L3B (<1 km) suggests the drainage of one may have triggered the other through tensional stresses induced by basal cavity opening. L3C to L3F are located along the modeled subglacial pathway ~8 km downstream from L3A and L3B, suggesting that their later drainage was triggered by uplift and/or basal slip as meltwater from L3A and L3B travelled subglacially. As with the later drainages of the September 18 cascade, the close proximity of lakes L3C-E, mean that tensile stresses associated with cavity uplift due to one lake drainage may have played a role in the drainage of the others. Finally, L3G drained within ~24-hour hours of the drainage of L3C-L3F (Figure 2.10$c_i$). Despite being hydrologically connected to the other lakes via the subglacial pathway, L3G lies upstream of the others and it seems highly unlikely that a pressure wave would travel ~11 km up glacier from L3A to induce uplift or basal slip beneath L3G. Instead, the drainage of lakes L3A to L3F is likely to have accelerated the ice locally, placing the L3G basin under horizontal tension, thereby allowing L3G to drain via hydrofracture (Christoffersen et al., 2018).

Between 5 September 08:43 and 6 September 17:32 2015, lakes L1A to L1E drained on ZI (Figure 2.10$b_i$). The lakes in this cascade are generally spaced farther apart and more evenly than those associated with the 2018/2019 cascades, with the nearest pair ~3.5 km apart and the farthest pair ~32 km apart. Although the exact drainage sequence is not known, it is likely that meltwater flow along the subglacial pathway connecting all five lakes was the primary driver. Lakes L1B and L1C are sufficiently close so that basal cavity opening during rapid drainage of one could have triggered the other, while the remaining lakes are more widely spaced, likely ruling out this possibility. If L1A drained first, the resulting meltwater would travel along the subglacial pathway, triggering the remaining lakes to drain through ice sheet uplift and/or basal slip. Alternatively, if one of the other lakes drained first, the drainage of up glacier lakes may have been triggered via the transmission of horizontal stress gradients within the ice.

In summary, we propose that our smaller drainage cascades involving two or three lakes are more likely to result from a single triggering mechanism, while our larger cascades involving five to seven lakes require a combination of mechanisms. The mechanisms are: (1) enhanced tensile stress from basal cavity opening during rapid drainage of a nearby lake; (2) increased basal uplift and/or slip beneath one lake caused by subglacial water passage from a previously drained upstream lake; (3) increased horizontal strain rates caused by downstream lake drainage and ice acceleration. While a single mechanism or a combination of mechanisms may explain the sequence of drainages within a cascade event, they do not explain the initial lake drainage trigger, nor do they explain isolated winter drainage events. Possible triggers for these include transient strain rate anomalies within the ice (Poinar and Andrews, 2021) or episodic subglacial drainage leading to vertical uplift and basal ice acceleration (Andersen et al., 2023).

### 2.6.4. Ice velocity responses

The large cluster cascades involving five to seven lakes that occurred during early winter (September), caused limited ice acceleration compared to the cascade that occurred in late winter (April). (Figure 2.10$a_i$ to 2.9$b_{iii}$). Since they occurred close to the end of the melt season, it is likely that an efficient subglacial system would have reduced the potential for a lake drainage cascade to induce high basal water pressure and reduced friction (Tedstone et al.,2013; Andrews et al., 2014; Andrews et al., 2018). This aligns with our observations of seasonal slowdowns following the end of most melt seasons (Figure 2.12). Similarly, the small cluster cascades involving two or three lakes that occurred in early winter also had minimal or no impact on velocity (Figure 2.11$a_{ii}$ to 2.10$b_{ii}$). Despite the relatively high temporal resolution of the 6- and 12-day ice velocity products, short-lived perturbations in velocity driven by lake drainage clusters may go unresolved (Poinar & Andrews, 2021; Stevens et al., 2024). However, limited ice velocity responses to late summer / early winter lake drainages have also been observed through in-situ measurements at Helheim Glacier and 79NG. At Helheim Glacier, GPS-derived ice velocities were largely unaffected by a late melt season near-terminus lake drainage event (Stevens et al., 2022). Subglacial modeling suggested that the presence of an efficient subglacial drainage system contributed to the limited response (Stevens et al., 2022). Likewise, a September lake drainage event near the terminus of 79NG induced only a minor, short-lived velocity increase (Neckel et al., 2020).

The late winter cascade in April 2019 was the only event in which we observed an ice velocity increase (Figure 2.10$c_{ii}$). The return to predrainage velocities within the following 6-day image pair, despite the large volume water input to what was likely an inefficient subglacial drainage system, suggests the water was able to be evacuated from the blister that formed beneath the lake to be transported downstream via subglacial pathways.

We find no evidence that the number of winter lake drainages affects the winter monthly velocity magnitudes at 79NG and ZI (Figure 2.12). This suggests that the volume and rate of melt water reaching the ice sheet base during winter drainage events is insufficient to perturb subglacial water pressure and basal friction over a sustained period. The year on year acceleration at ZI, including during winter months, is explained by other factors, notably its rapid retreat in 2012 (Mouginot et al., 2015; Grinsted et al., 2022; Khan et al., 2022).

Maier et al., (2023) documented a late winter 15-lake cascading event at a land terminating region in southwest Greenland using optical imagery. The down glacier propagation of an ice velocity wave was tracked using Differential Interferometry Synthetic Aperture Radar (DInSAR), revealing the subglacial movement of water during the cascade that lasted around a month following the initial lake drainage. Together with our findings relating to a late winter cascade event (Figure 2.10c), these results demonstrate that winter cascade events can trigger ice dynamical responses, with potential consequences for the development of subglacial systems during the following melt season. It is well documented, that during the melt season, increased surface melt water inputs, including from lake drainages, contributes initially to the expansion of subglacial cavities and glacier acceleration, and then to the development of subglacial channels and a transition from high to low ice velocities later in the melt season (Bartholomew et al, 2010; Tedstone et al., 2013; Andrews et al., 2014; Banwell et al., 2016; Andrews et al., 2018). Further investigation is required to determine if winter drainages lead to similar development of subglacial channels capable of influencing ice velocity.

### 2.6.5. Future work

Winter surface lake drainage may significantly impact subglacial drainage systems, with potential implications for ice dynamics. We show that winter lake drainages at ZI and 79NG are common, accounting for 22% of all drainage events observed throughout both summers and winters over an entire seven-year period. Unlike optical datasets, such as MODIS and Landsat with archives extending back multiple decades, no SAR data archive offers sufficient spatial and temporal continuity to observe historical winter lake drainage events prior to Sentinel-1's launch in 2014 and RCM in 2019. It is important, therefore, to extend winter lake drainage investigations to other regions of the GrIS to evaluate their broader prevalence. Winter monitoring is increasingly crucial as surface lakes are projected to expand further inland under ongoing climate change.

Although many studies have documented lake behavior during melt seasons using optical imagery (Sundal et al., 2009; Selmes et al., 2011; Morriss et al., 2013; Fitzpatrick et al., 2014; Williamson et al., 2018; Fan et al., 2025; Lutz et al., 2025), recent studies using satellite SAR and airborne radar have shown that surface lakes may persist through winters and into subsequent melt seasons (Koenig et al., 2015; Miles et al., 2017; Dunmire et al., 2021; Zheng et al., 2023). Furthermore, recent studies, along with our own, highlight winter drainage as a possible fate for surface lakes (Schröder et al., 2020; Benedek & Willis, 2021; Maier et al., 2023). For ZI and 79NG, we were able to combine our winter lake drainage data with those for summer lake drainages from Lutz et al (2024). Future studies should build on this by integrating optical and SAR-based methodologies allowing year-round monitoring of surface lakes to reach a more comprehensive understanding of their life cycles and their impacts on ice sheet dynamics.

Optical remote sensing is highly effective for mapping lake extent, estimating water volume, and detecting drainage during summers (Pope et al., 2016; Williamson et al., 2018). In contrast, SAR uniquely enables the detection of winter drainage events beneath snow cover and areal extent during polar night (Miles et al., 2017; Benedek & Willis, 2021; Zheng et al., 2023). Although low dielectric contrasts between meltwater-saturated snow and firn poses challenges, SAR remains a valuable complement to optical data during the summer, particularly under persistent cloud cover (Schröder et al., 2020). The long-term C-band SAR archive from Sentinel-1, operational since 2014 and bolstered by the recent launch of Sentinel-1C and planned Sentinel-1D mission, offers a strong foundation for advancing winter hydrological studies.

More research is needed to understand how winter lake drainages affect ice dynamics. Studies during the summer show that early meltwater input accelerates ice flow, but this effect often reverses later in the season as the subglacial system becomes more efficient (Sole et al., 2013; Tedstone et al., 2013; Andrews et al., 2014). It is still unclear whether winter lake drainages, like those seen in our study, influence the development of subglacial channels or affect ice flow in the following melt season. Winter lake behavior may also impact melt season surface hydrology. For example, lakes that remain undrained through the winter are more likely to feed into supraglacial river networks in the summer (Lampkin et al., 2020). Thus, winter drainage events could play a key role in controlling the amount and distribution of surface meltwater at the beginning of the summer.

While satellite-derived ice velocity with 6–12 day resolution are valuable, they may not capture the short-lived ice dynamic responses triggered by rapid winter drainage events (Poinar & Andrews, 2021; Stevens et al., 2024). Integrating these observations with high-frequency (<1 hour) in-situ GPS measurements could offer crucial insights into both vertical and horizontal ice deformation, as has been shown for melt season drainages (Das et al., 2008; Doyle et al., 2013; Dow et al., 2015; Chudley et al., 2019; Stevens et al., 2024). Extending such in-situ observations into the winter months could determine whether winter drainage processes differ fundamentally from those in the melt season and provide essential ground truth for interpreting satellite-based assessments of lake drainage behavior across Greenland.

### 2.7. Conclusions

We examined ten years of winter lake drainages on the GrIS using C-band SAR data from Sentinel-1 and the RCM. Using a semi-automated detection algorithm that tracks backscatter changes and includes a new incidence angle normalization method, we combined data from different viewing angles to achieve near-daily resolution. Our results show that winter lake drainages are common at ZI and 79NG in NE Greenland. We identified 90 drainage events across 55 lakes, with some lakes draining multiple times, up to six winters in the ten year period. Drainage frequency of winter generally declined as winter progressed, but event timing and location varied widely.

About half of all observed winter drainages occurred as part of cascading events involving between two and seven lakes. We identified two distinct types: (1) small-scale cascades involving two or three lakes over short distances (<10 km), and (2) large-scale cascades involving five to seven lakes over long distances (~25–33 km). Based on the timing, spatial relationships, and subglacial hydrological context, we propose different triggering mechanisms for each type. Larger cascades likely result from a combination of processes, including tensile stress generation from basal cavity opening, transient increases in horizontal strain due to downstream ice acceleration, and changes in the stress regime due to subglacial hydrological connections, as meltwater passes beneath adjacent lakes.

Winter drainage frequency is influenced by conditions from the preceding melt season, including melt intensity and the frequency of melt season drainage events. Winters with more drainage events often followed cooler melt seasons with fewer summer drainages, while winters with fewer events tended to follow warmer melt seasons with more drainages. Statistical analysis revealed a negative correlation between winter drainage frequency and preceding melt season drainage counts at low- and mid-elevation lakes, but a positive correlation at high-elevations. We also found that the relative importance of winter drainages to preceding summer drainages declines significantly as melt intensity increases. Additionally, lakes that drained during winter were unlikely to drain again in the following summer, and vice versa.

Overall, we found limited evidence of widespread seasonal or long-term velocity increases directly linked to winter drainage events. Most cascading events were associated with only localized or short-lived velocity changes. A notable exception was a seven-lake cascade in April 2019, which produced a clear short-term increase in ice velocity.

Supraglacial lakes play a key role in regulating both surface and subglacial hydrologic systems, with important implications for ice sheet dynamics. While their behavior during the melt season is well documented through optical remote sensing, winter lake drainages have only recently been recognized as a regular and significant part of their lifecycle. Using SAR imagery combined with a novel incidence angle normalization technique, our study offers a comprehensive assessment of winter supraglacial lake drainage frequency and its relationship to preceding melt season conditions on the GrIS. These findings provide a foundation for future research into the year-round dynamics of supraglacial lakes and their evolving role in a warming climate.

# Chapter 3. C- and L-band SAR optimization for detection of buried and open water supraglacial lakes in Northeast Greenland during the melt season

## 3.1. Abstract

Supraglacial lakes form each melt season in surface depressions across the ablation zone of the Greenland Ice Sheet (GrIS). These lakes influence the GrIS surface mass balance (SMB) by reducing surface albedo, altering supraglacial meltwater routing, and injecting meltwater to the ice-sheet bed during drainage events, thereby promoting basal lubrication and triggering basal sliding. Over the past several decades, passive optical sensors have provided much of the foundational understanding of supraglacial lake behavior. However, optical observations are hindered by cloud cover and are unable to detect meltwater beneath snow and ice surfaces. In this study, we analyzed fully-polarimetric and compact-polarimetric C- and L-band synthetic aperture radar (SAR) image pairs acquired during the 2024 melt season over Nioghalvfjerdsbræ (79NG) and Zachariæ Isstrøm (ZI) in Northeast (NE) Greenland. Our analysis first included a detailed comparison of backscatter signatures from open-water and lid-covered lake surfaces, along with surrounding ice-sheet facies including snow, bare ice, crevasse, and slush. We found the SAR parameters VV/HH, linear polarization ratio (LPR), and the degree of depolarization (DoD) provided greater separability between open-water lake areas and surrounding ice-sheet facies compared to single-polarization channels for both C- and L-band. Notably, L-band VV/HH and LPR exhibited strong separability of both open and lid-covered lake surfaces from all surrounding ice-sheet facies. In the second component of our analysis, we assessed the accuracy of supraglacial lake mapping using XGBoost and Random Forest machine-learning classifiers, applied to various feature sets derived from C- and L-band SAR data. Classification performances of XGBoost and Random Forest were generally comparable, with L-band outperforming C-band overall. Inclusion of texture parameters generally improved classification accuracy. Moreover, the promising results obtained from L-band VV/HH and LPR suggest these parameters may enable the detection and mapping of meltwater concealed beneath snow and ice lids on supraglacial lakes. Together, these results demonstrate the utility of SAR-based methodologies for supraglacial lake detection during the melt season, highlighting their potential to complement or independently support optical-based methods.

## 3.2. Introduction

Observations of the GrIS over recent decades indicate an accelerating trend in mass loss, contributing significantly to global sea-level rise (Mouginot et al., 2019; Shepherd et al., 2020). Lakes, represent crucial meltwater features on the ice sheet surface. Each melt season, meltwater generated from snow and firn accumulation flows into rivers, subsequently terminating in depressions to form lakes (Pitcher & Smith, 2019). The locations of these lakes remain relatively constant annually, as they form in surface depressions governed by basal topography and ice thickness (Lampkin & Vanderberg, 2011; Ignéczi et al., 2016, 2018). Lakes serve as significant nodes within the supraglacial hydrological network, influencing the routing and storage of meltwater to subglacial and proglacial environments or retaining meltwater locally on the ice sheet surface (Yang & Smith, 2016; Lampkin et al., 2020; Lu et al., 2021). Despite their importance, supraglacial hydrological networks comprising lakes, rivers, and moulins remain complex and relatively understudied (Yang & Smith, 2016; Yang et al., 2019, 2021). The presence of lakes impacts the mass balance of the GrIS in several ways. Firstly, lakes reduce ice-sheet surface albedo, thereby increasing surface melt rates relative to surrounding areas (Tedesco & Steiner, 2011; Tedesco et al., 2012). Secondly, rapid lake drainages can introduce substantial volumes of meltwater into the subglacial hydrological system, elevating subglacial water pressures, reducing basal friction, and consequently enhancing ice flow (Das et al., 2008; Doyle et al., 2014; Stevens et al., 2015; Christoffersen et al., 2018; Hoffman et al., 2018). Despite these documented impacts, accurately predicting the timing and triggers of lake drainage events remains challenging (Poinar & Andrews, 2021; Stevens et al., 2024). Additionally, while inland expansion of lakes to regions characterized by thicker and slower-moving ice has been observed and modeled (Howat et al., 2013; Ignéczi et al., 2016; Fan et al., 2025), it remains uncertain if this expansion is increasing the frequency of drainage events at higher elevations, and if such events influence the dynamics of otherwise stable regions of the ice sheet (Poinar et al., 2015; Hoffman et al., 2018; Otto et al., 2022).

Satellite-based Earth observations are commonly employed for studying lakes due to their remote locations and highly dynamic nature. Optical wavelengths (visible and NIR) were the first to be adopted for lake studies and continue to be the most frequently utilized (Sundal et al., 2009; Selmes et al., 2011; Arthur et al., 2020). Satellite-based optical sensors provide spatial resolutions ranging from 250 m (MODIS) down to 10 m (Sentinel-2). Distinct spectral properties enable the differentiation of snow, firn, and ice from meltwater in lakes, enabling straightforward lake detection during the melt season. Detection methods range from simple thresholding of spectral indices to sophisticated machine-learning and deep-learning algorithms (Yang & Smith, 2013). MODIS aboard the Terra and Aqua satellites (launched 1999 and 2002 respectively), has a swath of 2330 km and 10 km in the cross track and along track respectively. It has 36 bands, though studies of lakes primarily employ band 1 and 2 covering 620 to 670 nm and 841 to 876 nm respectively. Early studies employed MODIS aboard Terra and Aqua satellites, which now offer over two decades of freely accessible data (Arthur et al., 2020). MODIS's high temporal resolution and broad swath widths have provided valuable insights into lake formation and behavior over extensive regions and periods (Sundal et al., 2009; Selmes et al., 2011; Liang et al., 2012; Morriss et al., 2013; Fitzpatrick et al., 2014). MODIS continues to be relevant in lake studies relating to drainage dynamics (Cooley & Christoffersen, 2017; Poinar & Andrews, 2021) and changes in distribution through out the MODIS archive (Ignéczi et al., 2016). The Landsat archive extends back to 1985 and, with its higher spatial resolution (30 m), enables detailed studies of the inland progression of lakes, though at a reduced temporal resolution compared to MODIS (Gledhill & Williamson, 2018; Otto et al., 2022; Fan et al., 2025). Sentinel-2 is a two-sensor optical constellation, each consisting of 13 bands ranging in spatial resolution of 10 m to 60 m and swath width of 290 km. With to sensors in operation, daily or high temporal resolution is achieved at high latitudes (~ >60° N) during cloud free conditions. Since the launch of Sentinel-2A in 2015 and Sentinel-2B in 2017, the increased availability of medium-resolution optical data has facilitated numerous methodological advancements.

NDWI has emerged as a robust yet straightforward approach for lake detection (Yang & Smith, 2013; Miles et al., 2017; Williamson et al., 2017, 2018; Otto et al., 2022; Zhang et al., 2023). Machine-learning approaches for lake mapping, particularly those using Random Forest (Dirscherl et al., 2020; Wendleder et al., 2021; Dell et al., 2022) and deep-learning methods (Yuan et al., 2020; Lutz et al., 2023) have proven effective. Optical sensors also facilitate estimates of lake depth and volume through the use of a physically based radiative transfer equation (RTE) (Sneed & Hamilton, 2007; Pope et al., 2016; Williamson et al., 2017) and in-situ based empirical models (Box & Ski, 2007; Tedesco & Steiner; 2011; Legleiter et al., 2014). Recent work employing ICESat-2 has made progress in assessing accuracies and improving volume retrievals using these methods. Evaluation of depths retrieved used the commonly employed RTE method reveal is tends to overestimate depth in the green band and underestimate it in the red band of Sentinel-2 (Melling et al., 2024). Methodologies employing ICESat-2 to improve depth retrieval using passive optical sensors include histogram-based thresholding to separate lake surface and bed returns (Fair et al., 2020) and machine learning (Zhou et al., 2025; Fan et al., 2025). However, optical sensors face several limitations, such as prolonged observational gaps due to cloud cover, resulting in uncertainties or temporal aliasing around the timing and mechanisms of lake drainage (Fitzpatrick et al., 2014; Cooley & Christoffersen, 2017; Stevens et al., 2024). Additionally, optical wavelengths cannot penetrate below snow or ice surfaces that can be present on lake surfaces, which likely leads to underestimations of lake area compared with studies using SAR (Schröder et al., 2020).

SAR sensors emit electromagnetic radiation within the microwave region, enabling them to penetrate cloud cover and other media in glacial environments, illuminating targets independently of sunlight, thus overcoming limitations associated with optical sensors. Radar pulses interact with surface and shallow subsurface features, returning backscatter signals influenced by geometry, roughness, dielectric properties, and SAR system parameters (Ulaby et al., 1984; Hallikainen et al., 1986; König et al., 2001). Consequently, in ice sheet environments, spaceborne SAR has become widely utilized for mapping ice sheet facies and glacier zones, exploiting the unique backscatter signatures of features such as firn, ice slabs, bare ice, and crevassed regions (Fahnestock et al., 1993; Cooper & Smith, 2019; Barzycka et al., 2023; Culberg et al., 2024). C-band SAR has been more widely adopted for studies during the winter. Early instances of SAR-based lake observations involved manual delineation of buried lakes from winter C-band ASAR scenes (Johansson & Brown, 2012). ASAR was a SAR sensor capable of single and dual-pol polarisation modes at spatial resolutions up to 30 m. Poinar et al. (2015) qualitatively observed wintertime lakes using both C-band and notably L-band imagery. The adoption of C-band (5.3 GHz) SAR for mapping lakes expanded significantly following the Sentinel-1 mission launch in 2014 and widespread availability of SAR data. Subsequently, Miles et al. (2017) employed a threshold-based classification algorithm using Sentinel-1 HH and HV backscatter within melt-season lake extents detected using optical sensors to track lake extents from the melt season into winter. Building upon this, Zheng et al. (2023) applied a dynamic thresholding approach for mapping lake extents across Greenland over multiple winter seasons, while Dunmire et al. (2021) fused melt-season Sentinel-2 data with winter Sentinel-1 imagery to map winter lake extents. Other studies analyzed C-band HH and HV backscatter time series, from Sentinel-1, within melt-season lake extents detected using optical sensors to detect winter drainage events (Benedek & Willis, 2021). While dry winter conditions have enabled greater use of C-band SAR during the winter, attempts to map lakes during the melt season remain limited due to challenges relating to poor dielectric contrast with surrounding ice sheet facies resulting in reduced backscatter due to signal attenuation and diminished scattering from snow and firn volumes (Ulaby et al., 1984; Hallikainen et al., 1986). During the melt season, the low dielectric contrast between lakes and surrounding saturated snow and firn produces overlapping backscatter signatures, complicating differentiation. This has led to challenges in mapping using thresholding (Miles et al., 2017) and Bayesian classification schemes (Schröder et al., 2020). Deep learning has demonstrated the ability for melt season lake detection, though lack analysis in relation to scattering mechanisms (Dirscherl et al., 2020; Jiang et al., 2022).

Assessments and utilization of SAR parameters for mapping lakes, beyond C-band HH and HV polarization channels, remain limited. The HH polarization is primarily affected by surface scattering, while HV polarization is sensitive to multiple and volume scattering (Freeman & Durden, 1998). Within lake studies, HV polarization is often preferred due to its stronger contrast between firn and snow, where volume scattering dominates, and water, which exhibits no volume scattering due to negligible penetration depth (Miles et al., 2017). A primary limitation of C-band SAR during melting conditions is limited penetration depth of this frequency into firn and ice. In glacial environments, C-band and L-band penetrate approximately 9 m and 14 m into dry firn, and around 1 m and 3 m into ice, respectively (Rignot et al., 2001). The penetration depth reduces but also becomes particularly pronounced in snow and firn containing liquid water for C-band relative to L-band. L-band SAR can penetrate saturated snow roughly 15 times deeper than C-band, allowing for comparatively higher volume scattering contributions in L-band (Ulaby et al., 1984; Casey et al., 2016). Incorporating additional polarization channels and polarimetric parameters beyond HH and HV, has demonstrated benefits in mapping ice types, surface roughness, and melt ponds across varying melt and winter conditions (Casey et al., 2016; Cafarella et al., 2019; Mahmud et al., 2022; Tavri et al., 2023). For smooth, specular surfaces (Bragg surfaces), VV polarization dominates relative to HH, resulting in an elevated co-polarized ratio (VV/HH). In contrast, rough, or volume scattering, surfaces exhibit VV/HH ratios close to 1, and double-bounce scattering may result in VV/HH ratios less than 1 (Cloude & Pottier, 1996; Freeman & Durden, 1998). This polarimetric theory has been successfully applied in sea ice studies to estimate surface melt pond fraction, the proportion of melt pond coverage in a sea ice area, leveraging distinct VV/HH signatures of melt ponds, relative to bare and snow-covered ice, during early and advanced melt phases (Scharien et al., 2012; Scharien et al., 2014).

Recent SAR missions utilizing modes beyond dual-polarization HH and HV, including RCM, SAOCOM-1, NISAR, and ALOS-2/PALSAR-2, now offer various imaging modes providing, e.g., compact polarimetric (CP), fully polarimetric (FP), and dual-pol (VV/HH) data. Despite these advancements, SAR frequencies and polarimetric parameters, either as a complement to, or beyond, C-band HH and HV, remain largely unexplored for mapping lakes. Additionally, the recent launch of the NISAR mission in July 2025, followed by the planned ROSE-L mission in 2028, will significantly enhance the availability of frequent, open-access, L-band SAR data of ice sheets. These compliment existing L-band missions including ALOS-2/4 and SAOCOM-1 which are taskable and capable of acquiring FP data. As such, this study addresses the following objectives:

1. Determine the optimal frequency and polarizations for separation of open water and ice-covered lakes from surrounding ice sheet facies during melt conditions.
2. Evaluate which method among Random Forest and XGBoost classifications best maps lake extents during the melt season and identify the most effective SAR parameters for this purpose.

## 3.3. Study area and data

### 3.3.1. Study area

We examined lakes located at the outlet glaciers 79NG and ZI in NE Greenland (Figure 3.1). NE Greenland currently holds approximately 18% of the total GrIS lake volume, with projections indicating an increase to approximately 30–35% by the end of the century (Ignéczi et al., 2016). During the melt season from early June to late August, expansive networks of supraglacial rivers and lakes form at elevations ranging from approximately 400 m to 1500 m above sea level (Sundal et al., 2009; Lu et al., 2021; Hochreuther et al., 2021; Turton et al., 2021). Peak lake area and volume typically occur in early August (Hochreuther et al., 2021; Kanzow et al., 2025), while peak lake elevations and numbers commonly occur between 850 m and 1000 m above sea level (Hochreuther et al., 2021; Turton et al., 2021). Lakes have been documented to drain during both melt and winter seasons (Schröder et al., 2020; Lutz et al., 2025), as well as persist undrained for multiple years, becoming partially or entirely buried under snow and ice lids (Koenig et al., 2015; Lampkin et al., 2020).

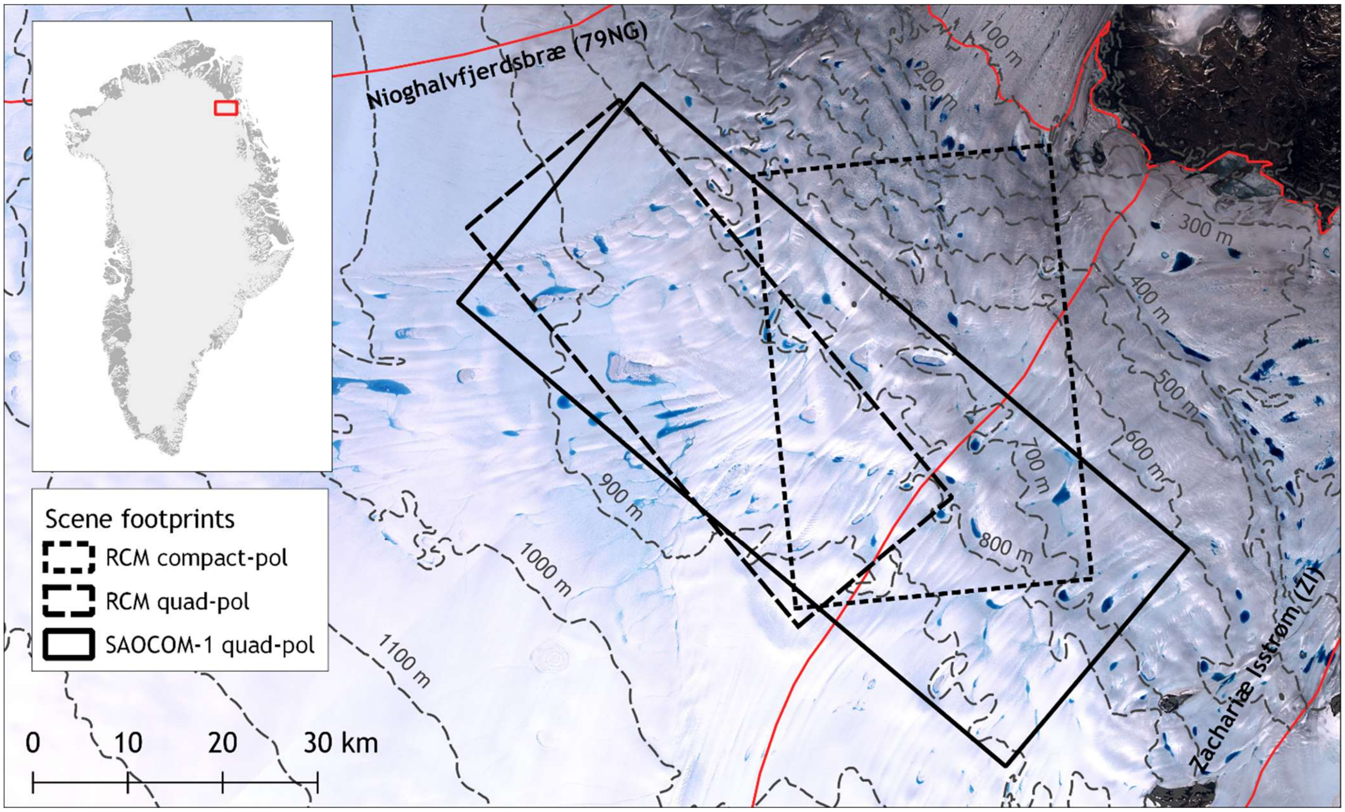


**Figure 3.1.** Study area including Nioghalvfjerdsbræ (79 NG) and Zachariæ Isstrøm (ZI) glaciers shown using red outlines overlaid on a Sentinel-2 RGB mosaic from imagery acquired on 20 July 2024 at 15:38 UTC (Mouginot & Rignot, 2019). Footprints of the RCM compact-pol (C-band; 21 July 2024, 08:30 UTC) and quad-pol (12 July 2024, 18:27 UTC) images, along with SAOCOM-1 (L-band; 12 July 05:41 UTC and 20 July 05:44 UTC).

### 3.3.2. SAR data

Two spatially and temporally overlapping C-band (5.405 GHz, λ = 5.5 cm) and L-band (1.275 GHz, λ = 23.5 cm) SAR image pairs were tasked during July of the 2024 melt season for this study (see footprints in Figure 3.1). Each were acquired at a different stage of the melt season with unique environmental conditions. Sensor characteristics and acquisition details are summarized in Tables 3.1 and 3.2, respectively. The first pair was acquired on 12 July (hereafter referred to as case 1), with a temporal difference of 12 hours and 46 minutes between acquisitions. L-band data in StripMap FP mode (HH, HV, VV, VH) were obtained from SAOCOM-1, part of Argentina's Earth observation satellite constellation managed by CONAE. Corresponding C-band data, also in StripMap FP mode, were acquired from RCM. The spatial resolution for L- and C-band data was 10.0 m × 6.0 m and 6.5 m × 2.9 m, in azimuth and range, respectively, with swath widths of 29 km for L-band and 20 km for C-band. Incidence angle range of the L-band image was 27.2 – 29.6°, and 41.8 – 43.1° for C-band (Table 3.2). The second image pair (hereafter referred to as case 2) was acquired on 20-21 July, with a temporal difference of 26 hours and 45 minutes. The C-band image was acquired in Medium-resolution CP mode, with a spatial resolution of

18.2 m × 1.2 m and a swath width of 30 km. A C-band CP mode image was used due to a lack of FP image availability. The L-band imagery was acquired in the same mode and orbit as case 1. Incidence angle of the CP mode images was 45.6 – 47.4°. Due to the lack of available CP L-band imagery around this date, CP data were simulated from the available FP data (details in Section 3.1). The Noise-Equivalent Sigma Zero (NESZ) values for the L-band StripMap images are −34 dB for FP mode, and −24 dB and −25 dB for C-band FP and CP modes, respectively (Table 3.3). All images were acquired in Single Look Complex (SLC) format. RCM data were sourced from Natural Resources Canada (https://www.eodms-sgdot.nrcan-rncan.gc.ca/), and SAOCOM-1 imagery was ordered from the CONAE SAOCOM Catalogue (https://catalog.saocom.conae.gov.ar/catalog/#/).

### 3.3.3. Optical data

Two optical images were acquired to coincide with case 1 & 2 (Table 3.2). For case 1, a Landsat 8 image was acquired on 13 July at 20:44 UTC. While Sentinel-2 has higher spatial resolution, no cloud-free scenes were available. The Landsat 8 Tier 2 Level 1TP (L1TP) top-of-atmosphere (TOA) reflectance image was utilized. A Tier 1 image, with geometric Root Mean Square Error (RMSE) tolerances ≤12 m was not available, though we assessed the available Tier 2 image geometric RMSE of 16.4 m and found it acceptable. For case 2, a Sentinel-2 Level-1C TOA reflectance image was acquired on 20 July at 15:38 UTC. Visible bands B2, B3, B4, and Near-Infrared (NIR) were utilized for both optical datasets to facilitate region of interest (ROI) selection (Section 3.3.2) and classification training and validation (Section 3.3.3.2). Landsat and Sentinel-2 imagery have been extensively used in previous studies for mapping meltwater features in the GrIS environment, including slush (Yang & Smith, 2013; Dell et al., 2022) and lakes (Miles et al., 2017; Benedek & Willis, 2021; Otto et al., 2022).

**Table 3.1.** Overview of C- and L-band SAR sensors and modes used. NESZ refers to the noise equivalent sigma zero, i.e., noise floor.

| Sensor & mode | SAOCOM-1 (L-band) StripMap FP | RCM (C-band) StripMap FP | RCM (C-band) Medium resolution CP |
|---|---|---|---|
| Center frequency (λ) | 1.275 GHz (23.5 cm) | 5.405 GHz (5.5 cm) | 5.405 GHz (5.5 cm) |
| Polarizations | HH + HV + VH + VV | HH + HV + VH + VV | RCH + RCV |
| Resolution ($r$† × $a$‡) | 10.0 m x 6.0 m | 6.5 m x 2.9 m | 18.2 m x 1.2 m |
| NESZ (nominal) | -34 dB | -24 dB | -25 dB |
| Swath width | 29 km | 20 km | 30 km |
| Operational years | Oct 2018 - present | June 2019 - present | June 2019 - present |

Notes:
† Range resolution
‡ Azimuth resolution

**Table 3.2.** SAR and Optical image list. Incidence angle ($\theta$) range for each image are provided. ERA5 2 m air temperature (°C) and 10 m wind speed (m/s) at time of acquisition from Figure 3.2 are provided.

| ID | Sensor | Date (YYYY-MM-DD) | Time (UTC) | $\theta$ range (°) | Air temp. (°C) | Wind speed (m/s) |
|---|---|---|---|---|---|---|
| SAO-1 | SAOCOM-1 FP | 2024-07-12 | 05:41:23 | 27.2 – 29.6 | -1.0 | 7.4 |
| RCM-1 | RCM FP | 2024-07-12 | 18:27:48 | 41.8 – 43.1 | -0.9 | 5.9 |
| L8 | Landsat TOA | 2024-07-13 | 20:44:54 | 2.2 – 4.4 | 0.6 | 3.3 |
| SAO-2 | SAOCOM-1 FP | 2024-07-20 | 05:44:57 | 27.2 – 29.6 | 1.5 | 7.6 |
| RCM-2 | RCM CP | 2024-07-21 | 08:30:08 | 45.6 – 47.4 | 3.6 | 8.2 |
| S2 | Sentinel-2 TOA | 2024-07-20 | 15:38:19 | 1.6 – 5.0 | 4.6 | 7.0 |

### 3.3.4. Weather data

Temperature and wind speed data were obtained from the ERA5 v5 global reanalysis dataset provided by the Copernicus Climate Change Service (Hersbach et al., 2020). ERA5 provides a wide range of climate variables from 1950 onwards, gridded at a spatial resolution of 31 km. Hourly data of 2 m air temperature and 10 m wind speed were acquired from 1 June to 31 August 2024. Additionally, automatic weather station data from the Programme for Monitoring of the GrIS (PROMICE) were used (Fausto et al., 2021), specifically, data from the KPC_U station, located approximately 90 km northwest of the study area at an elevation of 870 m. At this station, air temperature and wind speed are recorded at a height of 2.6 m. ERA5, and KPC_U station data are presented in Figure 3.2.

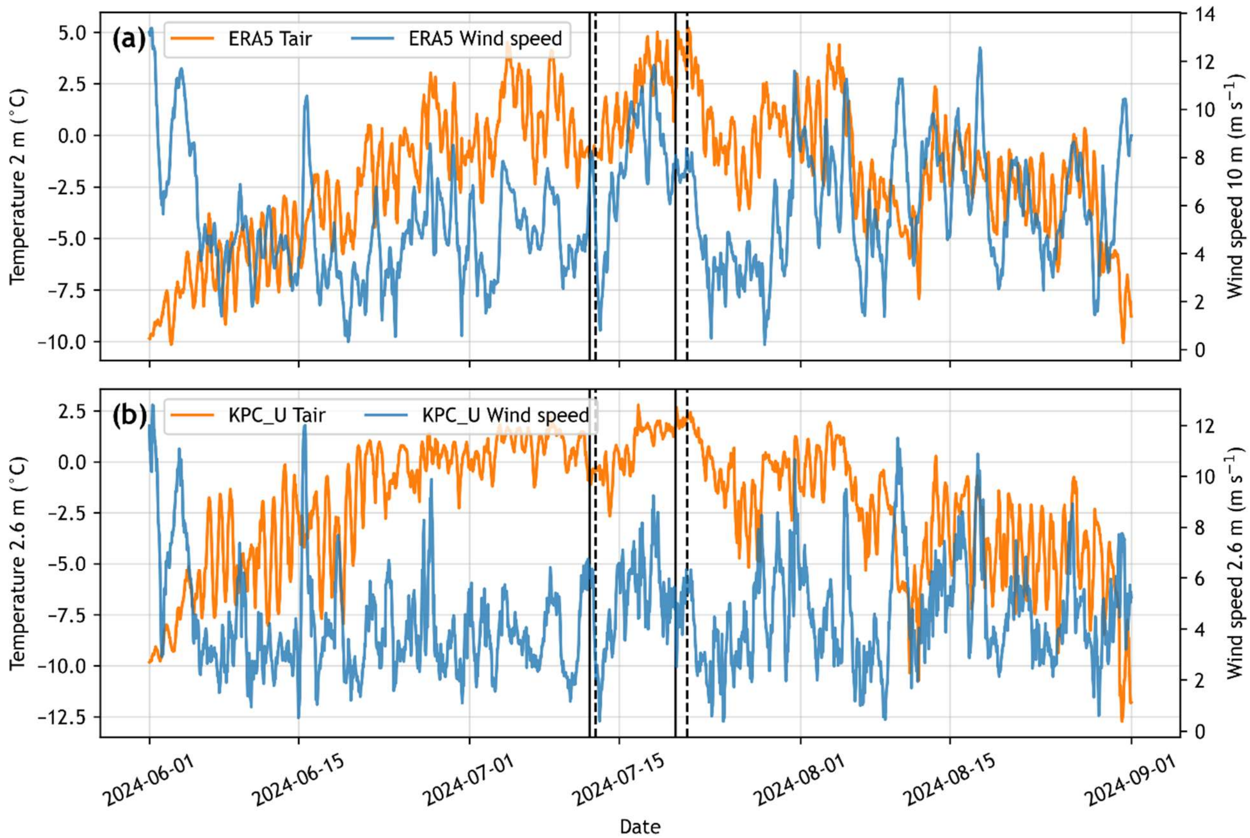


**Figure 3.2.** (a) ERA5 2 m air temperature and 10 m wind speed; (b) PROMICE KPC_U station in situ temperature and wind speed at 2.6 m height. Solid vertical lines mark SAOCOM acquisitions; dashed lines mark RCM acquisitions.

## 3.4. Methods

### 3.4.1. SAR image processing and polarimetric parameters

All SAR images in SLC format were radiometrically calibrated to normalized radar cross-section sigma naught (σ°), terrain-corrected using the 30 m Copernicus DEM, and projected onto the NSIDC Sea Ice Polar Stereographic North projection (EPSG: 3413) with a pixel spacing of 10 m using nearest neighbour resampling. To reduce speckle noise, an edge-aware Lee Sigma speckle filter with an 11 × 11 window and a 5 × 5 target window was applied (Lee et al., 2009). Image processing was conducted using ESA's SNAP 11 software.

For case 1, HV, HH, and VV/HH were utilized. For case 2, the CP channels right-circular horizontal receive (RCH), and right-circular vertical receive (RCV) were used, alongside CP parameters including the linear polarization ratio (LPR) and degree of depolarization (DoD). For our analysis we considered LPR as a CP analogue to VV/HH used in case 1, and we use DoD in place of a missing C-band HV channel because both respond strongly to volume- and surface-scattering effects. We note, however, they are not identical with HV being a direct single channel measure of cross-pol power, whereas DoD describes how incoherent the backscatter is, factoring in RCH and RCV channels. LPR and DoD have demonstrated effectiveness in discriminating sea ice types during winter and melt conditions (Singha & Ressel, 2017; Nasonova et al., 2018; Tavri et al., 2023). Additionally, L-band HV, HH, and VV/HH were included to enable comparison with case 1.

Grey-level Co-occurrence Matrix (GLCM) texture parameters (Haralick et al., 1973) were computed for all SAR image bands using SNAP 11 software. Three contrast-related GLCM metrics (Contrast, Dissimilarity, Homogeneity), two orderliness metrics (Entropy, Angular Second Moment), and one statistical metric (Correlation) were derived (Appendix B Figure B.1 to B.4) A window size of 9 pixels, a quantization level of 64, and a displacement of 4 pixels were empirically determined and subsequently used for deriving the GLCM matrix from which metrics were derived. A quantization of 64 was considered sufficient through iterative testing and has been used previously in SAR-based sea ice research (Mahmud et al., 2022; Scharien & Nasonova, 2022). No directionality was selected for GLCM calculation after visual inspection of lake shapes in optical imagery indicated no significant directional preference (Hall-Beyer, 2017).

### 3.4.2. Backscatter characteristics and feature separability

Towards objective 1, six classes were identified, including two lake classes, one class for the open water or subaerial portions of lakes (OW), and one for lake lids (LL), which have been observed to partially or entirely cover lakes and persist throughout the melt season (Koenig et al., 2015; Lampkin et al., 2020). The four ice sheet facies classes selected were slush (SL), snow (SN), crevasse (CR), and bare ice (BI).

ROIs consisted of 200 m × 200 m boxes (400 pixels at 10 m resolution), within overlapping footprints of corresponding SAR image pairs of cases 1 and 2. A minimum of three ROIs were identified per class. Class identification was supported by corresponding optical imagery. More information about the identification of each class is provided below. ROI examples from cases 1 and 2 can be found in Figure 3.3 and 3.4. ROI data for each class were then used for feature separability analysis and for analyzing backscatter characteristics.

The OW class was mapped with the NDWI, which exploits the strong absorption of longer optical wavelengths by liquid water in contrast to the high reflectance of snow and ice. In this study we used $NDWI_{ice}$, a variant of the Normalized Difference Water Index specifically adapted for the ice-sheet environment (Yang & Smith, 2013) and widely applied to meltwater detection across Greenland (Williamson et al., 2017, 2018; Otto et al., 2022; Zhang et al., 2023). Initially, a strict threshold was established by averaging $NDWI_{ice}$ values across 10 manually identified lakes, then empirically adjusted to exclude streams and slush. A threshold of $NDWI_{ice} > 0.30$ was used for the 13 July Landsat 8 image, and $NDWI_{ice} > 0.25$ for the 20 July Sentinel-2 image. OW ROIs were subsequently defined within identified lake boundaries. A secondary mask was defined using moderate $NDWI_{ice}$ values to identify SL, setting a lower threshold of 0.12 for both optical images and an upper threshold equal to the respective strict lake boundary thresholds. ROIs classified as SL were selected to contain at least 75% pixels within this range of $NDWI_{ice}$ values. Although the threshold of 0.12 efficiently identifies SL, it can also include supraglacial streams (Yang & Smith, 2013). To reduce potential inclusion of streams, elongated linear features identified in thresholded masks or RGB imagery were excluded from SL ROIs. Despite these precautions, small, braided streams that are narrower than a Sentinel-2 or Landsat pixel may still be classified as slush.

For identification of SN, BI, and CR classes, a global threshold was applied to the near infrared (NIR) band from Sentinel-2 and Landsat imagery (Ryan et al., 2019; Yang et al., 2019; Lu et al., 2021). Empirical threshold selection was guided by manual interpretation of RGB imagery. Following Lu et al., (2021), we found a threshold of NIR > 0.58 for the 13 July Landsat 8 and 20 July Sentinel-2 image was effective in identifying snow covered areas. SN ROIs were identified in areas above the NIR threshold, while BI ROIs were positioned below. During selection, moderate and high $NDWI_{ice}$ threshold masks were referenced to avoid overlaps between SL, OW, SN, and BI classes. CR ROIs were manually delineated using visual interpretation of RGB imagery.

Separability between classes was assessed using the two-sample Kolmogorov-Smirnov (K-S) test. The K-S test is nonparametric and suitable for backscatter intensity since it does not assume a specific distribution of the test data. The K-S test compares cumulative distribution functions of paired samples, yielding a test statistic (D) ranging from 0 (no separability) to 1 (perfect separability). Prior to testing, 500 random samples per class were drawn, and samples beyond a z-score of ±3 were excluded to ensure robustness. A description of expected scattering mechanisms and C- vs. L-band differences are outlined in Table 3.3.

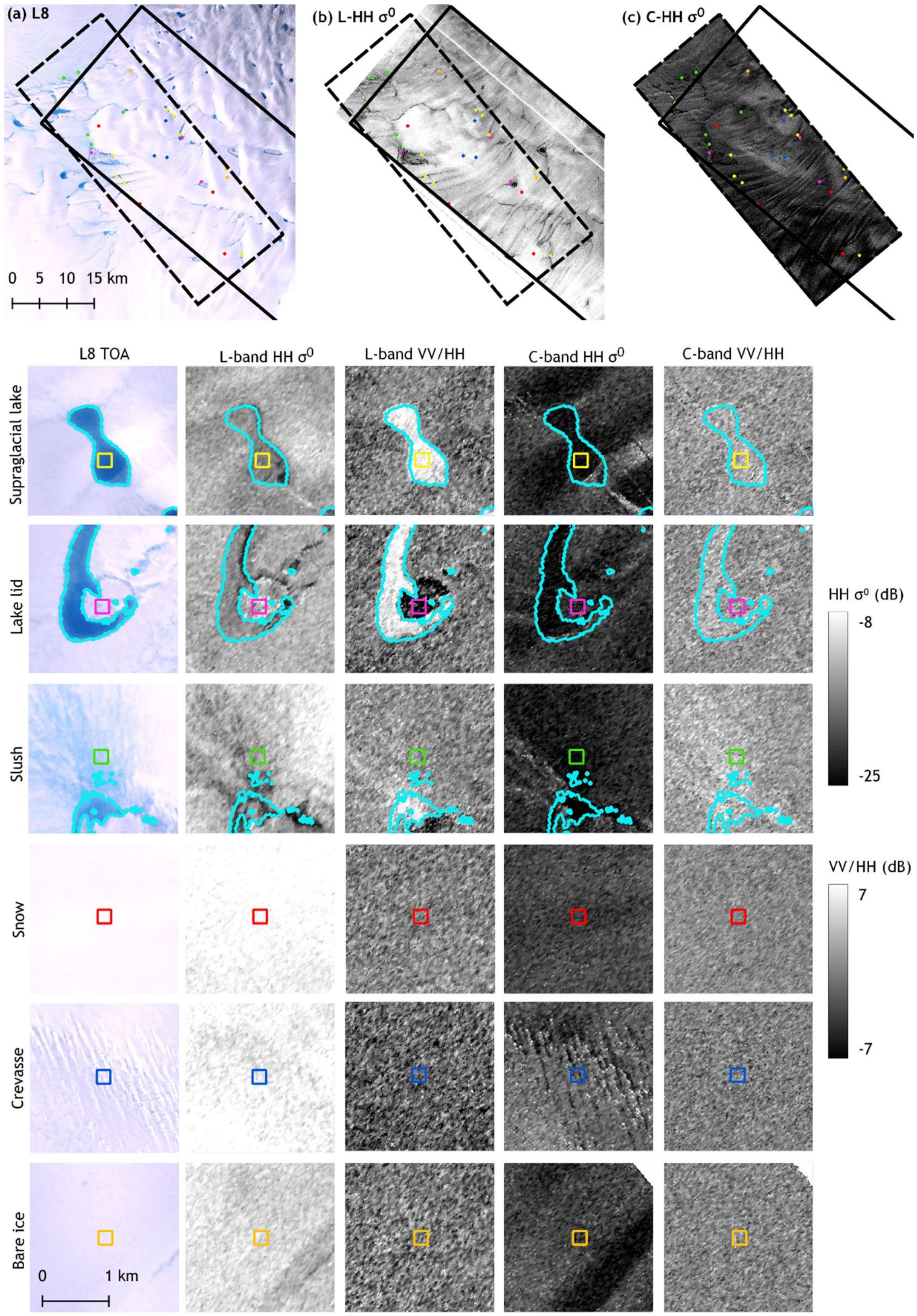


**Figure 3.3.** Case 1 ROIs examples used to sample the six surface classes: supraglacial lake (OW), lake-lid (LL), slush (SL), snow (SN), crevasse (CR), and bare ice (BI) from case 1 (12 July 2024 FP image pair). (a) Landsat-8 (L8) RGB (13 July) with RCM footprint (dashed) and SAOCOM footprint (solid). (b) SAOCOM-1 HH image; (c) RCM HH image, each with the same footprints. Lower panel: class ROIs displayed across Landsat TOA, L-band HH, L-band VV/HH, C-band HH, and C-band VV/HH with high $NDWI_{ice}$ threshold polygons overlaid in cyan. Grey scales (right) correspond to HH and VV/HH ranges shown.

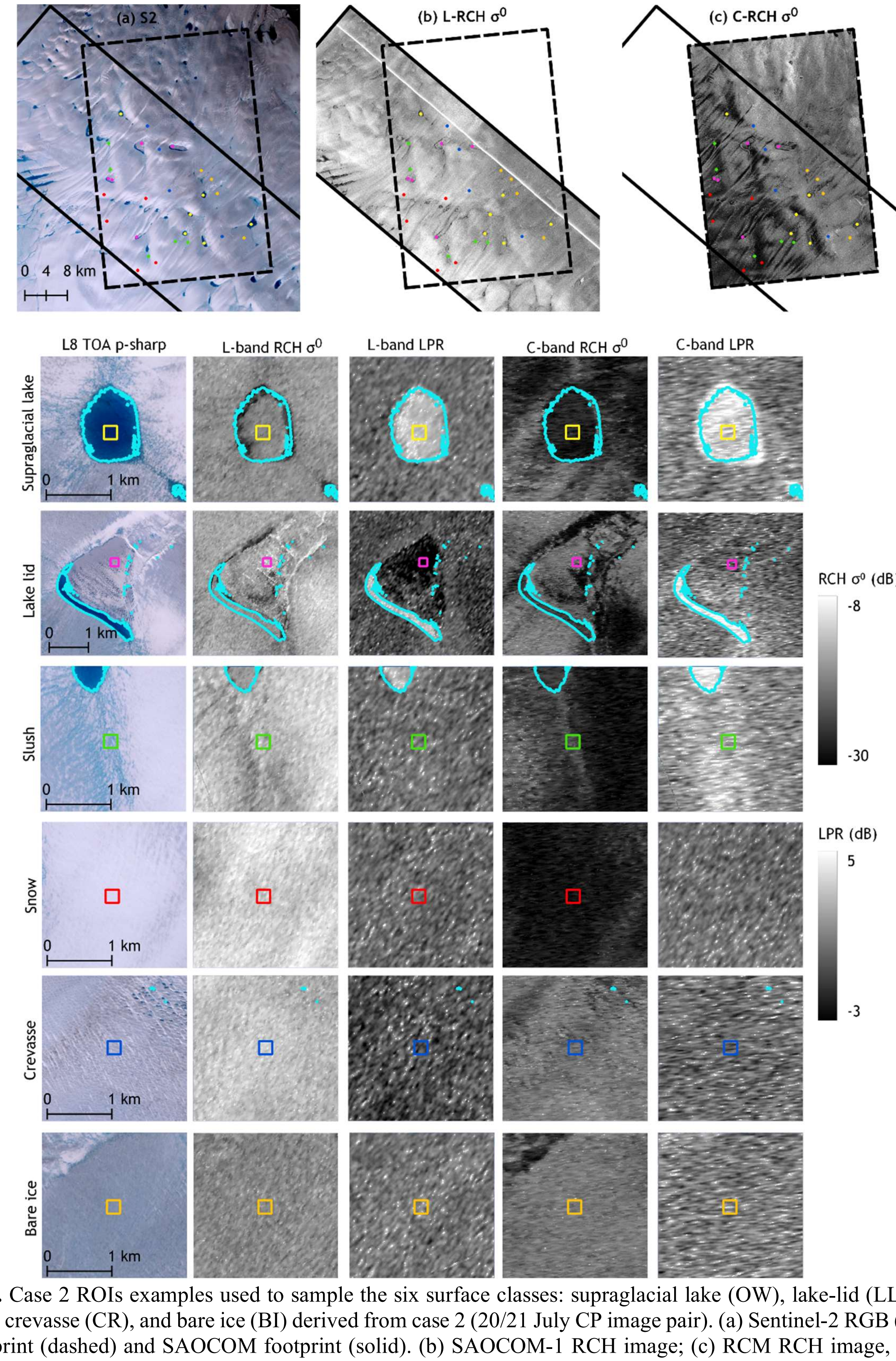


**Figure 3.4.** Case 2 ROIs examples used to sample the six surface classes: supraglacial lake (OW), lake-lid (LL), slush (SL), snow (SN), crevasse (CR), and bare ice (BI) derived from case 2 (20/21 July CP image pair). (a) Sentinel-2 RGB (20 July) with RCM footprint (dashed) and SAOCOM footprint (solid). (b) SAOCOM-1 RCH image; (c) RCM RCH image, each with the same footprints. Lower panel: class ROIs displayed across Landsat TOA, L-band HH, L-band VV/HH, C-band HH, and C-band VV/HH with high $NDWI_{ice}$ threshold polygons overlaid in cyan. Grey scales (right) correspond to HH and VV/HH ranges shown.

**Table 3.3.** Expected scattering mechanisms and frequency differences for the lake classes, open water (OW) and lake lids (LL), and for the ice-sheet classes slush (SL), snow (SN), crevasse (CR), and bare ice (BI).

| Class | Scattering mechanism | C- vs. L-band differences |
|---|---|---|
| Open water (OW) | Specular and Bragg scattering. | C-band is more sensitive to small-scale wind roughening (cm ripples), while L-band responds to longer waves (dm scale). |
| Lake lids (LL) | Combination surface, volume, and double bounce. | L-band penetrates deeper into the lid and interacts with horizontal snow/ice layers, while C-band is more surface-sensitive. |
| Slush (SL) | High liquid water content restricts penetration; dominant surface scattering with limited volume contribution. | C-band backscatter is dominated by surface scattering due to shallow penetration; L-band penetrates slightly deeper and samples upper centimeters. |
| Snow (SN) | Greater penetration than slush with significant volume scattering. | C-band is more sensitive to changes in liquid water content; L-band is better at capturing dry snow volume scattering. |
| Crevasse (CR) | Geometric structures produce double-bounce; additional volume scattering may occur. | Both bands show similar scattering behavior. |
| Bare ice (BI) | Combination of surface and volume scattering. | L-band penetrates deeper, making it more sensitive to internal volume features; C-band emphasizes surface roughness. |

### 3.4.3. Supraglacial lake classification

To optimize C- and L-band SAR for melt season lake mapping, two widely utilized decision tree-based machine learning algorithms were used, with varying input feature sets: Random Forest (Breiman, 2001) and eXtreme Gradient Boosting (XGBoost; Chen & Guestrin, 2016). All classification analyses were performed separately for cases 1 and 2 and classification accuracy was used to assess classification performance.

#### 3.4.3.1 Image classifiers

Random Forest and XGBoost have both been successfully applied in remote sensing studies of lakes using optical (Dirscherl et al., 2020; Dell et al., 2022; Wang & Sugiyama, 2024; Zhou et al., 2025) and SAR imagery (Wendleder et al., 2021). The Random Forest is a decision tree-based ensemble machine learning algorithm (Breiman, 2001). A user-defined number of trees are created with a training dataset, each with its own bootstrap subset of the training data. Furthermore, a random subset of feature variables is selected at each node, with a single feature then being selected using the one with the lowest Gini impurity. Gini impurity is a measure of how well features at each node split the training data and is essential in building the decision trees that are accurate predictors. Each tree then produces a vote on the predicted class. Votes of all trees are then aggregated, and the mean is taken to provide a final class. By including randomness during the selection of training observations for each tree and feature variables at each node, the algorithm is robust and resistant to overfitting than non-ensemble decision trees.

The second classification method is XGBoost, an advanced tree-based algorithm (Chen & Guestrin, 2016). Unlike Random Forest, XGBoost sequentially builds trees by correcting the residual errors from preceding trees. After an initial tree is created using a subset of the training data and features, residuals between predicted and actual values guide the construction of subsequent trees. Each tree independently predicts class probabilities, and the aggregated probabilities determine the final classification outcome. Training data generation and parameter optimization for both classifiers are described below.

#### 3.4.3.2 Training data and Random Forest and XGBoost parameter tuning

Two distinct training and validation datasets were created for cases 1 and 2. Binary labels were collected for lake (open water, OW) and non-lake (i.e., merged ice facies SL, SN, CR, BI) categories. Due to limited unique areas available for sampling LL, we focused exclusively on classifying OW areas against the surrounding ice sheet. Label collection was guided by the $NDWI_{ice}$ derived masks described in Section 3.3.2. Lake labels were obtained from manually drawn polygons within areas exceeding the high NDWIice threshold, whereas non-lake labels were taken from polygons below this threshold. Samples were collected independently of ROIs from the separability analysis as described above in section 3.4.2. For case 1, a balanced sample of 3000 lake pixels and 3000 non-lake pixels were selected. For case 2, 2000 pixels for each class were selected.

To assess classifier performance in case 1, we defined eight feature sets that incrementally combine polarimetric channels and texture metrics. Sets (a) to (d) are built on HH, HV, and VV/HH while sets (e) to (h) start from VV and HH: (a) HH + HV; (b) HH + HV + all GLCM textures; (c) HH + HV + VV/HH; (d) HH + HV + VV/HH + all textures; (e) VV + HH; (f) VV + HH + all textures; (g) VV + HH + VV/HH; and (h) VV + HH + VV/HH + all textures. For case 2 we evaluated four CP C-band sets that incrementally add texture and ratio information: (i) RCH + RCV; (j) RCH + RCV + all GLCM textures; (k) RCH + RCV + LPR and DoD; and (l) RCH + RCV + LPR, DoD + all textures. In parallel, eight L-band FP sets were tested, following the same structure used in case 1: (m) HH + HV; (n) HH + HV + textures; (o) HH + HV + VV/HH; (p) HH + HV + VV/HH + textures; (q) VV + HH; (r) VV + HH + textures; (s) VV + HH + VV/HH; and (t) VV + HH + VV/HH + textures.

Model training utilized the scikit-learn Python package for Random Forest (Pedregosa et al., 2011) and the XGBoost Python package (Chen & Guestrin, 2016). During training, samples were partitioned into 70% training and 30% testing subsets. Parameter optimization for both classifiers was conducted using scikit-learn's RandomizedSearchCV. RandomizedSearchCV allows for testing of random combinations of model parameters and the outputs of an F1 score for each iteration. This was conducted for each model and feature set.

#### 3.4.3.3 Accuracy assessment

To evaluate classification accuracy, a separate validation dataset containing 500 random validation points for each class was created. Lake validation samples were selected within polygons exceeding the high NDWIice threshold, while non-lake samples were randomly selected from areas below this threshold.

Class accuracy was quantified using precision (P) and recall (R) (Dirscherl et al., 2020; Wang & Sugiyama, 2024). P and R are calculated using true positives (TP), false positives (FP), true negatives (TN), and false negatives (FN) in instances of classified lake pixels. Precision (producer's accuracy) indicates the proportion of predicted pixels correctly classified and is calculated as follows:

$$P_{Lake} = \frac{TP}{FP+FN} \tag{4}$$

$$P_{NoLake} = \frac{TN}{TN+FN} \tag{5}$$

Recall (user's accuracy) quantifies the proportion of actual class pixels correctly identified:

$$R_{Lake} = \frac{TP}{TP+FN} \tag{6}$$

$$R_{NoLake} = \frac{TN}{TN+FP} \tag{7}$$

The F1 score, the harmonic mean of precision and recall, is calculated as:

$$F1 = 2 \times \frac{P \times R}{P + R} \tag{8}$$

To assess overall performance, overall accuracy (OA) and Cohen's kappa coefficient (K) were computed. OA is defined as:

$$OA = \frac{TP+TN}{N} \tag{9}$$

K accounts for chance agreement and is calculated using expected accuracy (EA) and OA:

$$EA = \left(\frac{TP+FP}{N} \times \frac{TP+FN}{N}\right) + \left(\frac{FN+TN}{N} \times \frac{FP+TN}{N}\right) \tag{10}$$

$$K = \frac{OA-EA}{1-EA} \tag{11}$$

### 3.5. Results and discussion

Results from the backscatter signature and separability statistics comparisons for cases 1 and 2 are given in sections 3.5.1. to 3.5.4. This is followed by an assessment of classification accuracies using varied feature sets in section 3.5.5 and 3.5.6. and an assessment of feature importance from the Random Forest classifications in Section 3.5.7. Feature importance was evaluated only for the Random Forest model, as XGBoost does not provide a directly comparable metric. Each case corresponds to different stages of the melt season. Case 1 precedes the typical peak in lake area that occurs in early August, whereas case 2 was collected much closer to this historical peak (Hochreuther et al., 2021; Kanzow et al., 2025). ERA5 records (Figure 3.2) show that two-meter air temperatures were higher during the second acquisition (1.5 °C for SAO-2 and 3.6 °C for RCM-2) than during the first (-1.0 °C for SAO-1 and -0.9 °C for RCM-1). Although temperatures at the KPC_U station are generally cooler, they follow the same pattern captured by ERA5. The more advanced melt stage of case 2 acquisition is apparent in the Sentinel-2 image (Figure 3.4), which shows less snow cover and generally larger lake extents than the earlier Landsat-8 scene (Figure 3.3).

#### 3.5.1. Case 1 backscatter signatures and separability

Backscatter signatures and K-S separability statistics for HH, HV, and VV/HH at C- and L-band frequencies are presented in Figure 3.5. For HH, OW consistently exhibits the lowest backscatter across all classes at both frequencies. However, significant overlap between OW and SL at HH leads to poor separability, as indicated by D = 0.31 (C-band) and D = 0.41 (L-band). Generally, HH values across all classes are lower at C-band compared to L-band (e.g., SN is ~ -22 dB at C-band and ~ -9 dB at L-band). Greater variability in L-band backscatter across all classes contributes to generally good separability (D ≥ 0.73) between OW and other classes except for SL (D = 0.41), which contrasts with the moderate to poor (D = 0.31 – 0.64) separability at C-band for all classes except CR (D = 0.91). These differences likely reflect the reduced penetration depth of C-band and dominance of surface scattering, while L-band includes contributions from surface and volume scattering. HH backscatter of LL, overlaps with other classes at both frequencies, resulting in moderate to poor separability. Similar behaviours are observed for HV, with greater overall class signature variability and improved separability at L-band compared to C-band. Notably, at C-band, HV shows poorer overall separability compared to HH, whereas at L-band, HV exhibits increased separability for OW from all classes except for SLs relative to HH. For LL and all ice-sheet facies, L-band HV offers improved separability across all classes. In C-band HH, all classes except for CR exhibit backscatter values close to or below the NESZ (-24 dB), while at L-band, all classes remain well above the NESZ (-34 dB). For C-band HV, backscatter values for all classes frequently approach or fall below the NESZ, whereas at L-band, although HV backscatter values are relatively lower compared to HH, they consistently remain above the NESZ across all classes.

L-band VV/HH demonstrates enhanced separability of both lake classes (OW and LL) from all ice sheet classes, when compared to HV and HH. In contrast, such improvement is not observed at C-band. The L-band VV/HH for OW is the highest of all classes, reaching ~7 dB, while ice sheet class values cluster between ~ -3 and 5 dB. This is consistent with OW exhibiting Bragg scattering characteristics combined with no volume scattering, leading to greater VV than HH (Cloude & Pottier, 1996; Freeman & Durden, 1998). Rougher or volume scattering surfaces like ice and snow tend to yield VV/HH values closer to unity (Freeman & Durden, 1998; Scharien et al., 2012; Scharien et al., 2014). Consequently, OW is highly separable from all other classes using L-band VV/HH, with the lowest D = 0.88 for SL, a substantial improvement over HV and HH. Furthermore, LL exhibits the lowest VV/HH at L-band, characterized by predominantly negative values resulting from HH dominance over VV (Figure 3.5). These results reflect sea ice melt pond retrieval using C-band VV/HH to differentiate pond, bare and snow-covered ice signatures (Scharien et al., 2012; Scharien et al., 2014).

For both C- and L-band HH and HV, SL had consistently poor separability with OW. Of all the ice-sheet facies, SL is the class with the expected highest water content and relative permittivity (Hallikainen et al., 1986) as it represents saturated snow and firn and potentially small, braided stream networks smaller than Sentinel-2 or Landsat 8-pixel width. The high relative permittivity of SL likely causes poor contrast with OW, with both classes attenuating much of the signal and causing predominantly surface scattering due to limit penetration into snow or firn. The greater separability between OW and SL for L-band may be attributable to its enhanced penetration in wet snow and firnto probl, as it can penetrate saturated snow roughly 15 times deeper than C-band (Ulaby et al., 1984; Casey et al., 2016). The enhanced penetration of L-band into the top few cm of the snow or firn media, would lead to greater contributions from volume scattering, thus increasing the backscatter.

L-band VV/HH is the only parameter to demonstrate good separability between OW and SL owing to the preferential scattering of VV relative to HH for specular (Bragg) surfaces (Cloude & Pottier, 1996; Freeman & Durden, 1998). Because the L-band signal can penetrate snow and firn with liquid water content that characterize SL, surface-roughness and volume scattering increase, making the VV and HH backscatter tend to unity and pushing the VV/HH ratio toward 1, unlike the higher values over OW. The lower separability of C-band VV/HH relative to L-band may be attributed to a reduction in VV/HH from wind roughening of OW due to L-bands more limited sensitivity to wind roughening that C-band (Isoguchi & Shimada, 2009). Surface roughening at wind speeds of 6.4 – 8.0 m $s^{-1}$ over sea ice melt pond has been observed to be problematic due to non-Bragg scattering leading to similar VV/HH with non melt water mediums such as ice and snow (Scharien et al., 2014). ERA5 10 m wind speed at the time of acquisition was 5.9 m $s^{-1}$ (Table 3.2). Additionally, in C-band the backscatter from several classes, including both OW and SL, are close to or below the NESZ, potentially limiting separability of the VV/HH.

### 3.5.2. Case 1 lake transects

Figure 3.6 shows C- and L-band HH, HV, and VV/HH sampled over a lake with a lid (i), and another without (ii). Lake (i) provides a clear demonstration of the VV/HH utility relative to HH and HV. Over the OW portion of the lake (~1000 – 1300 m along the transect), HH and HV do not show contrast with the surrounding ice sheet in either frequency. At the start of the LL portion (~1300 m), HH and HV increase in L-band but not in C-band, suggesting volumetric scattering at the longer wavelength. For C-band VV/HH, values remain above 0 dB (ranging from ~ 0 to 4 dB) along the transect, with no clear increase over the OW. In contrast, L-band VV/HH increases to > 0.5 dB over the OW compared to typical background values of -2 to 0.5 dB. Over the LL, L-band VV/HH drops below -2 dB, then returns to background values, delineating the lake structure clearly. Lake (ii), without an ice lid, shows some contrast between lake and surrounding ice in HH and HV, but with no consistent signal. It is evident that dark regions outside the lake are likely to complicate lake boundary detection using single polarization channels. L-band VV/HH again provides strong contrast: outside the lake, values range from -1 to 1 dB, while OW (~800 – 2200 m) VV/HH is above ~ 2dB. C-band VV/HH is noisier, fluctuating between 0 and

4 dB, making lake boundaries likely difficult to identify. We note that C-band HH and HV backscatter fluctuate close to or below their image NESZ values (-24 dB) along segments of the transects, with HH ranging between -19 and -24 dB and HV often falling below the NESZ over both open water and ice-sheet areas. In contrast, L-band HH and HV remain well above their respective NESZ values (-34 dB) throughout all segments of the transects. Overall, the superiority of L-band VV/HH for resolving lake features including OW, LL, and extent, is apparent.

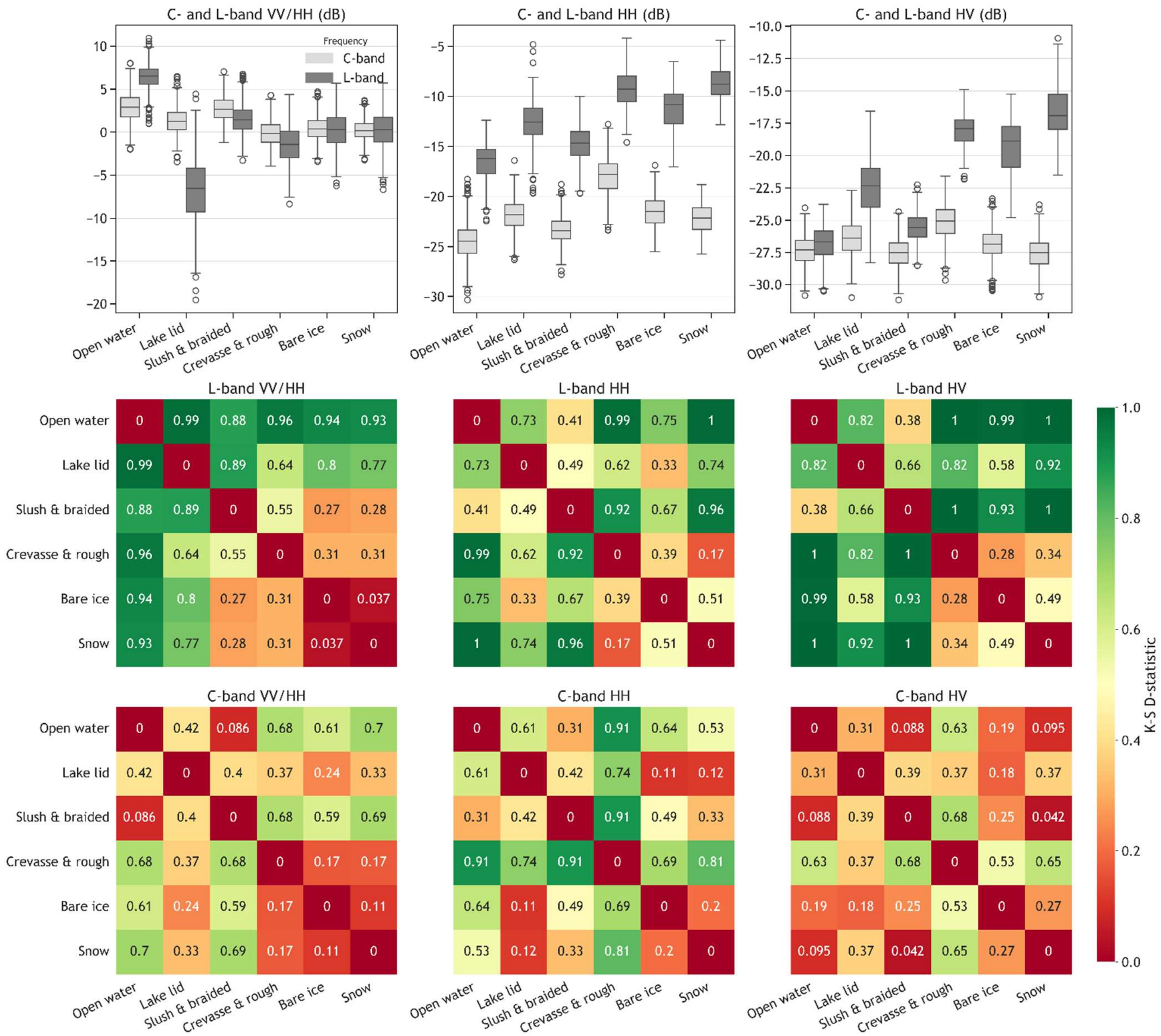


**Figure 3.5.** Backscatter separability for case 1 (12 July 2024 FP image pair). The top row shows box plots of VV/HH, HH, and HV for L-band (grey) and C-band (light) across six surface classes: open water, lake lid, slush and braided, crevasse and rough, bare ice, and snow. The middle row displays the Kolmogorov–Smirnov D statistic for L-band, and the bottom row shows the same for C-band. Higher D values indicate stronger separability between class pairs.

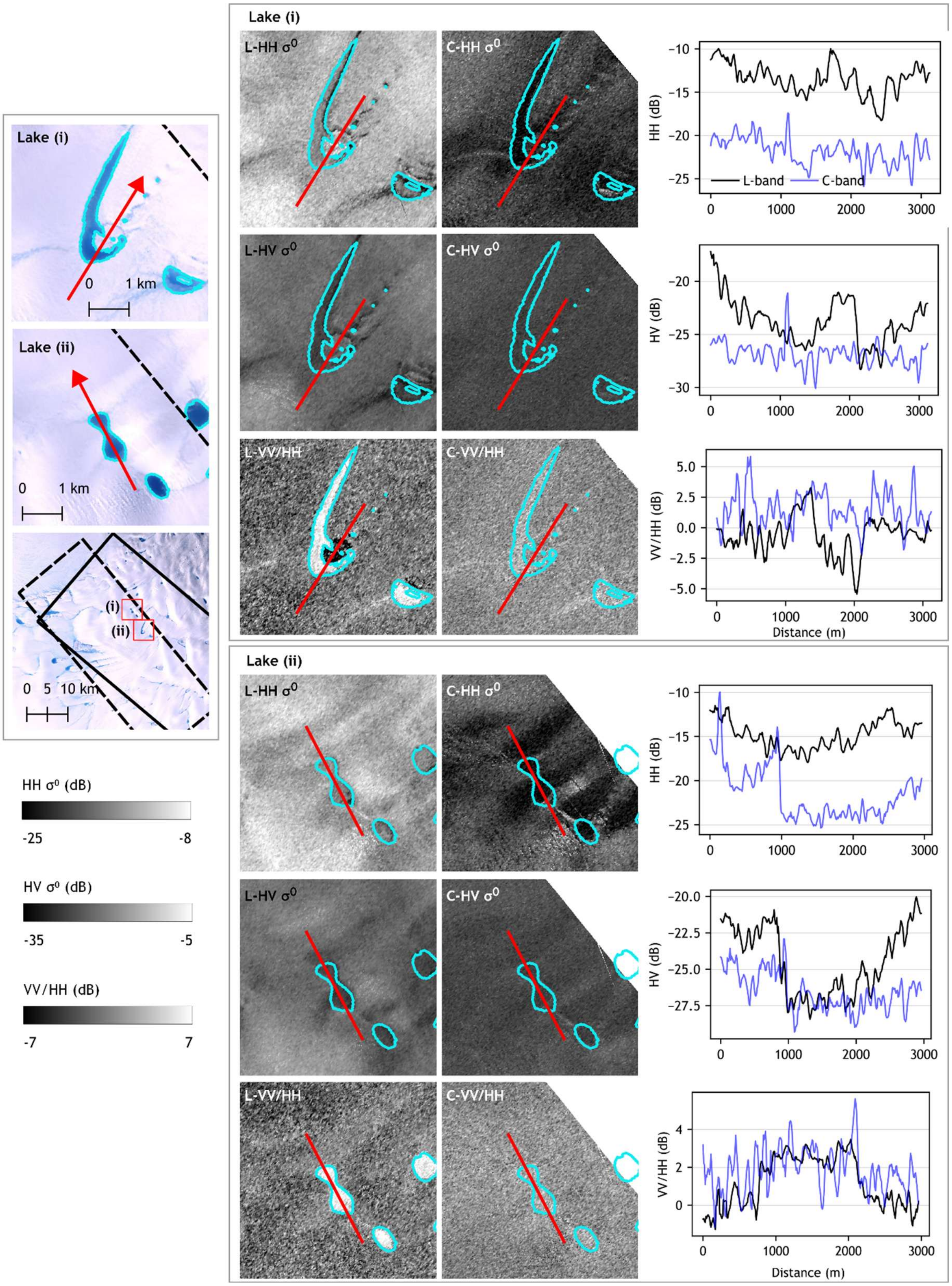


**Figure 3.6.** Transects over two lakes in case 1 (12 July 2024 FP image pair). The left column shows Landsat-8 imagery with lake outlines in cyan, representing extents derived using a high $NDWI_{ice}$ threshold, and transect directions in red. The middle panels display L-band and C-band HH, HV, and VV/HH images with transects and lake outlines overlaid. The right column presents backscatter profiles sampled along each transect, where L-band is shown in black and C-band in blue. Lake (i) contains both open water and a lake lid, while Lake (ii) consists entirely of open water.

### 3.5.3. Case 2 backscatter signatures and separability

For case 2, we first analyze CP data. RCH, LPR, and DoD were evaluated at both C- and L-bands (Figure 3.7), and, for comparison with the fully polarimetric results from case 1, we also analyse HH, HV, and VV/HH extracted from the L-band FP scene (Figure 3.8). RCH shows limited utility: at L-band the OW class is poorly separated from SL and BI ($D \leq 0.25$), and at C-band OW is also poorly distinguished from SN, SL, and LL ($D \leq 0.56$). LL exhibits only poor-to-moderate separability from most ice-sheet facies in either band ($D \sim 0.14 - 0.56$). Absolute RCH values are systematically lower at C-band; the smallest inter-band difference occurs for BI and the largest for SN RCH had generally mixed separation between OW and ice-sheet facies and poor separation between OW and SL in both frequencies. This is consistent with single polarization channels of case 1 and suggests that SL is similarly the most difficult class to separate with single channels of CP data, likely still owing to the high permittivity and reduced penetration in water saturated glacial mediums. We note that C-band RCH backscatter values for OW, LL, SL, and SN classes have significant portions of their distribution at or below the NESZ (-25 dB), while in L-band backscatter values are consistently above its NESZ (-34 dB) for all classes. Consistent with case 2, L-band LPR delivers excellent lake/ice discrimination: every OW–ice sheet comparison yields $D > 0.85$, and the minimum LL–ice sheet D is 0.76. C-band LPR also performs well for OW (all OW–ice $D > 0.78$) but struggles with LL (LL–ice D = 0.15–0.59, except LL–OW = 0.96). In C-band distributions, all non-OW classes cluster between –2 dB and 2 dB, whereas OW peaks near 4 dB; SL overlaps most strongly with OW. At L-band, OW again records the highest LPR, while LL is markedly lower than all classes, indicating dominant horizontal-polarization scattering. DoD mirrors LPR for OW (all OW–ice $D \geq 0.89$) and often yields slightly higher D values, yet LL remains only moderately separable. OW consistently exhibits the lowest DoD, and the L-band spread is narrower than at C-band, producing no overlap between OW and any ice-sheet class.

Considering the FP channels at L-band, HH, HV and VV/HH achieve separability comparable to that of the CP parameters RCH and LPR. For L-band HH, overall separability is limited. OW is well separated from CR and SN ($D > 0.89$) but poorly separated from SL and BI ($D \leq 0.26$). LL shows poor separability from all ice-sheet facies ($D < 0.68$) except bare ice, where moderate separation is reached ($D = 0.85$). L-band HV also has a mixed separability of OW and LL with ice-sheet facies. Separability of OW and LL from SL and BI is moderate ($D \sim 0.4 – 0.65$) and from CR and SN is good ($D \sim 0.78 – 1$). Similar to case 1, all L-band HH and HV backscatter values are above the NESZ (-34 dB).

In contrast, L-band VV/HH provides good separability for OW relative to every ice-sheet class (all OW-ice D ≥ 0.84) and for LL relative to ice-sheet classes (all LL-ice D ≥ 0.77), a performance consistent with that of L-band LPR. Of all the SAR parameters analyzed at both frequencies in both cases, L-band VV/HH demonstrated the most consistent separability between OW and all ice-sheet facies. In separating OW from ice-sheet facies, L-band VV/HH consistently exhibited good contrast between OW and surrounding ice-sheet classes, including SL, which likely has the highest permittivity among the ice-sheet facies. In contrast, C-band VV/HH (case 1) and LPR (case 2) displayed less consistency in distinguishing these classes, potentially due to the limited penetration capability of C-band into ice-sheet facies undergoing varying degrees of melt. When assessing LL–ice separability, neither C-band VV/HH nor LPR demonstrated effective discrimination, whereas L-band VV/HH (along with L-band LPR) provided clear separation, similar to in case 1. These results suggest that only the longer wavelength L-band SAR penetrates sufficiently deep to interact with horizontal layering within LL, thus producing preferential scattering of horizontally polarized waves relative to vertically polarized waves.

### 3.5.4. Case 2 lake transects

CP parameter profiles were sampled across two lakes: Lake i (OW followed by an ice lid, LL) and Lake ii (OW only) (Figure 3.9). RCH fails to highlight either OW (~1400 m along-track) or LL, remaining within ±1 dB of surrounding ice in both bands. In contrast, LPR spikes sharply over OW to ~3 dB (L-band) and ~4 dB (C-band). Down-stream, C-band LPR decays gradually across the lid, whereas L-band LPR drops to below –2 dB, cleanly delineating the LL before rebounding to ~0 dB at ~3400 m, the inferred lid terminus. DoD drops at the OW boundary for both bands; over the LL C-band DoD is flat, while L-band DoD shows a slight rise, again signalling lid presence. Lake ii (OW only), RCH remains flat over the OW (~1500–2800 m), whereas LPR rises rapidly to ~4 dB (C-band) and ~3 dB (L-band) and falls back to ice-sheet levels at the down-lake edge. DoD exhibits a decrease and increases pattern, marking both OW margins in each band. Similar to case 1, single-polarization channel RCH at C-band exhibits backscatter values close to the NESZ (-25 dB) along significant portions of the transect. In contrast, L-band RCH backscatter values remain significantly higher than the corresponding NESZ of -34 dB. Together, these observations confirm that L-band CP metrics, especially LPR, provide the most reliable single-parameter discrimination of lake surfaces and lids, while C-band LPR remains effective for OW but is less sensitive to LL. RCH contributes little additional information beyond the superior LPR and DoD metrics.

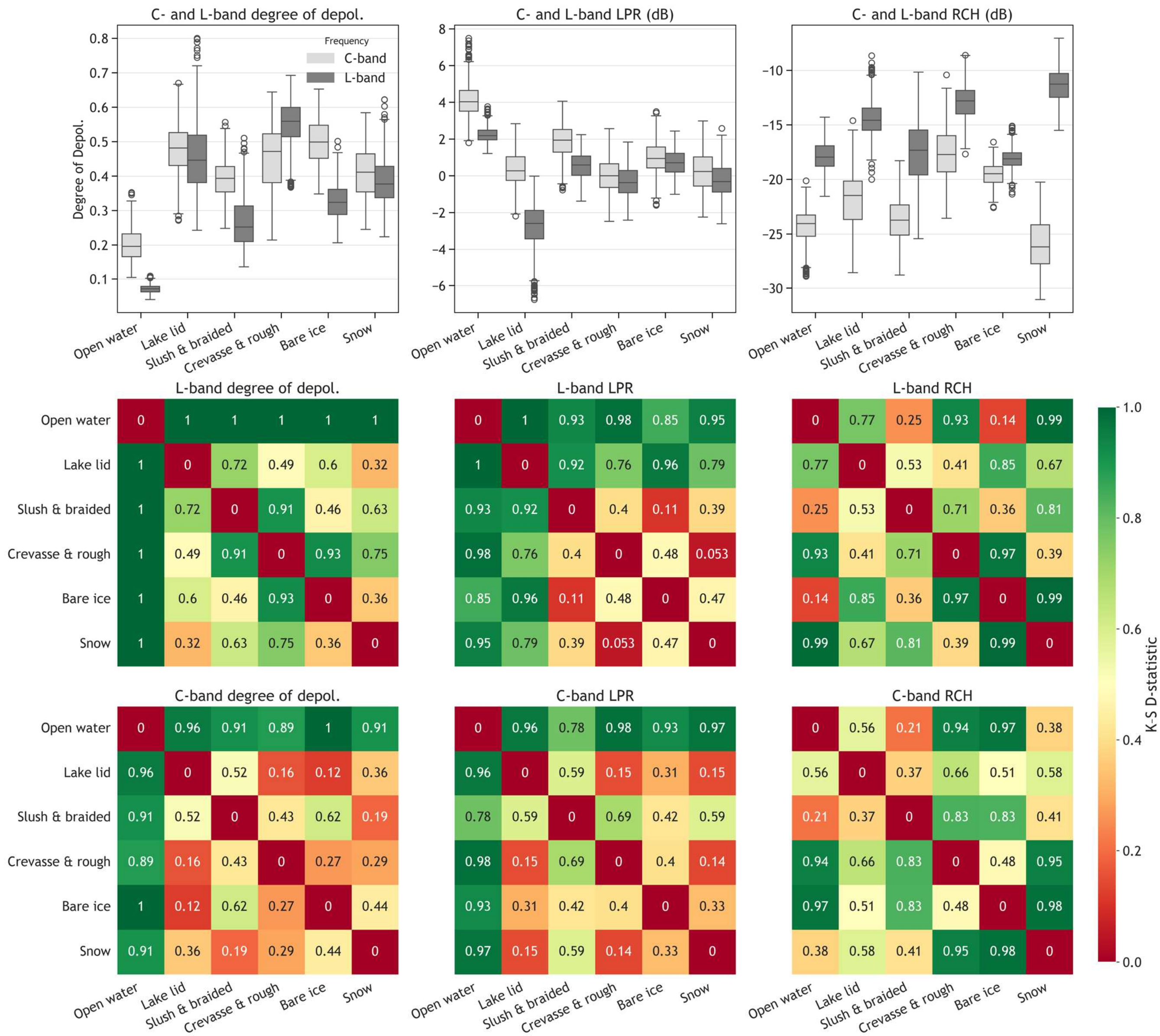


**Figure 3.7.** Backscatter separability for case 2 (20/21 July 2024 CP image pair). The top row presents box plots of the DoD, LPR, and RCH for L-band (grey) and C-band (light grey) across six surface classes: open water, lake lid, slush and braided, crevasse and rough, bare ice, and snow. The middle row displays the Kolmogorov–Smirnov D statistic for L-band, and the bottom row shows the same for C-band. Higher D values indicate stronger separability between class pairs.

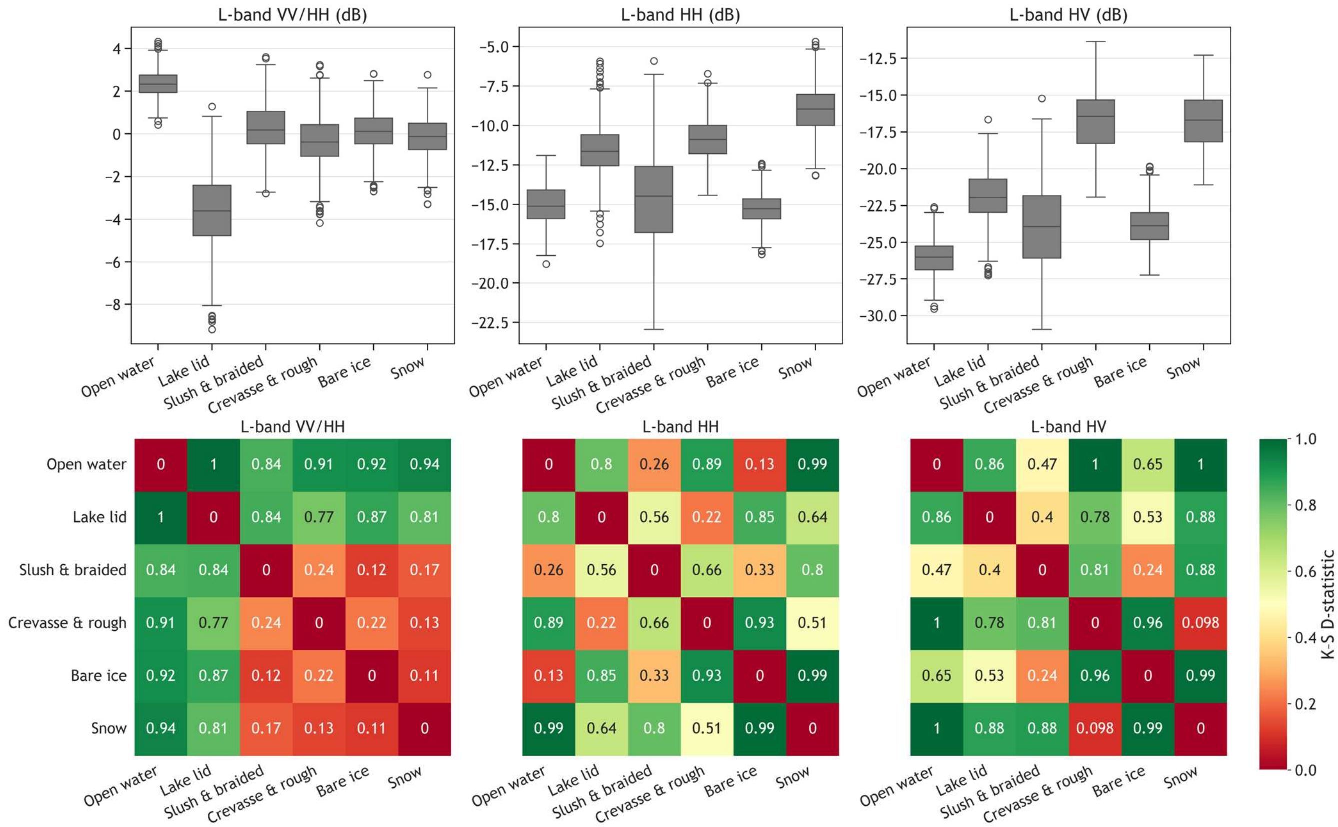


**Figure 3.8.** Backscatter separability for L-band FP image used to simulate the CP image of case 2 (Figure 3.7). The top row shows box plots of VV/HH, HH, and HV for L-band across six surface classes: open water, lake lid, slush and braided, crevasse and rough, bare ice, and snow. The bottom row displays the Kolmogorov–Smirnov D statistic. Higher D values indicate stronger separability between class pairs.

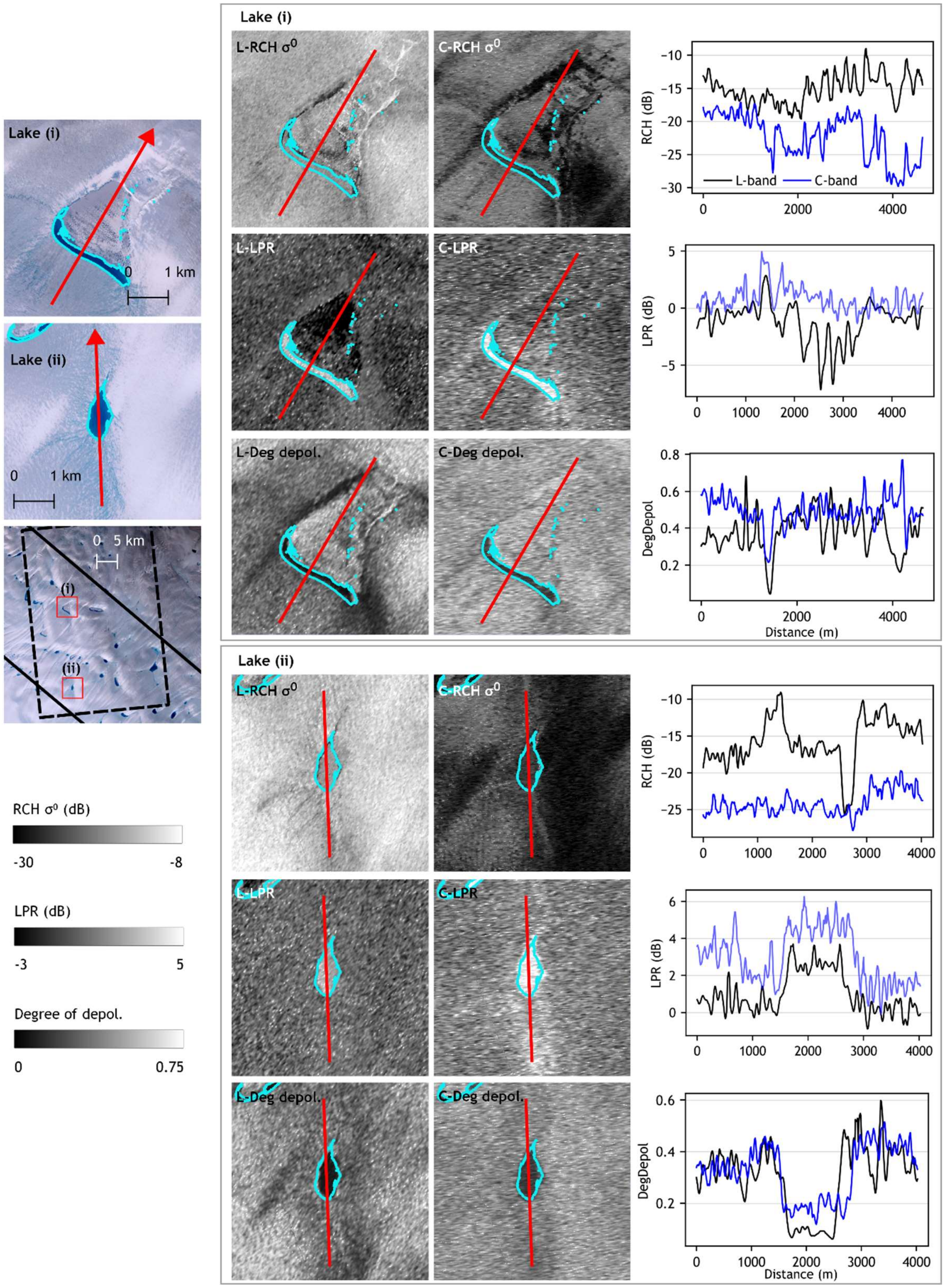


**Figure 3.9.** Transects over two lakes in case 2 (20/2021 July 2024 CP image pair). The left column shows Landsat-8 imagery with lake extents in cyan derived from a high $NDWI_{ice}$ threshold and transect directions in red. The center panels display L-band and C-band RCH, LPR, and DoD with transects overlaid. The right column presents profiles along each transect with L-band in black and C-band in blue. Lake (i) contains both open water and a lake lid whereas Lake (ii) is entirely open water.

### 3.5.5. Case 1 lake classification accuracy

Classification metrics for cases 1 and 2 are summarized in Tables 3.3 and 3.4, with example classification outputs provided in Figure 3.10 and 3.11. Because cases 1 and 2 differ in acquisition date, melt stages, and (for C-band) footprint and hence training data, we treat their results separately.

First, we consider case 1 and feature set a) to d) usings varying combinations of HH, HV, and VV/HH (Table 3.4). Across all the L-band feature sets, and using both classification algorithms, OA and F1 exceed those of any C-band model. The best C-band configuration was feature set d) in XGBoost, achieving OA = 0.835, whereas the lowest-performing L-band feature group (set b) still attains OA = 0.880. Feature sets including VV/HH (set c and d) yield the highest OA and K. Notably, the OA-K gap is far larger in C-band (~ 0.17 - 0.34) than in L-band (~ 0.01 - 0.12), indicating that chance agreement inflates OA more strongly at the shorter wavelength. Adding GLCM textures improves most C-band and L-band models, except for the L-band set a), which exhibits a decrease in accuracy relative to set b). P tends to exceed R for the lake class in C-band models, whereas recall dominates for no-lake; these biases are muted in L-band.

Next, we consider case 1 feature sets e) to h), which are based on VV and HH polarizations (Table 3.4). Similar to results from feature sets a) to d), L-band feature sets using both classification algorithms achieved higher OA and F1 scores than all corresponding C-band models. Furthermore, within both C- and L-band, feature sets e) to h) produced metrics comparable to those from sets a) to d), indicating that dual-pol feature sets (VV + HH) can achieve similar or better classification performance to FP sets that include HV. The inclusion of texture parameters in the L-band dual-pol feature set f) led to a reduction in accuracy, whereas adding texture parameters to the L-band dual-pol set that included VV/HH (set h) resulted in increased accuracy for both Random Forest and XGBoost. For C-band, including texture parameters improved accuracy consistently in both dual-pol (set f) and VV/HH dual-pol (set h) configurations. Overall, among all feature sets (a–h), the highest F1, OA, and K were obtained with L-band feature set h using the Random Forest classifier.

Figure 3.10 confirms the similar performance of XGBoost and Random Forest, mapped lake extents are similar for each frequency and feature set. C-band models misclassify large portions of the surrounding ice sheet as lake, whereas L-band models show much less confusion (Figure 3.10). The best L-band configurations (Figure 3.10$a_{vi}$ and $b_{vi}$) closely track the $NDWI_{ice}$ lake outlines, with minimal misclassification of adjacent snow and ice. Minimal difference are apparent between L-band classifications based solely on the co-polarized bands VV and HH (Figure 3.10$a_{vi}$ and 10$b_{vi}$) and those that included HV (Figure 3.10$a_v$ and $b_v$).

### 3.5.6. Case 2 lake classification accuracy

Next, we consider case 2 CP feature sets (i to l) (Table 3.5). The best C-band result is obtained with set h) in Random Forest (OA = 0.989, K = 0.978), while the best L-band result comes from set g) in XGBoost (OA = 0.986, K = 0.972. For set i), L-band achieves higher OA and K for both classification models than C-band, whereas for set j), which includes texture parameters, C-band produces higher OA and K. Similarly, for feature sets that incorporate LPR and DoD (sets k and l), L-band yields higher OA and K in set k), while C-band yields higher values in set l). Thus, incorporating texture parameters brings small gains in C-band but neutral or negative changes in L-band. For sets i) and j), the OA–K gaps for C-band (~0.054 – 0.132) and L-band (~0.103 – 0.145) are similarly large. However, upon introduction of LPR and DoD (sets k and l), these gaps decrease substantially (0.011 – 0.052 for C-band; 0.004 – 0.011 for L-band). Feature sets containing LPR and DoD yield the largest absolute accuracy gains at both wavelengths.

L-band feature sets that included FP data, specifically variations of HH, HV, and VV/HH (sets m to p), as well as variations of VV, HH, and VV/HH (sets q to t), produced results comparable to CP feature sets. The highest OA and K among all feature sets in case 2 were achieved by sets p (OA = 0.999, K = 0.998) and t (OA = 0.999, K = 0.998) using Random Forest. Similar to case 1, feature sets relying solely on dual-pol VV + HH data (sets q to t) exhibited high accuracy, comparable or superior to those incorporating HV (sets m to p), and surpassed the accuracy obtained by CP feature sets. L-band feature sets based on dual-pol HH + HV data (sets m and n) achieved lower OA (0.838 – 0.877) and K (0.676 – 0.754) than dual-pol VV + HH (sets q and r) (OA = 0.933 – 0.948 and K = 0.866 – 0.896). The inclusion of VV/HH in sets s) and t) further increased OA and K relative to feature sets q) and r).

In Figure 3.11, similarities in performance between XGBoost and RF models are evident. C- and L-band feature sets without LPR or DoD (Figure 3.11$a_i$, $a_{iii}$, $b_i$, and $b_{iii}$) had greater misclassification of snow and ice, as well as less homogenous areas of correctly classified areas over lake extents. Both C- and L-band models with features sets including LPR and DoD exhibited very accurate classification of lakes, with minimal misclassification of snow and ice areas, and most of the lake correctly classified. L-band feature sets that rely solely on VV and HH bands (Figure 3.11$a_v$ and $b_v$) classify lakes accurately and show minimal confusion with surround ice-sheet facies, comparable to C- and L-band CP feature sets that incorporate LPR and DoD (Figure 3.11$a_{ii}$, $a_{iv}$, $b_{ii}$, and $b_{iv}$).

**Table 3.4.** Classification metrics for case 1 (12 July 2024 FP image pair), comparing C-band RCM and L-band SAOCOM-1. Random Forest and XGBoost models were trained with eight C- and L-band feature sets each: a) HH + HV, b) HH + HV + GLCMs; c) HH + HV + VV/HH; d) HH + HV + VV/HH + GLCMs; e) VV + HH; f) VV + HH + GLCMs; g) VV + HH + VV/HH; h) VV, HH, VV/HH, GLCMs. Reported metrics are precision and recall for the lake and no-lake classes ($P_{Lake}$, $R_{Lake}$, $P_{NoLake}$, $R_{NoLake}$), macro-averaged F1, overall accuracy (OA), and Cohen's K.

| Band | Feature Set | $P_{Lake}$ | $R_{Lake}$ | $P_{NoLake}$ | $R_{NoLake}$ | F1 | OA | K |
|---|---|---|---|---|---|---|---|---|
| | | | | **Random Forest** | | | | |
| **C-band** | a) HH, HV | 0.727 | 0.526 | 0.629 | 0.802 | 0.657 | 0.664 | 0.328 |
| | b) HH, HV, GLCMs | 0.833 | 0.638 | 0.707 | 0.872 | 0.752 | 0.755 | 0.51 |
| | c) HH, HV, VV/HH | 0.775 | 0.722 | 0.74 | 0.79 | 0.756 | 0.756 | 0.512 |
| | d) HH, HV, VV/HH, GLCMs | 0.783 | 0.908 | 0.89 | 0.748 | 0.827 | 0.828 | 0.656 |
| | e) VV, HH | 0.785 | 0.75 | 0.761 | 0.794 | 0.772 | 0.772 | 0.544 |
| | f) VV, HH, GLCMs | 0.886 | 0.796 | 0.815 | 0.898 | 0.847 | 0.847 | 0.694 |
| | g) VV, HH, VV/HH | 0.776 | 0.742 | 0.753 | 0.786 | 0.764 | 0.764 | 0.528 |
| | h) VV, HH, VV/HH, GLCMs | 0.784 | 0.914 | 0.897 | 0.748 | 0.83 | 0.831 | 0.662 |
| **L-band** | a) HH, HV | 0.922 | 0.92 | 0.92 | 0.922 | 0.921 | 0.921 | 0.842 |
| | b) HH, HV, GLCMs | 0.931 | 0.836 | 0.851 | 0.938 | 0.887 | 0.887 | 0.774 |
| | c) HH, HV, VV/HH | 0.957 | 0.982 | 0.982 | 0.956 | 0.969 | 0.969 | 0.938 |
| | d) HH, HV, VV/HH, GLCMs | 0.990 | 0.996 | 0.996 | 0.99 | 0.993 | 0.993 | 0.986 |
| | e) VV, HH | 0.953 | 0.942 | 0.943 | 0.954 | 0.948 | 0.948 | 0.896 |
| | f) VV, HH, GLCMs | 0.931 | 0.838 | 0.853 | 0.938 | 0.888 | 0.888 | 0.776 |
| | g) VV, HH, VV/HH | 0.954 | 0.946 | 0.946 | 0.954 | 0.95 | 0.95 | 0.9 |
| | h) VV, HH, VV/HH, GLCMs | 0.994 | 0.996 | 0.996 | 0.994 | 0.995 | 0.995 | 0.99 |
| | | | | **XGBoost** | | | | |
| **C-band** | a) HH, HV | 0.855 | 0.52 | 0.655 | 0.912 | 0.705 | 0.716 | 0.432 |
| | b) HH, HV, GLCMs | 0.794 | 0.638 | 0.697 | 0.834 | 0.733 | 0.736 | 0.472 |
| | c) HH, HV, VV/HH | 0.799 | 0.738 | 0.757 | 0.814 | 0.776 | 0.776 | 0.552 |
| | d) HH, HV, VV/HH, GLCMs | 0.793 | 0.906 | 0.89 | 0.764 | 0.834 | 0.835 | 0.67 |
| | e) VV, HH | 0.816 | 0.684 | 0.728 | 0.846 | 0.763 | 0.765 | 0.53 |
| | f) VV, HH, GLCMs | 0.881 | 0.872 | 0.873 | 0.882 | 0.877 | 0.877 | 0.754 |
| | g) VV, HH, VV/HH | 0.807 | 0.746 | 0.764 | 0.822 | 0.784 | 0.784 | 0.568 |
| | h) VV, HH, VV/HH, GLCMs | 0.78 | 0.93 | 0.913 | 0.738 | 0.832 | 0.834 | 0.668 |
| **L-band** | a) HH, HV | 0.923 | 0.932 | 0.931 | 0.922 | 0.927 | 0.927 | 0.854 |
| | b) HH, HV, GLCMs | 0.936 | 0.816 | 0.837 | 0.944 | 0.88 | 0.88 | 0.76 |
| | c) HH, HV, VV/HH | 0.96 | 0.972 | 0.972 | 0.96 | 0.966 | 0.966 | 0.932 |
| | d) HH, HV, VV/HH, GLCMs | 0.99 | 0.996 | 0.996 | 0.99 | 0.993 | 0.993 | 0.986 |
| | e) VV, HH | 0.949 | 0.938 | 0.939 | 0.95 | 0.944 | 0.944 | 0.888 |
| | f) VV, HH, GLCMs | 0.928 | 0.83 | 0.846 | 0.936 | 0.883 | 0.883 | 0.766 |
| | g) VV, HH, VV/HH | 0.95 | 0.948 | 0.948 | 0.95 | 0.949 | 0.949 | 0.898 |
| | h) VV, HH, VV/HH, GLCMs | 0.992 | 0.996 | 0.996 | 0.992 | 0.994 | 0.994 | 0.988 |

**Table 3.5.** Classification metrics for case 2 (20/21 July 2024 CP images, and L-band FP), comparing C-band RCM and L-band SAOCOM-1. Random Forest and XGBoost models are evaluated with four C- and L-band CP feature sets: i) RCH + RCV; j) RCH + RCV + GLCMs; k) RCH + RCV + LPR/DoD, and l) RCH + RCV + LPR/DoD + GLCMs. Eight L-band FP feature sets were also evaluated: m) HH + HV, n) HH + HV + GLCMs; o) HH + HV + VV/HH; p) HH + HV + VV/HH + GLCMs; q) VV + HH; r) VV + HH + GLCMs; s) VV + HH + VV/HH; t) VV, HH, VV/HH, GLCMs. Metrics reported are precision and recall for lake and no-lake classes ($P_{Lake}$, $R_{Lake}$, $P_{NoLake}$, $R_{NoLake}$), macro-averaged F1, overall accuracy (OA), and Cohen's K.

| Band | Feature Set | $P_{Lake}$ | $R_{Lake}$ | $P_{NoLake}$ | $R_{NoLake}$ | F1 | OA | K |
|---|---|---|---|---|---|---|---|---|
| | | | | **Random Forest** | | | | |
| **C-band** | i) RCH, RCV | 0.923 | 0.836 | 0.85 | 0.93 | 0.883 | 0.883 | 0.766 |
| | j) RCH, RCV, GLCMs | 0.92 | 0.946 | 0.944 | 0.918 | 0.932 | 0.932 | 0.864 |
| | k) RCH, RCV, LPR/DoD | 0.987 | 0.926 | 0.93 | 0.988 | 0.957 | 0.957 | 0.914 |
| | l) RCH, RCV, LPR/DoD, GLCMs | 0.994 | 0.984 | 0.984 | 0.994 | 0.989 | 0.989 | 0.978 |
| **L-band** | i) RCH, RCV | 0.913 | 0.878 | 0.882 | 0.916 | 0.897 | 0.897 | 0.794 |
| | j) RCH, RCV, GLCMs | 0.885 | 0.816 | 0.829 | 0.894 | 0.855 | 0.855 | 0.71 |
| | k) RCH, RCV, LPR/DoD | 0.994 | 1.0 | 1.0 | 0.994 | 0.997 | 0.997 | 0.994 |
| | l) RCH, RCV, LPR/DoD, GLCMs | 0.967 | 1.0 | 1.0 | 0.966 | 0.983 | 0.983 | 0.966 |
| | m) HH, HV | 0.885 | 0.866 | 0.869 | 0.888 | 0.877 | 0.877 | 0.754 |
| | n) HH, HV, GLCMs | 0.853 | 0.824 | 0.83 | 0.858 | 0.841 | 0.841 | 0.682 |
| | o) HH, HV, VV/HH | 0.99 | 0.96 | 0.961 | 0.99 | 0.975 | 0.975 | 0.95 |
| | p) HH, HV, VV/HH, GLCMs | 0.998 | 1.0 | 1.0 | 0.998 | 0.999 | 0.999 | 0.998 |
| | q) VV, HH | 0.955 | 0.94 | 0.941 | 0.956 | 0.948 | 0.948 | 0.896 |
| | r) VV, HH, GLCMs | 0.945 | 0.92 | 0.922 | 0.946 | 0.933 | 0.933 | 0.866 |
| | s) VV, HH, VV/HH | 0.948 | 0.948 | 0.948 | 0.948 | 0.948 | 0.948 | 0.896 |
| | t) VV, HH, VV/HH, GLCMs | 0.998 | 1.0 | 1.0 | 0.998 | 0.999 | 0.999 | 0.998 |
| | | | | XGBoost | | | | |
| **C-band** | i) RCH, RCV | 0.874 | 0.86 | 0.862 | 0.876 | 0.868 | 0.868 | 0.736 |
| | j) RCH, RCV, GLCMs | 0.939 | 0.954 | 0.953 | 0.938 | 0.946 | 0.946 | 0.892 |
| | k) RCH, RCV, LPR/DoD | 0.989 | 0.906 | 0.913 | 0.99 | 0.948 | 0.948 | 0.896 |
| | l) RCH, RCV, LPR/DoD, GLCMs | 0.99 | 0.986 | 0.986 | 0.99 | 0.988 | 0.988 | 0.976 |
| **L-band** | i) RCH, RCV | 0.895 | 0.87 | 0.874 | 0.898 | 0.884 | 0.884 | 0.768 |
| | j) RCH, RCV, GLCMs | 0.928 | 0.824 | 0.842 | 0.936 | 0.88 | 0.88 | 0.76 |
| | k) RCH, RCV, LPR/DoD | 0.994 | 0.998 | 0.998 | 0.994 | 0.996 | 0.996 | 0.992 |
| | l) RCH, RCV, LPR/DoD, GLCMs | 0.973 | 1.0 | 1.0 | 0.972 | 0.986 | 0.986 | 0.972 |
| | m) HH, HV | 0.876 | 0.872 | 0.873 | 0.876 | 0.874 | 0.874 | 0.748 |
| | n) HH, HV, GLCMs | 0.855 | 0.814 | 0.823 | 0.862 | 0.838 | 0.838 | 0.676 |
| | o) HH, HV, VV/HH | 0.992 | 0.958 | 0.959 | 0.992 | 0.975 | 0.975 | 0.95 |
| | p) HH, HV, VV/HH, GLCMs | 0.998 | 0.982 | 0.982 | 0.998 | 0.99 | 0.99 | 0.98 |
| | q) VV, HH | 0.946 | 0.944 | 0.944 | 0.946 | 0.945 | 0.945 | 0.89 |
| | r) VV, HH, GLCMs | 0.953 | 0.942 | 0.943 | 0.954 | 0.948 | 0.948 | 0.896 |
| | s) VV, HH, VV/HH | 0.957 | 0.944 | 0.945 | 0.958 | 0.951 | 0.951 | 0.902 |
| | t) VV, HH, VV/HH, GLCMs | 0.998 | 0.982 | 0.982 | 0.998 | 0.99 | 0.99 | 0.98 |

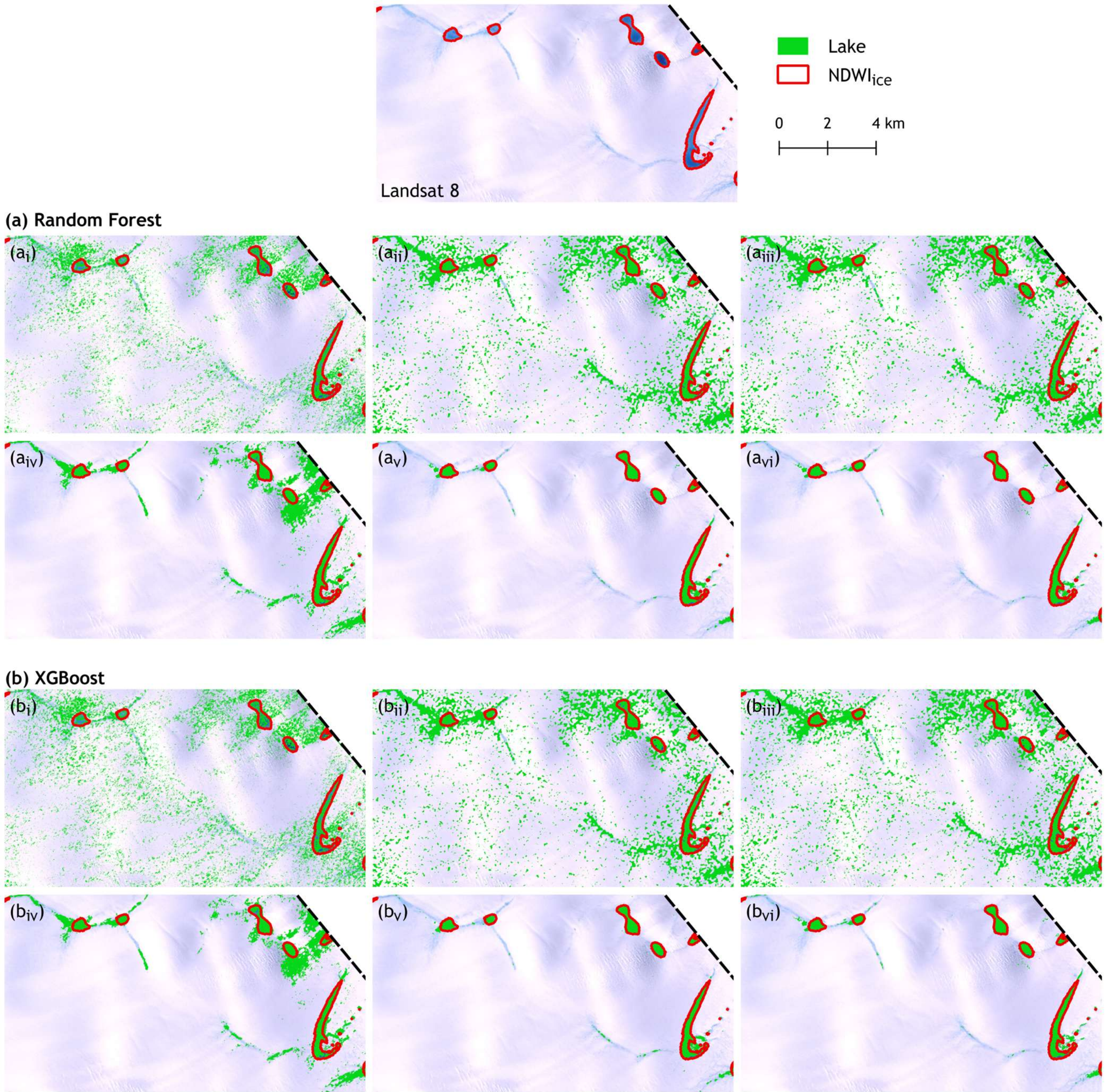


**Figure 3.10.** Example lake classification outputs from case 1 (12 July 2024 FP image pair). The top panel shows a reference Landsat-8 RGB mosaic (13 July) with the RCM footprint outlined by a dashed line. Panels (a) and (b) present classifications from Random Forest and XGBoost, respectively. In each row, panels (i) to (iii) correspond to C-band feature sets b), d), and h), while panels (iv) to (vi) correspond to L-band. Green pixels indicate areas classified as lake and the red outlines denote lake detected using $NDWI_{ice}$ (> 0.30).

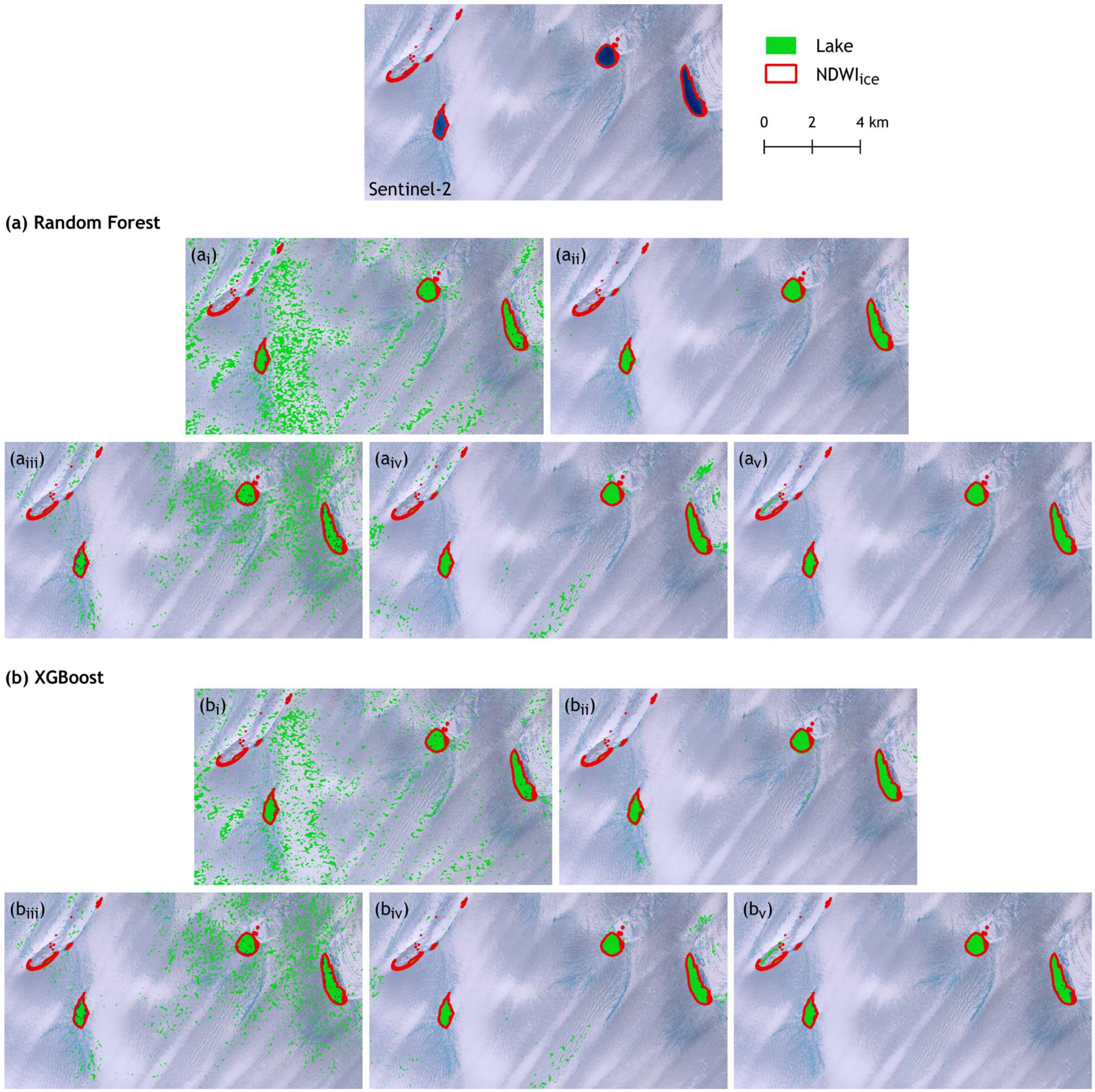


**Figure 3.11.** Example lake classification outputs from case 2 (20/21 July 2024 CP image pair). The top panel shows a reference Sentinel-2 RGB mosaic (20 July). Panels (a) and (b) show classifications from Random Forest and XGBoost, respectively. In each row, panels (i) and (ii) correspond to C-band feature sets j) and l), while panels (iii) to (v) correspond to L-band feature sets j), l), and p). Green pixels indicate areas classified as lake and the red outlines denote lake detected using $NDWI_{ice}$ (> 0.25).

### 3.5.7. Lake classification feature importance

Feature importance, quantified via the Random Forest mean decrease in Gini impurity for case 1 (feature set d, Table 3.4) and case 2 (feature sets l and p, Table 3.5) are shown in Figure 3.12 and Figure 3.13 respectively.

Considering first case 1, in both frequencies the most influential predictors are GLCM texture parameters derived from VV/HH; VV/HH image ranks next for C-band whereas for L-band, HV is the single most important non-texture variable (19 % of total) (Figure 3.12). At L-band, the four leading VV/HH textures together contribute 48.6 %.

For case 2, DoD, and GLCM texture parameters derived from it, dominate (Figure 3.13). When considering feature set l) (Table 3.5) the top seven variables account for 66 % of total importance in C-band and 84 % in L-band, suggesting that L-band classification can be driven by a smaller subset of predictors and is thus more efficient. C-band next favours GLCM texture parameters derived from RCH (correlation, dissimilarity, contrast), whereas at L-band the LPR is important, reinforcing the added value of CP ratios. In the L-band FP feature set for case 2 (set p, Table 3.5), VV/HH and its associated GLCM texture parameters together account for 93 % of the total feature importance, underscoring VV/HH as a key predictor of lakes during the melt season.

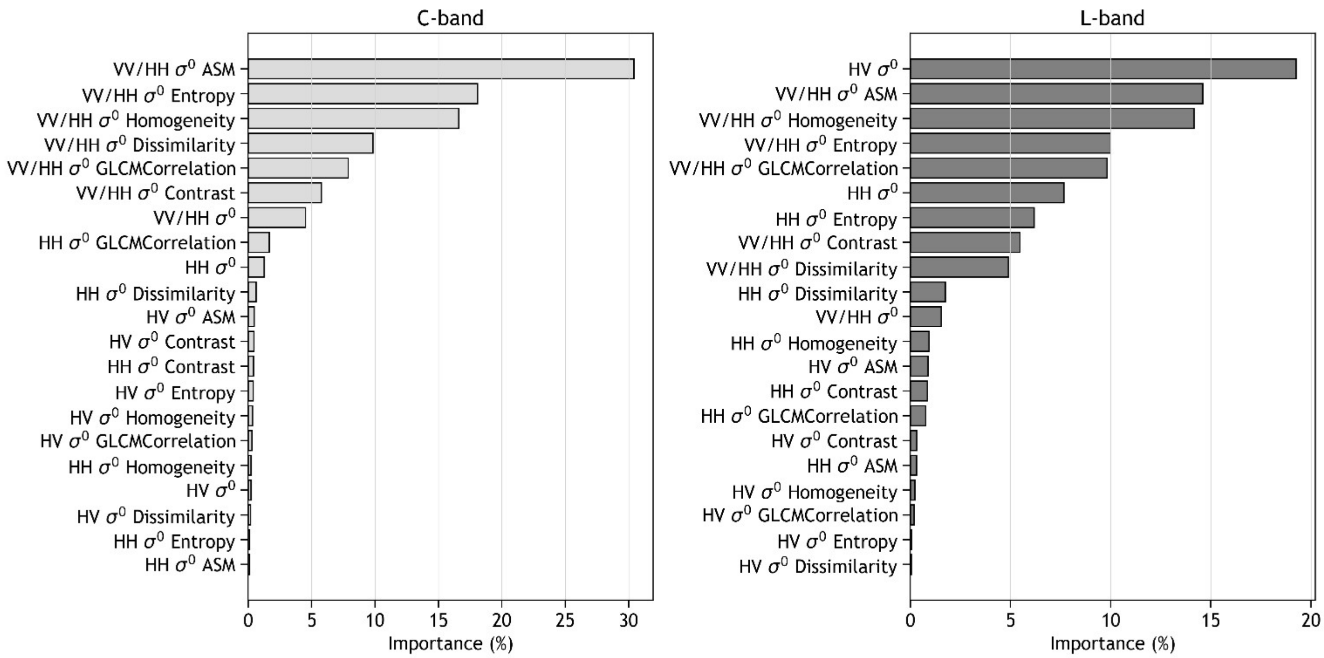


**Figure 3.12.** Feature importance for case 1 (12 July 2024 FP image pair), plotted as the percentage contribution to the total mean decrease in Gini impurity from the Random Forest classifier. C- and L-band feature sets d) (Table 3.4) are shown on the left and right respectively.

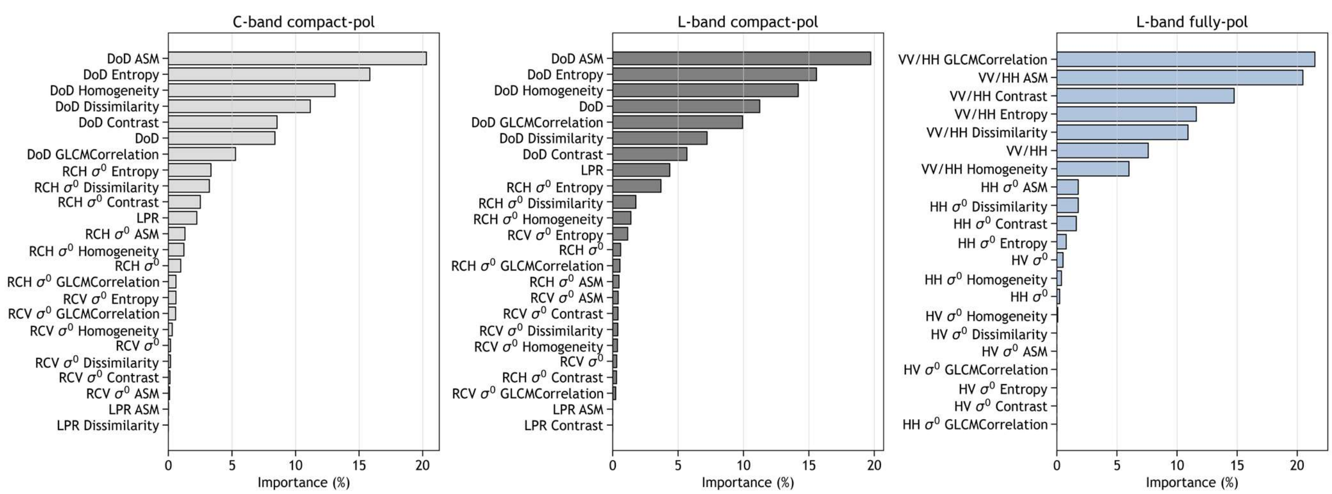


**Figure 3.13.** Feature importance for case 2 (20/21 July 2024 CP image pair and L-band FP image), plotted as the percentage contribution to the total mean decrease in Gini impurity from the Random Forest classifier. C-band and L-band feature sets l) (Table 3.5) are shown on the left and center plots respectively. L-band feature set p) (Table 3.5) is shown on the right plot.

### 3.8. Conclusion

In this study we analyzed two coincident pairs of C- and L-band data during the 2024 melt season over ZI and 79NG in NE Greenland. Our analysis included a detailed comparison of backscatter signatures and separability for lake classes (OW and LL) and ice-sheet facies (SL, SN, CR, and BI). This analysis was complimented by backscatter values sampled along two lakes for each case. This was followed by classifications of lakes using two decision tree machine learning models (XGBoost and Random Forest).

Our first objective was to determine the optimal frequency and polarizations for separation of open water and ice-covered supraglacial lakes from surrounding ice sheet facies during melt conditions. We found that VV/HH and LPR exhibited strong separability of OW from all ice-sheet facies in both frequencies and cases, except for the first C-band in case 1. For case 1 C-band VV/HH, poor separability may be attributable to wind-induced surface roughening of OW and backscatter values near or at the NESZ. The enhanced penetration of L-band relative to C-band likely contributed to superior performance in separating OW from SL with VV/HH and single-pol bands. Furthermore, L-band VV/HH and LPR demonstrated a low ratio for LL relative to OW and other ice-sheet facies. CP DoD in case 2 showed good separation of OW from ice-sheet facies at both frequencies, but did not achieve the strong LL–ice separation observed with L-band VV/HH and LPR. In general, single-polarization channels (HH, HV, and RCH) provided less consistent separation of OW from ice-sheet facies and were particularly limited in distinguishing LL. Among all classes, SL consistently showed the poorest separability, likely due to its low dielectric contrast with OW.

The second objective of our study was to evaluate Random Forest and XGBoost classifiers for mapping lakes and to identify which parameters were most effective for this purpose. Classification results indicated that XGBoost and Random Forest achieved similar accuracies across all evaluated feature sets, with neither algorithm consistently outperforming the other. For case 1, all L-band feature sets achieved higher classification accuracies than their corresponding C-band counterparts, whereas results from case 2 were more comparable between frequencies. The inclusion of texture parameters typically improved classification accuracy in both cases. Feature sets that included VV/HH or LPR resulted in greater classification accuracies, reflecting the greater overall separability these parameters provide between OW and ice-sheet facies. Dual-pol VV + HH based feature sets were capable of achieving accuracies similar or greater than those that included HV, supporting the notion of the importance VV/HH. Results on feature importance demonstrated that VV/HH was one of the most influential parameters in both case 1 and 2 FP classifications.

Future research can build upon this work by integrating in-situ data to directly measure liquid water content in snow and firn and to characterize the horizontal structure and internal properties of lake lids. Such data would enable detailed analyses of scattering mechanisms and provide critical geophysical context to remote sensing interpretations. Additionally, in-situ wind speed measurements could help clarify the impacts of wind-induced roughening on lake surface backscatter. Future comparative studies of SAR frequencies and polarizations should aim to acquire imagery at consistent incidence angles to minimize variability caused by sensor geometry and thus simplify interpretation. Evaluating lake detection performance explicitly at different incidence angles (near, mid, and far) could become a primary component of future research. Although fully-polarimetric, compact polarimetric, and dual-polarimetric (VV + HH) data remain limited at both C- and L-band, researchers may utilize taskable sensors such as SAOCOM-1 and ALOS PALSAR-2, which offer user-defined polarization modes. This capability could be especially valuable for continuous monitoring of field sites with instrumentation that require uninterrupted observations, such as lakes and melt ponds on ice shelves. Furthermore, future SAR missions should consider regularly acquiring dual polarimetric VV + HH or compact polarimetric data, as compact polarimetry provides a richness of information comparable to fully polarimetric data but with greater energy efficiency.

Lakes represent an important meltwater component of the GrIS's hydrologic systems, influencing both surface mass balance and ice-sheet dynamics. While optical-based methodologies for monitoring lakes during the melt season are well-developed, their use is restricted by cloud cover and ice lids. This study provides a melt-season analysis of C- and L-band SAR data, demonstrating that VV/HH, LPR, and DoD parameters offer improved capabilities for lake detection compared to single-polarization channels. These findings offer critical insights toward developing SAR-based monitoring techniques that could complement or operate independently of optical approaches, providing consistent observational coverage irrespective of cloud conditions.

# Chapter 4. Thesis summary and future directions

Supraglacial lakes are an important component of the GrIS hydrologic system, connecting surface meltwater processes to the subglacial environment and influencing SMB and overall stability. Over approximately the past two decades, passive optical spaceborne sensors have provided foundational insights into supraglacial lake characteristics and dynamics. However, due to inherent observational limitations associated with these sensors, monitoring has primarily been restricted to the melt season. In this thesis, SAR was advanced as a tool for monitoring supraglacial lakes throughout both winter and melt seasons. For winter monitoring, we developed a novel methodology enabling the detection of supraglacial lake drainage events at high temporal resolution over a 10-year period. During the melt season, we assessed and compared the capabilities of quad and compact polarimetric SAR at both C- and L-bands for detecting supraglacial lakes, with a particular focus on distinguishing between lakes with and without ice lids.

Our findings presented in Chapter 2, "A decade of winter supraglacial lake drainage across NE Greenland using C-band SAR," reveal that winter drainage events are common and occurred in each winter season of the study period. These findings represent some of the first to clearly demonstrate the prevalence of this previously poorly understood process, including the first time series observations approaching a daily temporal resolution. Results highlight the importance of winter drainage events on supraglacial lake behaviour, alongside well-documented melt-season drainage and winter freeze-through processes. Importantly, the results demonstrated that these winter drainage events can induce increases in ice velocity and showed potential relationships with melt-season conditions both preceding and following the events, as indicated by an analysis linking winter events to melt intensity and melt-season drainage events.

Given the lack of adequate historical SAR data over the GrIS compared to optical datasets such as Landsat, continued monitoring of winter lake behaviour is necessary to document long-term trends that may not have been fully captured within the span of our 10-year study. This is particularly important as climate change may influence the spatiotemporal distribution and frequency of these drainage events. Furthermore, there remains a need to extend similar analyses to other regions of the GrIS, which would allow for an expanded investigation into how winter drainage influences ice dynamics and the subglacial and supraglacial hydrological systems. Future methodological advances could build upon the approach developed in Chapter 2 by creating a fully automated detection system. Additionally, incorporating SAR frequencies such as L-band from upcoming missions like NISAR and ROSE-L could enhance the temporal resolution and accuracy of the detection of winter drainage events.

In Chapter 3, "Melt season C- and L-band SAR backscatter observations of supraglacial lakes in Northeast Greenland," our analysis demonstrated superior separability of supraglacial lakes from surrounding ice sheet facies during the melt season, particularly using VV/HH at L-band and, in some melt season conditions, at C-band as well. Single polarization channels have limited ability to separate slush and open water lake areas, contributing to limited melt season utility. We also observed that the decision tree classifiers, Random Forest and XGBoost, produced comparable results, with most feature sets at both C-band and L-band benefiting from the inclusion of GLCM texture metrics. These findings establish a foundation for future SAR-based melt-season lake detection methodologies that could operate independently or in combination with optical datasets, enabling continuous time series mapping of lake evolution, unaffected by cloud cover. Furthermore, the use of L-band VV/HH enables the detection of meltwater areas hidden beneath perennial snow and ice lake lids. Future research may exploit this capability to provide estimates of melt water hidden beneath snow and ice lids covering lakes during the melt season.

In this study, we used optical imagery to identify ice-sheet facies, supporting the analysis of backscatter signatures and class separability for C- and L-band SAR data. However, incorporating in-situ field measurements would substantially improve the analysis by providing direct observations of snow and firn volumetric water content, thus facilitating a more robust interpretation of results. Additionally, snow pit excavations and ice-core sampling from lake lids would help clarify potential scattering mechanisms responsible for the observed low L-band VV/HH backscatter. Direct measurements of near-surface wind speeds and observations of wind-driven roughening of lake surfaces could further strengthen comparisons of C- versus L-band performance and limitations in detecting supraglacial lakes.

Supraglacial lakes play a significant role in both the surface and dynamic mass balance of the GrIS. While lake dynamics during the melt season have been extensively studied using optical remote sensing, understanding of wintertime lake behaviour remains comparatively limited, with SAR methodologies only recently adopted for winter observations. Complementary use of SAR during the melt season also remains constrained by challenges such as widespread meltwater presence and low dielectric contrast between lakes and adjacent ice and snow facies. In this thesis, we developed a novel SAR-based methodology for monitoring winter lake dynamics, enabling insights into rarely studied winter drainage events in NE Greenland. Furthermore, we demonstrated the potential of C- and L-band SAR for detecting supraglacial lakes and identifying meltwater beneath snow and ice lids during the melt season. Future research can build upon this work by extending process-based studies of supraglacial lakes to additional regions of the GrIS, and by further exploring complex SAR microwave scattering mechanisms through integration of in-situ field data and expanded spatiotemporal datasets. Continued development and application of SAR-based monitoring methodologies will be essential for advancing our knowledge of supraglacial lakes in the coming decades. This progress will be facilitated by ongoing availability of C-band SAR data from the RCM and Sentinel-1 satellites, as well as the anticipated launch of open-access, regularly acquired L-band SAR data from the forthcoming NISAR and ROSE-L missions.

# References


Andersen, J. K., N. Rathmann, C. S. Hvidberg, A. Grinsted, A. Kusk, J. P. Merryman Boncori, and J. Mouginot. 2023. “Episodic Subglacial Drainage Cascades Below the Northeast Greenland Ice Stream.” Geophysical Research Letters 50(12):e2023GL103240. doi:10.1029/2023GL103240.

Andrews, Lauren C., Ginny A. Catania, Matthew J. Hoffman, Jason D. Gulley, Martin P. Lüthi, Claudia Ryser, Robert L. Hawley, and Thomas A. Neumann. 2014. “Direct Observations of Evolving Subglacial Drainage beneath the Greenland Ice Sheet.” Nature 514(7520):80–83. doi:10.1038/nature13796.

Andrews, Lauren C., Matthew J. Hoffman, Thomas A. Neumann, Ginny A. Catania, Martin P. Lüthi, Robert L. Hawley, Kristin M. Schild, Claudia Ryser, and Blaine F. Morriss. 2018. “Seasonal Evolution of the Subglacial Hydrologic System Modified by Supraglacial Lake Drainage in Western Greenland.” Journal of Geophysical Research: Earth Surface 123(6):1479–96. doi:10.1029/2017JF004585.

Arthur, Jennifer F., Chris Stokes, Stewart SR Jamieson, J. Rachel Carr, and Amber A. Leeson. 2020. “Recent Understanding of Antarctic Supraglacial Lakes Using Satellite Remote Sensing.” Progress in Physical Geography: Earth and Environment 44(6):837–69. doi:10.1177/0309133320916114.

Aschwanden, Andy, Mark A. Fahnestock, Martin Truffer, Douglas J. Brinkerhoff, Regine Hock, Constantine Khroulev, Ruth Mottram, and S. Abbas Khan. 2019. “Contribution of the Greenland Ice Sheet to Sea Level over the next Millennium.” Science Advances 5(6):eaav9396. doi:10.1126/sciadv.aav9396.

Ashcraft, I. S., and D. G. Long. 2005. “Observation and Characterization of Radar Backscatter over Greenland.” IEEE Transactions on Geoscience and Remote Sensing 43(2):225–37. doi:10.1109/TGRS.2004.841484.

Banwell, Alison, Ian Hewitt, Ian Willis, and Neil Arnold. 2016. “Moulin Density Controls Drainage Development beneath the Greenland Ice Sheet.” Journal of Geophysical Research: Earth Surface 121(12):2248–69. doi:10.1002/2015JF003801.

Bartholomew, Ian, Peter Nienow, Douglas Mair, Alun Hubbard, Matt A. King, and Andrew Sole. 2010. “Seasonal Evolution of Subglacial Drainage and Acceleration in a Greenland Outlet Glacier.” Nature Geoscience 3(6):408–11. doi:10.1038/ngeo863.

Barzycka, Barbara, Mariusz Grabiec, Jacek Jania, Małgorzata Błaszczyk, Finnur Pálsson, Michał Laska, Dariusz Ignatiuk, and Guðfinna Aðalgeirsdóttir. 2023. “Comparison of Three Methods for Distinguishing Glacier Zones Using Satellite SAR Data.” Remote Sensing 15(3):690. doi:10.3390/rs15030690.

Benedek, Corinne L., and Ian C. Willis. 2021. “Winter Drainage of Surface Lakes on the Greenland Ice Sheet from Sentinel-1 SAR Imagery.” The Cryosphere 15(3):1587–1606. doi:10.5194/tc-15-1587-2021.

Box, Jason E., Alun Hubbard, David B. Bahr, William T. Colgan, Xavier Fettweis, Kenneth D. Mankoff, Adrien Wehrlé, Brice Noël, Michiel R. van den Broeke, Bert Wouters, Anders A. Bjørk, and Robert S. Fausto. 2022. “Greenland Ice Sheet Climate Disequilibrium and Committed Sea-Level Rise.” Nature Climate Change 12(9):808–13. doi:10.1038/s41558-022-01441-2.

Box, Jason E., and Kathleen Ski. 2007. “Remote Sounding of Greenland Supraglacial Melt Lakes: Implications for Subglacial Hydraulics.” Journal of Glaciology 53(181):257–65. doi:10.3189/172756507782202883.

Brangers, I., H. Lievens, C. Miège, M. Demuzere, L. Brucker, and G. J. M. De Lannoy. 2020. “Sentinel-1 Detects Firn Aquifers in the Greenland Ice Sheet.” Geophysical Research Letters 47(3):e2019GL085192. doi:10.1029/2019GL085192.

Breiman, Leo. 2001. “Random Forests.” Machine Learning 45(1):5–32. doi:10.1023/A:1010933404324.

Brunt, K. M., T. A. Neumann, and B. E. Smith. 2019. “Assessment of ICESat-2 Ice Sheet Surface Heights, Based on Comparisons Over the Interior of the Antarctic Ice Sheet.” Geophysical Research Letters 46(22):13072–78. doi:10.1029/2019GL084886.

Cafarella, Silvie Marie, Randall Scharien, Torsten Geldsetzer, Stephen Howell, Christian Haas, Rebecca Segal, and Sasha Nasonova. 2019. “Estimation of Level and Deformed First-Year Sea Ice Surface Roughness in the Canadian Arctic Archipelago from C- and L-Band Synthetic Aperture Radar.” Canadian Journal of Remote Sensing 45(3–4):457–75. doi:10.1080/07038992.2019.1647102.

Casey, J., Stephen Howell, Adrienne Tivy, and Christian Haas. 2016. “Separability of Sea Ice Types from Wide Swath C- and L-Band Synthetic Aperture Radar Imagery Acquired during the Melt Season.” Remote Sensing of Environment 174:314–28. doi:10.1016/j.rse.2015.12.021.

Chen, Tianqi, and Carlos Guestrin. 2016. “XGBoost: A Scalable Tree Boosting System.” Pp. 785–94 in Proceedings of the 22nd ACM SIGKDD International Conference on Knowledge Discovery and Data Mining. San Francisco California USA: ACM.

Christoffersen, Poul, Marion Bougamont, Alun Hubbard, Samuel H. Doyle, Shane Grigsby, and Rickard Pettersson. 2018. “Cascading Lake Drainage on the Greenland Ice Sheet Triggered by Tensile Shock and Fracture.” Nature Communications 9(1):1064. doi:10.1038/s41467-018-03420-8.

Chudley, Thomas R., Poul Christoffersen, Samuel H. Doyle, Marion Bougamont, Charlotte M. Schoonman, Bryn Hubbard, and Mike R. James. 2019. “Supraglacial Lake Drainage at a Fast-Flowing Greenlandic Outlet Glacier.” Proceedings of the National Academy of Sciences 116(51):25468–77. doi:10.1073/pnas.1913685116.

Cloude, S. R., and E. Pottier. 1996. “A Review of Target Decomposition Theorems in Radar Polarimetry.” IEEE Transactions on Geoscience and Remote Sensing 34(2):498–518. doi:10.1109/36.485127.

Cooley, Sarah W., and Poul Christoffersen. 2017. “Observation Bias Correction Reveals More Rapidly Draining Lakes on the Greenland Ice Sheet.” Journal of Geophysical Research: Earth Surface 122(10):1867–81. doi:10.1002/2017JF004255.

Cooper, Matthew G., and Laurence C. Smith. 2019. “Satellite Remote Sensing of the Greenland Ice Sheet Ablation Zone: A Review.” Remote Sensing 11(20):2405. doi:10.3390/rs11202405.

Culberg, Riley, Roger J. Michaelides, and Julie Z. Miller. 2024a. “Sentinel-1 Detection of Ice Slabs on the Greenland Ice Sheet.” The Cryosphere 18(5):2531–55. doi:10.5194/tc-18-2531-2024.

Das, Sarah B., Ian Joughin, Mark D. Behn, Ian M. Howat, Matt A. King, Dan Lizarralde, and Maya P. Bhatia. 2008. “Fracture Propagation to the Base of the Greenland Ice Sheet During Supraglacial Lake Drainage.” Science 320(5877):778–81. doi:10.1126/science.1153360.

Dell, Rebecca L., Alison F. Banwell, Ian C. Willis, Neil S. Arnold, Anna Ruth W. Halberstadt, Thomas R. Chudley, and Hamish D. Pritchard. 2022. “Supervised Classification of Slush and Ponded Water on Antarctic Ice Shelves Using Landsat 8 Imagery.” Journal of Glaciology 68(268):401–14. doi:10.1017/jog.2021.114.

Dirscherl, Mariel, Andreas J. Dietz, Christof Kneisel, and Claudia Kuenzer. 2020. “Automated Mapping of Antarctic Supraglacial Lakes Using a Machine Learning Approach.” Remote Sensing 12(7):1203. doi:10.3390/rs12071203.

Dirscherl, Mariel, Andreas J. Dietz, Christof Kneisel, and Claudia Kuenzer. 2021. “A Novel Method for Automated Supraglacial Lake Mapping in Antarctica Using Sentinel-1 SAR Imagery and Deep Learning.” Remote Sensing 13(2):197. doi:10.3390/rs13020197.

Doyle, S. H., A. L. Hubbard, C. F. Dow, G. A. Jones, A. Fitzpatrick, A. Gusmeroli, B. Kulessa, K. Lindback, R. Pettersson, and J. E. Box. 2013. “Ice Tectonic Deformation during the Rapid in Situ Drainage of a Supraglacial Lake on the Greenland Ice Sheet.” The Cryosphere 7(1):129–40. doi:10.5194/tc-7-129-2013.

Doyle, Samuel H., Alun Hubbard, Andrew A. W. Fitzpatrick, Dirk van As, Andreas B. Mikkelsen, Rickard Pettersson, and Bryn Hubbard. 2014. “Persistent Flow Acceleration within the Interior of the Greenland Ice Sheet.” Geophysical Research Letters 41(3):899–905. doi:10.1002/2013GL058933.

Dow, C. F., B. Kulessa, I. C. Rutt, V. C. Tsai, S. Pimentel, S. H. Doyle, D. van As, K. Lindbäck, R. Pettersson, G. A. Jones, and A. Hubbard. 2015. “Modeling of Subglacial Hydrological Development Following Rapid Supraglacial Lake Drainage.” Journal of Geophysical Research: Earth Surface 120(6):1127–47. doi:10.1002/2014JF003333.

Dunmire, D., J. T. M. Lenaerts, A. F. Banwell, N. Wever, J. Shragge, S. Lhermitte, R. Drews, F. Pattyn, J. S. S. Hansen, I. C. Willis, J. Miller, and E. Keenan. 2020. “Observations of Buried Lake Drainage on the Antarctic Ice Sheet.” Geophysical Research Letters 47(15):e2020GL087970. doi:10.1029/2020GL087970.

Dunmire, Devon, Alison F. Banwell, Nander Wever, Jan T. M. Lenaerts, and Rajashree Tri Datta. 2021. “Contrasting Regional Variability of Buried Meltwater Extent over 2 Years across the Greenland Ice Sheet.” The Cryosphere 15(6):2983–3005. doi:10.5194/tc-15-2983-2021.

Fahnestock, Mark, Robert Bindschadler, Ron Kwok, and Ken Jezek. 1993. “Greenland Ice Sheet Surface Properties and Ice Dynamics from ERS-1 SAR Imagery.” Science 262(5139):1530–34. doi:10.1126/science.262.5139.1530.

Fair, Zachary, Mark Flanner, Kelly M. Brunt, Helen Amanda Fricker, and Alex Gardner. 2020. “Using ICESat-2 and Operation IceBridge Altimetry for Supraglacial Lake Depth Retrievals.” The Cryosphere 14(11):4253–63. doi:10.5194/tc-14-4253-2020.

Fan, Yubin, Chang-Qing Ke, Lanhua Luo, Xiaoyi Shen, Stephen John Livingstone, and James M. Lea. 2025. “Expansion of Supraglacial Lake Area, Volume and Extent on the Greenland Ice Sheet from 1985 to 2023.” Journal of Glaciology 71:e4. doi:10.1017/jog.2024.87.

Fausto, Robert S., Dirk van As, Kenneth D. Mankoff, Baptiste Vandecrux, Michele Citterio, Andreas P. Ahlstrøm, Signe B. Andersen, William Colgan, Nanna B. Karlsson, Kristian K. Kjeldsen, Niels J. Korsgaard, Signe H. Larsen, Søren Nielsen, Allan Ø. Pedersen, Christopher L. Shields, Anne M. Solgaard, and Jason E. Box. 2021. “Programme for Monitoring of the Greenland Ice Sheet (PROMICE) Automatic Weather Station Data.” Earth System Science Data 13(8):3819–45. doi:10.5194/essd-13-3819-2021.

Fischer, Georg, Konstantinos P. Papathanassiou, and Irena Hajnsek. 2020. “Modeling and Compensation of the Penetration Bias in InSAR DEMs of Ice Sheets at Different Frequencies.” IEEE Journal of Selected Topics in Applied Earth Observations and Remote Sensing 13:2698–2707. doi:10.1109/JSTARS.2020.2992530.

Fitzpatrick, A. a. W., A. L. Hubbard, J. E. Box, D. J. Quincey, D. van As, A. P. B. Mikkelsen, S. H. Doyle, C. F. Dow, B. Hasholt, and G. A. Jones. 2014. “A Decade (2002-2012) of Supraglacial Lake Volume Estimates across Russell Glacier, West Greenland.” The Cryosphere 8(1):107–21. doi:10.5194/tc-8-107-2014.

Freeman, A., and S. L. Durden. 1998. “A Three-Component Scattering Model for Polarimetric SAR Data.” IEEE Transactions on Geoscience and Remote Sensing 36(3):963–73. doi:10.1109/36.673687.

Georgiou, S., A. Shepherd, M. McMillan, and P. Nienow. 2009. “Seasonal Evolution of Supraglacial Lake Volume from ASTER Imagery.” Annals of Glaciology 50(52):95–100. doi:10.3189/172756409789624328.

Gledhill, Laura A., and Andrew G. Williamson. 2018. “Inland Advance of Supraglacial Lakes in North-West Greenland under Recent Climatic Warming.” Annals of Glaciology 59(76pt1):66–82. doi:10.1017/aog.2017.31.

Gorelick, Noel, Matt Hancher, Mike Dixon, Simon Ilyushchenko, David Thau, and Rebecca Moore. 2017. “Google Earth Engine: Planetary-Scale Geospatial Analysis for Everyone.” Remote Sensing of Environment 202:18–27. doi:10.1016/j.rse.2017.06.031.

Grinsted, Aslak, Christine S. Hvidberg, David A. Lilien, Nicholas M. Rathmann, Nanna B. Karlsson, Tamara Gerber, Helle Astrid Kjær, Paul Vallelonga, and Dorthe Dahl-Jensen. 2022. “Accelerating Ice Flow at the Onset of the Northeast Greenland Ice Stream.” Nature Communications 13(1):5589. doi:10.1038/s41467-022-32999-2.

Halberstadt, Anna Ruth W., Colin J. Gleason, Mahsa S. Moussavi, Allen Pope, Luke D. Trusel, and Robert M. DeConto. 2020. “Antarctic Supraglacial Lake Identification Using Landsat-8 Image Classification.” Remote Sensing 12(8):1327. doi:10.3390/rs12081327.

Hall-Beyer, Mryka. 2017. “GLCM Texture: A Tutorial v. 3.0 March 2017.” doi:10.11575/PRISM/33280.

Hallikainen, M., F. Ulaby, and M. Abdelrazik. 1986. “Dielectric Properties of Snow in the 3 to 37 GHz Range.” IEEE Transactions on Antennas and Propagation 34(11):1329–40. doi:10.1109/TAP.1986.1143757.

Hambrey, M. J. 1977. “Supraglacial Drainage and Its Relationship to Structure, with Particular Reference to Charles Rabots Bre, Okstindan, Norway.” Norsk Geografisk Tidsskrift - Norwegian Journal of Geography 31(2):69–77. doi:10.1080/00291957708545319.

Hanna, Edward, Dániel Topál, Jason E. Box, Sammie Buzzard, Frazer D. W. Christie, Christine Hvidberg, Mathieu Morlighem, Laura De Santis, Alessandro Silvano, Florence Colleoni, Ingo Sasgen, Alison F. Banwell, Michiel R. van den Broeke, Robert DeConto, Jan De Rydt, Heiko Goelzer, Alexandra Gossart, G. Hilmar Gudmundsson, Katrin Lindbäck, Bertie Miles, Ruth Mottram, Frank Pattyn, Ronja Reese, Eric Rignot, Aakriti Srivastava, Sainan Sun, Justin Toller, Peter A. Tuckett, and Lizz Ultee. 2024. “Short- and Long-Term Variability of the Antarctic and Greenland Ice Sheets.” Nature Reviews Earth & Environment 5(3):193–210. doi:10.1038/s43017-023-00509-7.

Haralick, Robert M., K. Shanmugam, and Its’Hak Dinstein. 1973. “Textural Features for Image Classification.” IEEE Transactions on Systems, Man, and Cybernetics SMC-3(6):610–21. doi:10.1109/TSMC.1973.4309314.

Hersbach, Hans, Bill Bell, Paul Berrisford, Shoji Hirahara, András Horányi, Joaquín Muñoz-Sabater, Julien Nicolas, Carole Peubey, Raluca Radu, Dinand Schepers, Adrian Simmons, Cornel Soci, Saleh Abdalla, Xavier Abellan, Gianpaolo Balsamo, Peter Bechtold, Gionata Biavati, Jean Bidlot, Massimo Bonavita, Giovanna De Chiara, Per Dahlgren, Dick Dee, Michail Diamantakis, Rossana Dragani, Johannes Flemming, Richard Forbes, Manuel Fuentes, Alan Geer, Leo Haimberger, Sean Healy, Robin J. Hogan, Elías Hólm, Marta Janisková, Sarah Keeley, Patrick Laloyaux, Philippe Lopez, Cristina Lupu, Gabor Radnoti, Patricia de Rosnay, Iryna Rozum, Freja Vamborg, Sebastien Villaume, and Jean-Noël Thépaut. 2020. “The ERA5 Global Reanalysis.” Quarterly Journal of the Royal Meteorological Society 146(730):1999–2049. doi:10.1002/qj.3803.

Hinkel, Jochen, Daniel Lincke, Athanasios T. Vafeidis, Mahé Perrette, Robert James Nicholls, Richard S. J. Tol, Ben Marzeion, Xavier Fettweis, Cezar Ionescu, and Anders Levermann. 2014. “Coastal Flood Damage and Adaptation Costs under 21st Century Sea-Level Rise.” Proceedings of the National Academy of Sciences 111(9):3292–97. doi:10.1073/pnas.1222469111.

Hochreuther, Philipp, Niklas Neckel, Nathalie Reimann, Angelika Humbert, and Matthias Braun. 2021. “Fully Automated Detection of Supraglacial Lake Area for Northeast Greenland Using Sentinel-2 Time-Series.” Remote Sensing 13(2):205. doi:10.3390/rs13020205.

Hoffman, Matthew J., Mauro Perego, Lauren C. Andrews, Stephen F. Price, Thomas A. Neumann, Jesse V. Johnson, Ginny Catania, and Martin P. Lüthi. 2018. “Widespread Moulin Formation During Supraglacial Lake Drainages in Greenland.” Geophysical Research Letters 45(2):778–88. doi:10.1002/2017GL075659.

Hossain, Emam, Md Osman Gani, Devon Dunmire, Aneesh C. Subramanian, and Hammad Younas. 2024. “Time Series Classification of Supraglacial Lakes Evolution over Greenland Ice Sheet.” Pp. 490–97 in 2024 International Conference on Machine Learning and Applications (ICMLA).

How, Penelope, Douglas I. Benn, Nicholas R. J. Hulton, Bryn Hubbard, Adrian Luckman, Heïdi Sevestre, Ward J. J. van Pelt, Katrin Lindbäck, Jack Kohler, and Wim Boot. 2017. “Rapidly Changing Subglacial Hydrological Pathways at a Tidewater Glacier Revealed through Simultaneous Observations of Water Pressure, Supraglacial Lakes, Meltwater Plumes and Surface Velocities.” The Cryosphere 11(6):2691–2710. doi:10.5194/tc-11-2691-2017.

Howat, I. M., A. Negrete, and B. E. Smith. 2014. “The Greenland Ice Mapping Project (GIMP) Land Classification and Surface Elevation Data Sets.” The Cryosphere 8(4):1509–18. doi:10.5194/tc-8-1509-2014.

Howat, I. M., S. de la Peña, J. H. van Angelen, J. T. M. Lenaerts, and M. R. van den Broeke. 2013. "Brief Communication 'Expansion of Meltwater Lakes on the Greenland Ice Sheet.'" The Cryosphere 7(1):201–4. doi:10.5194/tc-7-201-2013.

Howat, Ian. 2017. MEaSUREs Greenland Ice Mapping Project (GIMP) Land Ice and Ocean Classification Mask: Version Version 1. NASA National Snow and Ice Data Center Distributed Active Archive Center. doi:10.5067/B8X58MQBFUPA.

Hvidberg, Christine S., Aslak Grinsted, Dorthe Dahl-Jensen, Shfaqat Abbas Khan, Anders Kusk, Jonas Kvist Andersen, Niklas Neckel, Anne Solgaard, Nanna B. Karlsson, Helle Astrid Kjær, and Paul Vallelonga. 2020. "Surface Velocity of the Northeast Greenland Ice Stream (NEGIS): Assessment of Interior Velocities Derived from Satellite Data by GPS." The Cryosphere 14(10):3487–3502. doi:10.5194/tc-14-3487-2020.

Ignéczi, Ádám, Andrew J. Sole, Stephen J. Livingstone, Amber A. Leeson, Xavier Fettweis, Nick Selmes, Noel Gourmelen, and Kate Briggs. 2016. "Northeast Sector of the Greenland Ice Sheet to Undergo the Greatest Inland Expansion of Supraglacial Lakes during the 21st Century." Geophysical Research Letters 43(18):9729–38. doi:10.1002/2016GL070338.

Ignéczi, Ádám, Andrew J. Sole, Stephen J. Livingstone, Felix S. L. Ng, and Kang Yang. 2018. "Greenland Ice Sheet Surface Topography and Drainage Structure Controlled by the Transfer of Basal Variability." Frontiers in Earth Science 6:101. doi:10.3389/feart.2018.00101.

Irvine-Fynn, Tristram D. L., Andrew J. Hodson, Brian J. Moorman, Geir Vatne, and Alun L. Hubbard. 2011. "Polythermal Glacier Hydrology: A Review." Reviews of Geophysics 49(4). doi:10.1029/2010RG000350.

Isoguchi, Osamu, and Masanobu Shimada. 2009. "An L-Band Ocean Geophysical Model Function Derived From PALSAR." *IEEE Transactions on Geoscience and Remote Sensing* 47(7):1925–36. doi:10.1109/TGRS.2008.2010864.

Jiang, Di, Xinwu Li, Ke Zhang, Sebastián Marinsek, Wen Hong, and Yirong Wu. 2022. "Automatic Supraglacial Lake Extraction in Greenland Using Sentinel-1 SAR Images and Attention-Based U-Net." Remote Sensing 14(19):4998. doi:10.3390/rs14194998.

Johansson, A. M., P. Jansson, and I. A. Brown. 2013. "Spatial and Temporal Variations in Lakes on the Greenland Ice Sheet." Journal of Hydrology 476:314–20. doi:10.1016/j.jhydrol.2012.10.045.

Johansson, Anna Malin, and Ian A. Brown. 2012. "Observations of Supra-Glacial Lakes in West Greenland Using Winter Wide Swath Synthetic Aperture Radar." Remote Sensing Letters 3(6):531–39. doi:10.1080/01431161.2011.637527.

Joughin, I. 2023. MEaSUREs Greenland Monthly Ice Sheet Velocity Mosaics from SAR and Landsat: Version Version 5. Boulder, Colorado USA: NASA National Snow and Ice Data Center Distributed Active Archive Center. doi:https://doi.org/10.5067/EGKZX6FXXM4P.

Joughin, Ian. 2022. MEaSUREs Greenland 6 and 12 day Ice Sheet Velocity Mosaics from SAR: Version Version 2. Boulder, Colorado USA: NASA National Snow and Ice Data Center Distributed Active Archive Center. doi:https://doi.org/10.5067/1AMEDB6VJ1NZ.

Joughin, Ian, Benjamin Smith, Ian Howat, and Ted Scambos. 2016. MEaSUREs Multi-year Greenland Ice Sheet Velocity Mosaic: Version Version 1. NASA National Snow and Ice Data Center Distributed Active Archive Center. doi:10.5067/QUA5Q9SVMSJG.

Kanzow, Torsten, Angelika Humbert, Thomas Mölg, Mirko Scheinert, Matthias Braun, Hans Burchard, Francesca Doglioni, Philipp Hochreuther, Martin Horwath, Oliver Huhn, Maria Kappelsberger, Jürgen Kusche, Erik Loebel, Katrina Lutz, Ben Marzeion, Rebecca McPherson, Mahdi Mohammadi-Aragh, Marco Möller, Carolyne Pickler, Markus Reinert, Monika Rhein, Martin Rückamp, Janin Schaffer, Muhammad Shafeeque, Sophie Stolzenberger, Ralph Timmermann, Jenny Turton, Claudia Wekerle, and Ole Zeising. 2025. "The System of Atmosphere, Land, Ice and Ocean in the Region near the 79N Glacier in Northeast Greenland: Synthesis and Key Findings from the Greenland Ice Sheet–Ocean Interaction (GROCE) Experiment." The Cryosphere 19(5):1789–1824. doi:10.5194/tc-19-1789-2025.

Khan, Shfaqat A., Youngmin Choi, Mathieu Morlighem, Eric Rignot, Veit Helm, Angelika Humbert, Jérémie Mouginot, Romain Millan, Kurt H. Kjær, and Anders A. Bjørk. 2022. "Extensive Inland Thinning and Speed-up of Northeast Greenland Ice Stream." Nature 611(7937):727–32. doi:10.1038/s41586-022-05301-z.

Koenig, L. S., D. J. Lampkin, L. N. Montgomery, S. L. Hamilton, J. B. Turrin, C. A. Joseph, S. E. Moutsafa, B. Panzer, K. A. Casey, J. D. Paden, C. Leuschen, and P. Gogineni. 2015. "Wintertime Storage of Water in Buried Supraglacial Lakes across the Greenland Ice Sheet." The Cryosphere 9(4):1333–42. doi:10.5194/tc-9-1333-2015.

König, Max, Jan-Gunnar Winther, and Elisabeth Isaksson. 2001. "Measuring Snow and Glacier Ice Properties from Satellite." Reviews of Geophysics 39(1):1–27. doi:10.1029/1999RG000076.

Kroupnik, Guennadi, Daniel De Lisle, Stephane Côté, Mélanie Lapointe, Catherine Casgrain, and Réjean Fortier. 2021. "RADARSAT Constellation Mission Overview and Status." Pp. 1–5 in 2021 IEEE Radar Conference (RadarConf21).

Kulp, Scott A., and Benjamin H. Strauss. 2019. "New Elevation Data Triple Estimates of Global Vulnerability to Sea-Level Rise and Coastal Flooding." Nature Communications 10(1):4844. doi:10.1038/s41467-019-12808-z.

Lampkin, D. J., and J. VanderBerg. 2011. “A Preliminary Investigation of the Influence of Basal and Surface Topography on Supraglacial Lake Distribution near Jakobshavn Isbrae, Western Greenland.” Hydrological Processes 25(21):3347–55. doi:10.1002/hyp.8170.

Lampkin, Derrick Julius, Lora Koenig, Casey Joseph, and Jason Eric Box. 2020. “Investigating Controls on the Formation and Distribution of Wintertime Storage of Water in Supraglacial Lakes.” Frontiers in Earth Science 8. https://www.frontiersin.org/articles/10.3389/feart.2020.00370.

Law, Robert, Neil Arnold, Corinne Benedek, Marco Tedesco, Alison Banwell, and Ian Willis. 2020. “Over-Winter Persistence of Supraglacial Lakes on the Greenland Ice Sheet: Results and Insights from a New Model.” Journal of Glaciology 66(257):362–72. doi:10.1017/jog.2020.7.

Lee, Jong-Sen, Jen-Hung Wen, T. L. Ainsworth, Kun-Shan Chen, and A. J. Chen. 2009. “Improved Sigma Filter for Speckle Filtering of SAR Imagery.” IEEE Transactions on Geoscience and Remote Sensing 47(1):202–13. doi:10.1109/TGRS.2008.2002881.

Leeson, A. A., A. Shepherd, K. Briggs, I. Howat, X. Fettweis, M. Morlighem, and E. Rignot. 2015. “Supraglacial Lakes on the Greenland Ice Sheet Advance Inland under Warming Climate.” Nature Climate Change 5(1):51–55. doi:10.1038/nclimate2463.

Legleiter, C. J., M. Tedesco, L. C. Smith, A. E. Behar, and B. T. Overstreet. 2014. “Mapping the Bathymetry of Supraglacial Lakes and Streams on the Greenland Ice Sheet Using Field Measurements and High-Resolution Satellite Images.” The Cryosphere 8(1):215–28. doi:10.5194/tc-8-215-2014.

Li, Ya, Kang Yang, Shuai Gao, Laurence C. Smith, Xavier Fettweis, and Manchun Li. 2022. “Surface Meltwater Runoff Routing through a Coupled Supraglacial-Proglacial Drainage System, Inglefield Land, Northwest Greenland.” International Journal of Applied Earth Observation and Geoinformation 106:102647. doi:10.1016/j.jag.2021.102647.

Liang, Yu-Li, William Colgan, Qin Lv, Konrad Steffen, Waleed Abdalati, Julienne Stroeve, David Gallaher, and Nicolas Bayou. 2012. “A Decadal Investigation of Supraglacial Lakes in West Greenland Using a Fully Automatic Detection and Tracking Algorithm.” Remote Sensing of Environment 123:127–38. doi:10.1016/j.rse.2012.03.020.

Livingstone, S. J., C. D. Clark, J. Woodward, and J. Kingslake. 2013. “Potential Subglacial Lake Locations and Meltwater Drainage Pathways beneath the Antarctic and Greenland Ice Sheets.” The Cryosphere 7(6):1721–40. doi:10.5194/tc-7-1721-2013.

Lu, Yao, Kang Yang, Xin Lu, Ya Li, Shuai Gao, Wei Mao, and Manchun Li. 2021. “Response of Supraglacial Rivers and Lakes to Ice Flow and Surface Melt on the Northeast Greenland Ice Sheet during the 2017 Melt Season.” Journal of Hydrology 602:126750. doi:10.1016/j.jhydrol.2021.126750.

Lutz, Katrina, Zahra Bahrami, and Matthias Braun. 2023. “Supraglacial Lake Evolution over Northeast Greenland Using Deep Learning Methods.” Remote Sensing 15(17):4360. doi:10.3390/rs15174360.

Lutz, Katrina, Ilaria Tabone, Angelika Humbert, and Matthias Braun. 2025. “Multi-Annual Patterns of Rapidly Draining Supraglacial Lakes in Northeast Greenland.” The Cryosphere 19(7):2601–14. doi:10.5194/tc-19-2601-2025.

Lutz, Katrina, Ilaria Tabone, Angelika Humbert, and Matthias Holger Braun. 2024. “Rapid Drainages of Supraglacial Lakes in Northeast Greenland from 2016 - 2022 Observed through Sentinel-2 Imagery.” PANGAEA. doi:10.1594/PANGAEA.973446.

Mahmud, Mallik S., Torsten Geldsetzer, Stephen E. L. Howell, John J. Yackel, Vishnu Nandan, and Randall K. Scharien. 2018. “Incidence Angle Dependence of HH-Polarized C- and L-Band Wintertime Backscatter Over Arctic Sea Ice.” IEEE Transactions on Geoscience and Remote Sensing 56(11):6686–98. doi:10.1109/TGRS.2018.2841343.

Mahmud, Mallik S., Vishnu Nandan, Suman Singha, Stephen E. L. Howell, Torsten Geldsetzer, John Yackel, and Benoit Montpetit. 2022. “C- and L-Band SAR Signatures of Arctic Sea Ice during Freeze-Up.” Remote Sensing of Environment 279:113129. doi:10.1016/j.rse.2022.113129.

Maier, Nathan, Jonas Kvist Andersen, Jérémie Mouginot, Florent Gimbert, and Olivier Gagliardini. 2023. “Wintertime Supraglacial Lake Drainage Cascade Triggers Large-Scale Ice Flow Response in Greenland.” Geophysical Research Letters 50(4):e2022GL102251. doi:10.1029/2022GL102251.

Mantelli, E., C. Camporeale, and L. Ridolfi. 2015. “Supraglacial Channel Inception: Modeling and Processes.” Water Resources Research 51(9):7044–63. doi:10.1002/2015WR017075.

Mayaud, Jerome R., Alison F. Banwell, Neil S. Arnold, and Ian C. Willis. 2014. “Modeling the Response of Subglacial Drainage at Paakitsoq, West Greenland, to 21st Century Climate Change.” Journal of Geophysical Research: Earth Surface 119(12):2619–34. doi:10.1002/2014JF003271.

Melling, Laura, Amber Leeson, Malcolm McMillan, Jennifer Maddalena, Jade Bowling, Emily Glen, Louise Sandberg Sørensen, Mai Winstrup, and Rasmus Lørup Arildsen. 2024. “Evaluation of Satellite Methods for Estimating Supraglacial Lake Depth in Southwest Greenland.” The Cryosphere 18(2):543–58. doi:10.5194/tc-18-543-2024.

Miège, Clément, Richard R. Forster, Ludovic Brucker, Lora S. Koenig, D. Kip Solomon, John D. Paden, Jason E. Box, Evan W. Burgess, Julie Z. Miller, Laura McNerney, Noah Brautigam, Robert S. Fausto, and Sivaprasad Gogineni. 2016.

"Spatial Extent and Temporal Variability of Greenland Firn Aquifers Detected by Ground and Airborne Radars." Journal of Geophysical Research: Earth Surface 121(12):2381–98. doi:10.1002/2016JF003869.

Miles, Katie E., Ian C. Willis, Corinne L. Benedek, Andrew G. Williamson, and Marco Tedesco. 2017. "Toward Monitoring Surface and Subsurface Lakes on the Greenland Ice Sheet Using Sentinel-1 SAR and Landsat-8 OLI Imagery." Frontiers in Earth Science 5:58. doi:10.3389/feart.2017.00058.

Miller, Julie Z., Riley Culberg, David G. Long, Christopher A. Shuman, Dustin M. Schroeder, and Mary J. Brodzik. 2022. "An Empirical Algorithm to Map Perennial Firn Aquifers and Ice Slabs within the Greenland Ice Sheet Using Satellite L-Band Microwave Radiometry." The Cryosphere 16(1):103–25. doi:10.5194/tc-16-103-2022.

Morlighem, M. 2022. "IceBridge BedMachine Greenland. (IDBMG4, Version 5)." Boulder, Colorado USA: NASA National Snow and Ice Data Center Distributed Active Archive Center. doi:10.5067/GMEVBWFLWA7X.

Morlighem, M., C. N. Williams, E. Rignot, L. An, J. E. Arndt, J. L. Bamber, G. Catania, N. Chauché, J. A. Dowdeswell, B. Dorschel, I. Fenty, K. Hogan, I. Howat, A. Hubbard, M. Jakobsson, T. M. Jordan, K. K. Kjeldsen, R. Millan, L. Mayer, J. Mouginot, B. P. Y. Noël, C. O'Cofaigh, S. Palmer, S. Rysgaard, H. Seroussi, M. J. Siegert, P. Slabon, F. Straneo, M. R. van den Broeke, W. Weinrebe, M. Wood, and K. B. Zinglersen. 2017. "BedMachine v3: Complete Bed Topography and Ocean Bathymetry Mapping of Greenland From Multibeam Echo Sounding Combined With Mass Conservation." Geophysical Research Letters 44(21):11,051-11,061. doi:10.1002/2017GL074954.

Morriss, B. F., R. L. Hawley, J. W. Chipman, L. C. Andrews, G. A. Catania, M. J. Hoffman, M. P. Lüthi, and T. A. Neumann. 2013. "A Ten-Year Record of Supraglacial Lake Evolution and Rapid Drainage in West Greenland Using an Automated Processing Algorithm for Multispectral Imagery." The Cryosphere 7(6):1869–77. doi:10.5194/tc-7-1869-2013.

Mouginot, J., E. Rignot, B. Scheuchl, I. Fenty, A. Khazendar, M. Morlighem, A. Buzzi, and J. Paden. 2015. "Fast Retreat of Zachariæ Isstrøm, Northeast Greenland." Science 350(6266):1357–61. doi:10.1126/science.aac7111.

Mouginot, Jeremie, and Eric Rignot. 2019. "Glacier Catchments/Basins for the Greenland Ice Sheet." Dryad. doi:10.7280/D1WT11.

Mouginot, Jérémie, Eric Rignot, Anders A. Bjørk, Michiel van den Broeke, Romain Millan, Mathieu Morlighem, Brice Noël, Bernd Scheuchl, and Michael Wood. 2019. "Forty-Six Years of Greenland Ice Sheet Mass Balance from 1972 to 2018." Proceedings of the National Academy of Sciences 116(19):9239–44. doi:10.1073/pnas.1904242116.

Nasonova, Sasha, Scharien ,Randall K., Geldsetzer ,Torsten, Howell ,Stephen E. L., and Desmond and Power. 2018. "Optimal Compact Polarimetric Parameters and Texture Features for Discriminating Sea Ice Types during Winter and Advanced Melt." Canadian Journal of Remote Sensing 44(4):390–411. doi:10.1080/07038992.2018.1527683.

Neckel, Niklas, Ole Zeising, Daniel Steinhage, Veit Helm, and Angelika Humbert. 2020. "Seasonal Observations at 79°N Glacier (Greenland) From Remote Sensing and in Situ Measurements." Frontiers in Earth Science 8. https://www.frontiersin.org/articles/10.3389/feart.2020.00142.

Neumann, Tom, Anita Brenner, David Hancock, John Robins, Jack Saba, Kaitlin Harbeck, Aimee Gibbons, Jeffery Lee, Scott Luthcke, and Tim Rebold. 2023. "Ice, Cloud, and Land Elevation Satellite (ICESat-2) Project Algorithm Theoretical Basis Document (ATBD) for Global Geolocated Photons ATL03, Version 6." doi:10.5067/GA5KCLJT7LOT.

Noh, Myoung-Jong, and Ian M. Howat. 2015. "Automated Stereo-Photogrammetric DEM Generation at High Latitudes: Surface Extraction with TIN-Based Search-Space Minimization (SETSM) Validation and Demonstration over Glaciated Regions." GIScience & Remote Sensing 52(2):198–217. doi:10.1080/15481603.2015.1008621.

O'Callaghan, John F., and David M. Mark. 1984. "The Extraction of Drainage Networks from Digital Elevation Data." Computer Vision, Graphics, and Image Processing 28(3):323–44. doi:10.1016/S0734-189X(84)80011-0.

Otosaka, Inès N., Andrew Shepherd, Erik R. Ivins, Nicole-Jeanne Schlegel, Charles Amory, Michiel R. van den Broeke, Martin Horwath, Ian Joughin, Michalea D. King, Gerhard Krinner, Sophie Nowicki, Anthony J. Payne, Eric Rignot, Ted Scambos, Karen M. Simon, Benjamin E. Smith, Louise S. Sørensen, Isabella Velicogna, Pippa L. Whitehouse, Geruo A, Cécile Agosta, Andreas P. Ahlstrøm, Alejandro Blazquez, William Colgan, Marcus E. Engdahl, Xavier Fettweis, Rene Forsberg, Hubert Gallée, Alex Gardner, Lin Gilbert, Noel Gourmelen, Andreas Groh, Brian C. Gunter, Christopher Harig, Veit Helm, Shfaqat Abbas Khan, Christoph Kittel, Hannes Konrad, Peter L. Langen, Benoit S. Lecavalier, Chia-Chun Liang, Bryant D. Loomis, Malcolm McMillan, Daniele Melini, Sebastian H. Mernild, Ruth Mottram, Jeremie Mouginot, Johan Nilsson, Brice Noël, Mark E. Pattle, William R. Peltier, Nadege Pie, Mònica Roca, Ingo Sasgen, Himanshu V. Save, Ki-Weon Seo, Bernd Scheuchl, Ernst J. O. Schrama, Ludwig Schröder, Sebastian B. Simonsen, Thomas Slater, Giorgio Spada, Tyler C. Sutterley, Bramha Dutt Vishwakarma, Jan Melchior van Wessem, David Wiese, Wouter van der Wal, and Bert Wouters. 2023. "Mass Balance of the Greenland and Antarctic Ice Sheets from 1992 to 2020." Earth System Science Data 15(4):1597–1616. doi:10.5194/essd-15-1597-2023.

Otto, Jacqueline, Felicity A. Holmes, and Nina Kirchner. 2022. "Supraglacial Lake Expansion, Intensified Lake Drainage Frequency, and First Observation of Coupled Lake Drainage, during 1985–2020 at Ryder Glacier, Northern Greenland." Frontiers in Earth Science 10. https://www.frontiersin.org/articles/10.3389/feart.2022.978137.

Pedregosa, Fabian, Gael Varoquaux, Alexandre Gramfort, Vincent Michel, Bertrand Thirion, Olivier Grisel, Mathieu Blondel, Peter Prettenhofer, Ron Weiss, Vincent Dubourg, Jake Vanderplas, Alexandre Passos, and David Cournapeau. n.d. "Scikit-Learn: Machine Learning in Python." MACHINE LEARNING IN PYTHON.

Pitcher, Lincoln H., and Laurence C. Smith. 2019. "Supraglacial Streams and Rivers." Annual Review of Earth and Planetary Sciences 47(1):421–52. doi:10.1146/annurev-earth-053018-060212.

Poinar, Kristin, and Lauren C. Andrews. 2021. "Challenges in Predicting Greenland Supraglacial Lake Drainages at the Regional Scale." The Cryosphere 15(3):1455–83. doi:10.5194/tc-15-1455-2021.

Poinar, Kristin, Ian Joughin, Sarah B. Das, Mark D. Behn, Jan T. M. Lenaerts, and Michiel R. van den Broeke. 2015. "Limits to Future Expansion of Surface-Melt-Enhanced Ice Flow into the Interior of Western Greenland." Geophysical Research Letters 42(6):1800–1807. doi:10.1002/2015GL063192.

Pope, A., T. A. Scambos, M. Moussavi, M. Tedesco, M. Willis, D. Shean, and S. Grigsby. 2016. "Estimating Supraglacial Lake Depth in West Greenland Using Landsat 8 and Comparison with Other Multispectral Methods." The Cryosphere 10(1):15–27. doi:10.5194/tc-10-15-2016.

Porter, Claire, Ian Howat, Myoung-Jon Noh, Erik Husby, Samuel Khuvis, Evan Danish, Karen Tomko, Judith Gardiner, Adelaide Negrete, Bidhyananda Yadav, James Klassen, Cole Kelleher, Michael Cloutier, Jesse Bakker, Jeremy Enos, Galen Arnold, Greg Bauer, and Paul Morin. 2022. ArcticDEM - Strips, Version 4.1: Version 1.4. Harvard Dataverse. doi:10.7910/DVN/C98DVS.

Porter, Claire, Ian Howat, Myoung-Jon Noh, Erik Husby, Samuel Khuvis, Evan Danish, Karen Tomko, Judith Gardiner, Adelaide Negrete, Bidhyananda Yadav, James Klassen, Cole Kelleher, Michael Cloutier, Jesse Bakker, Jeremy Enos, Galen Arnold, Greg Bauer, and Paul Morin. 2023. "ArcticDEM - Mosaics, Version 4.1." Harvard Dataverse. doi:10.7910/DVN/3VDC4W.

Rignot, Eric, Keith Echelmeyer, and William Krabill. 2001. "Penetration Depth of Interferometric Synthetic-Aperture Radar Signals in Snow and Ice." Geophysical Research Letters 28(18):3501–4. doi:10.1029/2000GL012484.

Rignot, Eric, Michele Koppes, and Isabella Velicogna. 2010. "Rapid Submarine Melting of the Calving Faces of West Greenland Glaciers." Nature Geoscience 3(3):187–91. doi:10.1038/ngeo765.

Russell, Andrew J. 1993. "Supraglacial Lake Drainage near Sendre Strømjjord, Greenland." Journal of Glaciology 39(132):431–33. doi:10.3189/S0022143000016105.

Ryan, J. C., L. C. Smith, D. van As, S. W. Cooley, M. G. Cooper, L. H. Pitcher, and A. Hubbard. 2019. "Greenland Ice Sheet Surface Melt Amplified by Snowline Migration and Bare Ice Exposure." Science Advances 5(3):eaav3738. doi:10.1126/sciadv.aav3738.

Scharien, R. K., J. Landy, and D. G. Barber. 2014. "First-Year Sea Ice Melt Pond Fraction Estimation from Dual-Polarisation C-Band SAR – Part 1: In Situ Observations." The Cryosphere 8(6):2147–62. doi:10.5194/tc-8-2147-2014.

Scharien, R. K., J. J. Yackel, D. G. Barber, M. Asplin, M. Gupta, and D. Isleifson. 2012. "Geophysical Controls on C Band Polarimetric Backscatter from Melt Pond Covered Arctic First-Year Sea Ice: Assessment Using High-Resolution Scatterometry." Journal of Geophysical Research: Oceans 117(C9). doi:10.1029/2011JC007353.

Scharien, Randall Kenneth, and Sasha Nasonova. 2022. "Incidence Angle Dependence of Texture Statistics From Sentinel-1 HH-Polarization Images of Winter Arctic Sea Ice." IEEE Geoscience and Remote Sensing Letters 19:1–5. doi:10.1109/LGRS.2020.3039739.

Schröder, Ludwig, Niklas Neckel, Robin Zindler, and Angelika Humbert. 2020. "Perennial Supraglacial Lakes in Northeast Greenland Observed by Polarimetric SAR." Remote Sensing 12(17):2798. doi:10.3390/rs12172798.

Selmes, N., T. Murray, and T. D. James. 2011. "Fast Draining Lakes on the Greenland Ice Sheet." Geophysical Research Letters 38(15). doi:10.1029/2011GL047872.

Shepherd, Andrew, Erik Ivins, Eric Rignot, Ben Smith, Michiel van den Broeke, Isabella Velicogna, Pippa Whitehouse, Kate Briggs, Ian Joughin, Gerhard Krinner, Sophie Nowicki, Tony Payne, Ted Scambos, Nicole Schlegel, Geruo A, Cécile Agosta, Andreas Ahlstrøm, Greg Babonis, Valentina R. Barletta, Anders A. Bjørk, Alejandro Blazquez, Jennifer Bonin, William Colgan, Beata Csatho, Richard Cullather, Marcus E. Engdahl, Denis Felikson, Xavier Fettweis, Rene Forsberg, Anna E. Hogg, Hubert Gallee, Alex Gardner, Lin Gilbert, Noel Gourmelen, Andreas Groh, Brian Gunter, Edward Hanna, Christopher Harig, Veit Helm, Alexander Horvath, Martin Horwath, Shfaqat Khan, Kristian K. Kjeldsen, Hannes Konrad, Peter L. Langen, Benoit Lecavalier, Bryant Loomis, Scott Luthcke, Malcolm McMillan, Daniele Melini, Sebastian Mernild, Yara Mohajerani, Philip Moore, Ruth Mottram, Jeremie Mouginot, Gorka Moyano, Alan Muir, Thomas Nagler, Grace Nield, Johan Nilsson, Brice Noël, Ines Otosaka, Mark E. Pattle, W. Richard Peltier, Nadège Pie, Roelof Rietbroek, Helmut Rott, Louise Sandberg Sørensen, Ingo Sasgen, Himanshu Save, Bernd Scheuchl, Ernst Schrama, Ludwig Schröder, Ki-Weon Seo, Sebastian B. Simonsen, Thomas Slater, Giorgio Spada, Tyler Sutterley, Matthieu Talpe, Lev Tarasov, Willem Jan van de Berg, Wouter van der Wal, Melchior van Wessem, Bramha Dutt Vishwakarma, David Wiese, David Wilton, Thomas Wagner, Bert Wouters, Jan Wuite, and The IMBIE Team. 2020. "Mass Balance of the Greenland Ice Sheet from 1992 to 2018." Nature 579(7798):233–39. doi:10.1038/s41586-019-1855-2.

Shreve, R. L. 1972. “Movement of Water in Glaciers.” Journal of Glaciology 11(62):205–14. doi:10.3189/S002214300002219X.

Singha, Suman, and Rudolf Ressel. 2017. “Arctic Sea Ice Characterization Using RISAT-1 Compact-Pol SAR Imagery and Feature Evaluation: A Case Study Over Northeast Greenland.” IEEE Journal of Selected Topics in Applied Earth Observations and Remote Sensing 10(8):3504–14. doi:10.1109/JSTARS.2017.2691258.

Slater, Thomas, Anna E. Hogg, and Ruth Mottram. 2020. “Ice-Sheet Losses Track High-End Sea-Level Rise Projections.” Nature Climate Change 10(10):879–81. doi:10.1038/s41558-020-0893-y.

Smith, Benjamin E., Noel Gourmelen, Alexander Huth, and Ian Joughin. 2017. “Connected Subglacial Lake Drainage beneath Thwaites Glacier, West Antarctica.” The Cryosphere 11(1):451–67. doi:10.5194/tc-11-451-2017.

Smith, L. C., L. C. Andrews, L. H. Pitcher, B. T. Overstreet, Å. K. Rennermalm, M. G. Cooper, S. W. Cooley, J. C. Ryan, C. Miège, C. Kershner, and C. E. Simpson. 2021. “Supraglacial River Forcing of Subglacial Water Storage and Diurnal Ice Sheet Motion.” Geophysical Research Letters 48(7):e2020GL091418. doi:10.1029/2020GL091418.

Smith, Laurence C., Vena W. Chu, Kang Yang, Colin J. Gleason, Lincoln H. Pitcher, Asa K. Rennermalm, Carl J. Legleiter, Alberto E. Behar, Brandon T. Overstreet, Samiah E. Moustafa, Marco Tedesco, Richard R. Forster, Adam L. LeWinter, David C. Finnegan, Yongwei Sheng, and James Balog. 2015. “Efficient Meltwater Drainage through Supraglacial Streams and Rivers on the Southwest Greenland Ice Sheet.” Proceedings of the National Academy of Sciences 112(4):1001–6. doi:10.1073/pnas.1413024112.

Smith, Laurence C., Kang Yang, Lincoln H. Pitcher, Brandon T. Overstreet, Vena W. Chu, Åsa K. Rennermalm, Jonathan C. Ryan, Matthew G. Cooper, Colin J. Gleason, Marco Tedesco, Jeyavinoth Jeyaratnam, Dirk van As, Michiel R. van den Broeke, Willem Jan van de Berg, Brice Noël, Peter L. Langen, Richard I. Cullather, Bin Zhao, Michael J. Willis, Alun Hubbard, Jason E. Box, Brittany A. Jenner, and Alberto E. Behar. 2017. “Direct Measurements of Meltwater Runoff on the Greenland Ice Sheet Surface.” Proceedings of the National Academy of Sciences 114(50):E10622–31. doi:10.1073/pnas.1707743114.

Sneed, W. A., and G. S. Hamilton. 2007. “Evolution of Melt Pond Volume on the Surface of the Greenland Ice Sheet.” Geophysical Research Letters 34(3). doi:10.1029/2006GL028697.

Sole, Andrew, Peter Nienow, Ian Bartholomew, Douglas Mair, Thomas Cowton, Andrew Tedstone, and Matt A. King. 2013. “Winter Motion Mediates Dynamic Response of the Greenland Ice Sheet to Warmer Summers.” Geophysical Research Letters 40(15):3940–44. doi:10.1002/grl.50764.

Stevens, Laura A., Mark D. Behn, Jeffrey J. McGuire, Sarah B. Das, Ian Joughin, Thomas Herring, David E. Shean, and Matt A. King. 2015. “Greenland Supraglacial Lake Drainages Triggered by Hydrologically Induced Basal Slip.” Nature 522(7554):73–76. doi:10.1038/nature14480.

Stevens, Laura A., Sarah B. Das, Mark D. Behn, Jeffrey J. McGuire, Ching-Yao Lai, Ian Joughin, Stacy Larochelle, and Meredith Nettles. 2024. “Elastic Stress Coupling Between Supraglacial Lakes.” Journal of Geophysical Research: Earth Surface 129(5):e2023JF007481. doi:10.1029/2023JF007481.

Stevens, Laura A., Meredith Nettles, James L. Davis, Timothy T. Creyts, Jonathan Kingslake, Ian J. Hewitt, and Aaron Stubblefield. 2022. “Tidewater-Glacier Response to Supraglacial Lake Drainage.” Nature Communications 13(1):6065. doi:10.1038/s41467-022-33763-2.

Sundal, A. V., A. Shepherd, P. Nienow, E. Hanna, S. Palmer, and P. Huybrechts. 2009. “Evolution of Supra-Glacial Lakes across the Greenland Ice Sheet.” Remote Sensing of Environment 113(10):2164–71. doi:10.1016/j.rse.2009.05.018.

Tavri, Aikaterini, Randall Scharien, and Torsten Geldsetzer. 2023. “Melt Season Arctic Sea Ice Type Separability Using Fully and Compact Polarimetric C- and L-Band Synthetic Aperture Radar.” Canadian Journal of Remote Sensing 49(1):2271578. doi:10.1080/07038992.2023.2271578.

Tedesco, M., M. Lüthje, K. Steffen, N. Steiner, X. Fettweis, I. Willis, N. Bayou, and A. Banwell. 2012. “Measurement and Modeling of Ablation of the Bottom of Supraglacial Lakes in Western Greenland.” Geophysical Research Letters 39(2). doi:10.1029/2011GL049882.

Tedesco, M., and N. Steiner. 2011. “In-Situ Multispectral and Bathymetric Measurements over a Supraglacial Lake in Western Greenland Using a Remotely Controlled Watercraft.” The Cryosphere 5(2):445–52. doi:10.5194/tc-5-445-2011.

Tedesco, Marco. 2014. Remote Sensing of the Cryosphere. John Wiley & Sons.

Tedesco, Marco, Ian C. Willis, Matthew J. Hoffman, Alison F. Banwell, Patrick Alexander, and Neil S. Arnold. 2013. “Ice Dynamic Response to Two Modes of Surface Lake Drainage on the Greenland Ice Sheet.” Environmental Research Letters 8(3):034007. doi:10.1088/1748-9326/8/3/034007.

Tedstone, Andrew J., Peter W. Nienow, Andrew J. Sole, Douglas W. F. Mair, Thomas R. Cowton, Ian D. Bartholomew, and Matt A. King. 2013. “Greenland Ice Sheet Motion Insensitive to Exceptional Meltwater Forcing.” Proceedings of the National Academy of Sciences 110(49):19719–24. doi:10.1073/pnas.1315843110.

Turton, Jenny V., Philipp Hochreuther, Nathalie Reimann, and Manuel T. Blau. 2021. "The Distribution and Evolution of Supraglacial Lakes on 79° N Glacier (North-Eastern Greenland) and Interannual Climatic Controls." The Cryosphere 15(8):3877–96. doi:10.5194/tc-15-3877-2021.

Ulaby, Fawwaz T., W. Herschel Stiles, and Mohamed Abdelrazik. 1984. "Snowcover Influence on Backscattering from Terrain." IEEE Transactions on Geoscience and Remote Sensing GE-22(2):126–33. doi:10.1109/TGRS.1984.350604.

Vitousek, Sean, Patrick L. Barnard, Charles H. Fletcher, Neil Frazer, Li Erikson, and Curt D. Storlazzi. 2017. "Doubling of Coastal Flooding Frequency within Decades Due to Sea-Level Rise." Scientific Reports 7(1):1399. doi:10.1038/s41598-017-01362-7.

Wang, Yefan, and Shin Sugiyama. 2024. "Supraglacial Lake Evolution on Tracy and Heilprin Glaciers in Northwestern Greenland from 2014 to 2021." Remote Sensing of Environment 303:114006. doi:10.1016/j.rse.2024.114006.

Wendleder, Anna, Andreas Schmitt, Thilo Erbertseder, Pablo D'Angelo, Christoph Mayer, and Matthias H. Braun. 2021. "Seasonal Evolution of Supraglacial Lakes on Baltoro Glacier From 2016 to 2020." Frontiers in Earth Science 9. https://www.frontiersin.org/articles/10.3389/feart.2021.725394.

Williamson, Andrew G., Neil S. Arnold, Alison F. Banwell, and Ian C. Willis. 2017. "A Fully Automated Supraglacial Lake Area and Volume Tracking ('FAST') Algorithm: Development and Application Using MODIS Imagery of West Greenland." Remote Sensing of Environment 196:113–33. doi:10.1016/j.rse.2017.04.032.

Williamson, Andrew G., Alison F. Banwell, Ian C. Willis, and Neil S. Arnold. 2018. "Dual-Satellite (Sentinel-2 and Landsat 8) Remote Sensing of Supraglacial Lakes in Greenland." The Cryosphere 12(9):3045–65. doi:10.5194/tc-12-3045-2018.

Williamson, Andrew G., Ian C. Willis, Neil S. Arnold, and Alison F. Banwell. 2018. "Controls on Rapid Supraglacial Lake Drainage in West Greenland: An Exploratory Data Analysis Approach." Journal of Glaciology 64(244):208–26. doi:10.1017/jog.2018.8.

Yang, Kang, and Laurence C. Smith. 2013. "Supraglacial Streams on the Greenland Ice Sheet Delineated From Combined Spectral–Shape Information in High-Resolution Satellite Imagery." IEEE Geoscience and Remote Sensing Letters 10(4):801–5. doi:10.1109/LGRS.2012.2224316.

Yang, Kang, and Laurence C. Smith. 2016. "Internally Drained Catchments Dominate Supraglacial Hydrology of the Southwest Greenland Ice Sheet." Journal of Geophysical Research: Earth Surface 121(10):1891–1910. doi:10.1002/2016JF003927.

Yang, Kang, Laurence C. Smith, Matthew G. Cooper, Lincoln H. Pitcher, Dirk van As, Yao Lu, Xin Lu, and Manchun Li. 2021. "Seasonal Evolution of Supraglacial Lakes and Rivers on the Southwest Greenland Ice Sheet." Journal of Glaciology 67(264):592–602. doi:10.1017/jog.2021.10.

Yang, Kang, Laurence C. Smith, Xavier Fettweis, Colin J. Gleason, Yao Lu, and Manchun Li. 2019. "Surface Meltwater Runoff on the Greenland Ice Sheet Estimated from Remotely Sensed Supraglacial Lake Infilling Rate." Remote Sensing of Environment 234:111459. doi:10.1016/j.rse.2019.111459.

Yang, Kang, Laurence C. Smith, Andrew Sole, Stephen J. Livingstone, Xiao Cheng, Zhuoqi Chen, and Manchun Li. 2019. "Supraglacial Rivers on the Northwest Greenland Ice Sheet, Devon Ice Cap, and Barnes Ice Cap Mapped Using Sentinel-2 Imagery." International Journal of Applied Earth Observation and Geoinformation 78:1–13. doi:10.1016/j.jag.2019.01.008.

Young, Tun Jan, Poul Christoffersen, Marion Bougamont, Slawek M. Tulaczyk, Bryn Hubbard, Kenneth D. Mankoff, Keith W. Nicholls, and Craig L. Stewart. 2022. "Rapid Basal Melting of the Greenland Ice Sheet from Surface Meltwater Drainage." Proceedings of the National Academy of Sciences 119(10):e2116036119. doi:10.1073/pnas.2116036119.

Yuan, Jiawei, Zhaohui Chi, Xiao Cheng, Tao Zhang, Tian Li, and Zhuoqi Chen. 2020. "Automatic Extraction of Supraglacial Lakes in Southwest Greenland during the 2014–2018 Melt Seasons Based on Convolutional Neural Network." Water 12(3):891. doi:10.3390/w12030891.

Zeising, Ole, Niklas Neckel, Nils Dörr, Veit Helm, Daniel Steinhage, Ralph Timmermann, and Angelika Humbert. 2024. "Extreme Melting at Greenland's Largest Floating Ice Tongue." The Cryosphere 18(3):1333–57. doi:10.5194/tc-18-1333-2024.

Zhang, Wensong, Kang Yang, Laurence C. Smith, Yuhan Wang, Dirk van As, Brice Noël, Yao Lu, and Jinyu Liu. 2023. "Pan-Greenland Mapping of Supraglacial Rivers, Lakes, and Water-Filled Crevasses in a Cool Summer (2018) and a Warm Summer (2019)." Remote Sensing of Environment 297:113781. doi:10.1016/j.rse.2023.113781.

Zheng, Lei, Lanjing Li, Zhuoqi Chen, Yong He, Linshan Mo, Dairong Chen, Qihan Hu, Liangwei Wang, Qi Liang, and Xiao Cheng. 2023. "Multi-Sensor Imaging of Winter Buried Lakes in the Greenland Ice Sheet." Remote Sensing of Environment 295:113688. doi:10.1016/j.rse.2023.113688.

Zhou, Quan, Qi Liang, Wanxin Xiao, Teng Li, Lei Zheng, and Xiao Cheng. 2025. "Supraglacial Lake Depth Retrieval from ICESat-2 and Multispectral Imagery Datasets." Journal of Remote Sensing. doi:10.34133/remotesensing.0416.

# Appendix A. Supplementary figures for Chapter 2

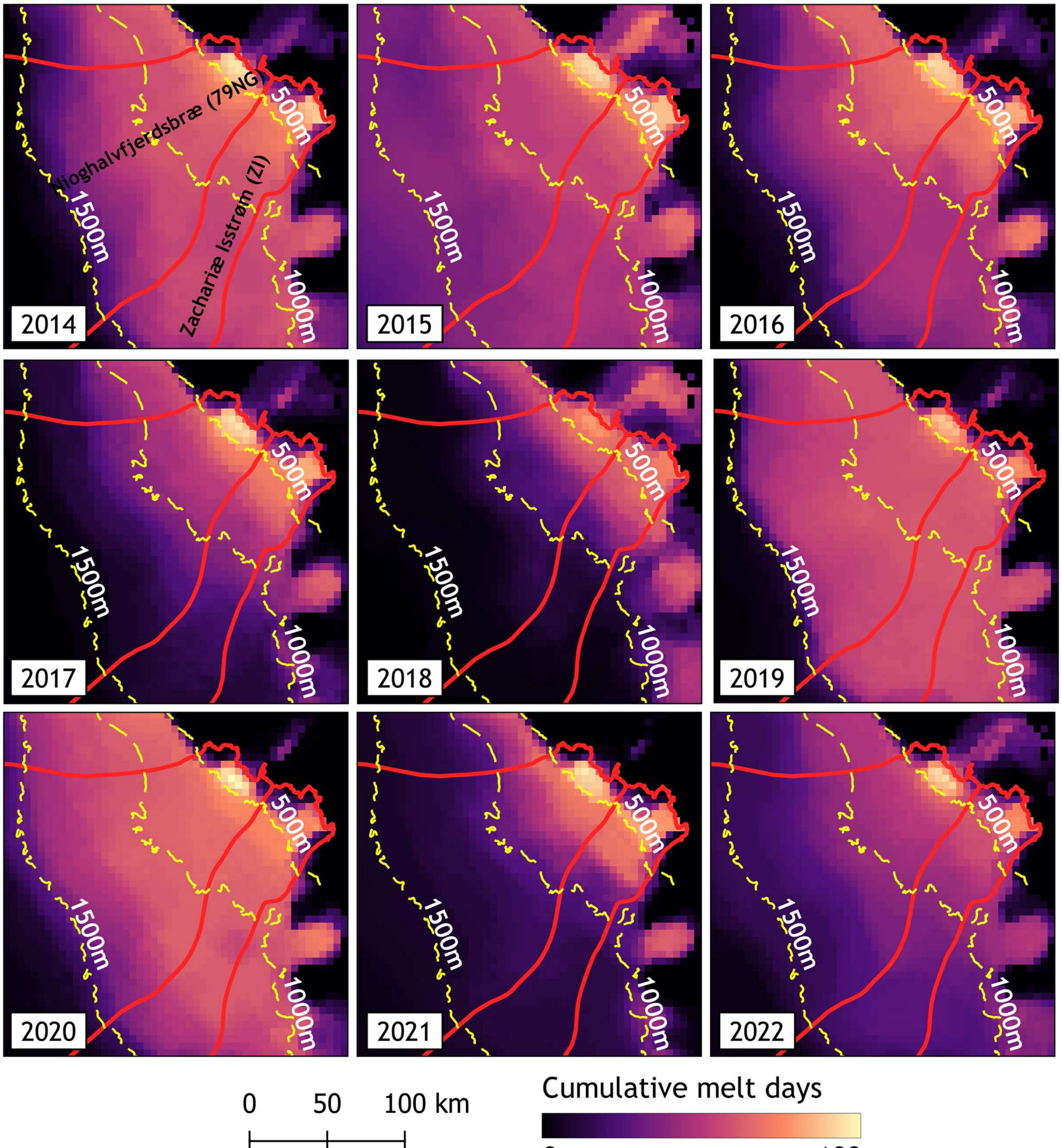


**Figure A.1.** Maps of melt intensity (cumulative melt days between 1 June and 31 August) for Nioghalvfjerdsbræ (79NG) and Zachariæ Isstrøm (ZI) derived from ASCAT data.

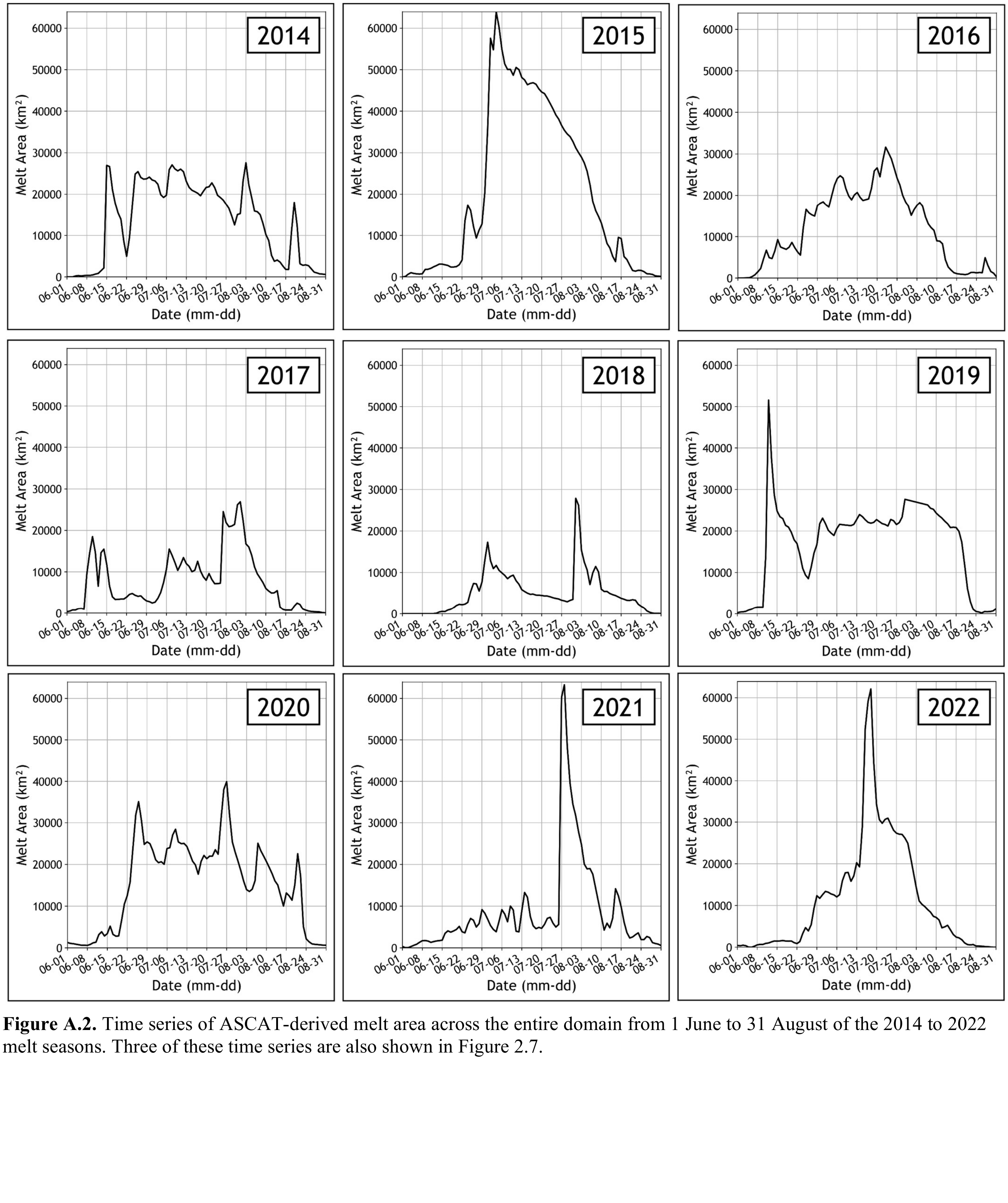


**Figure A.2.** Time series of ASCAT-derived melt area across the entire domain from 1 June to 31 August of the 2014 to 2022 melt seasons. Three of these time series are also shown in Figure 2.7.

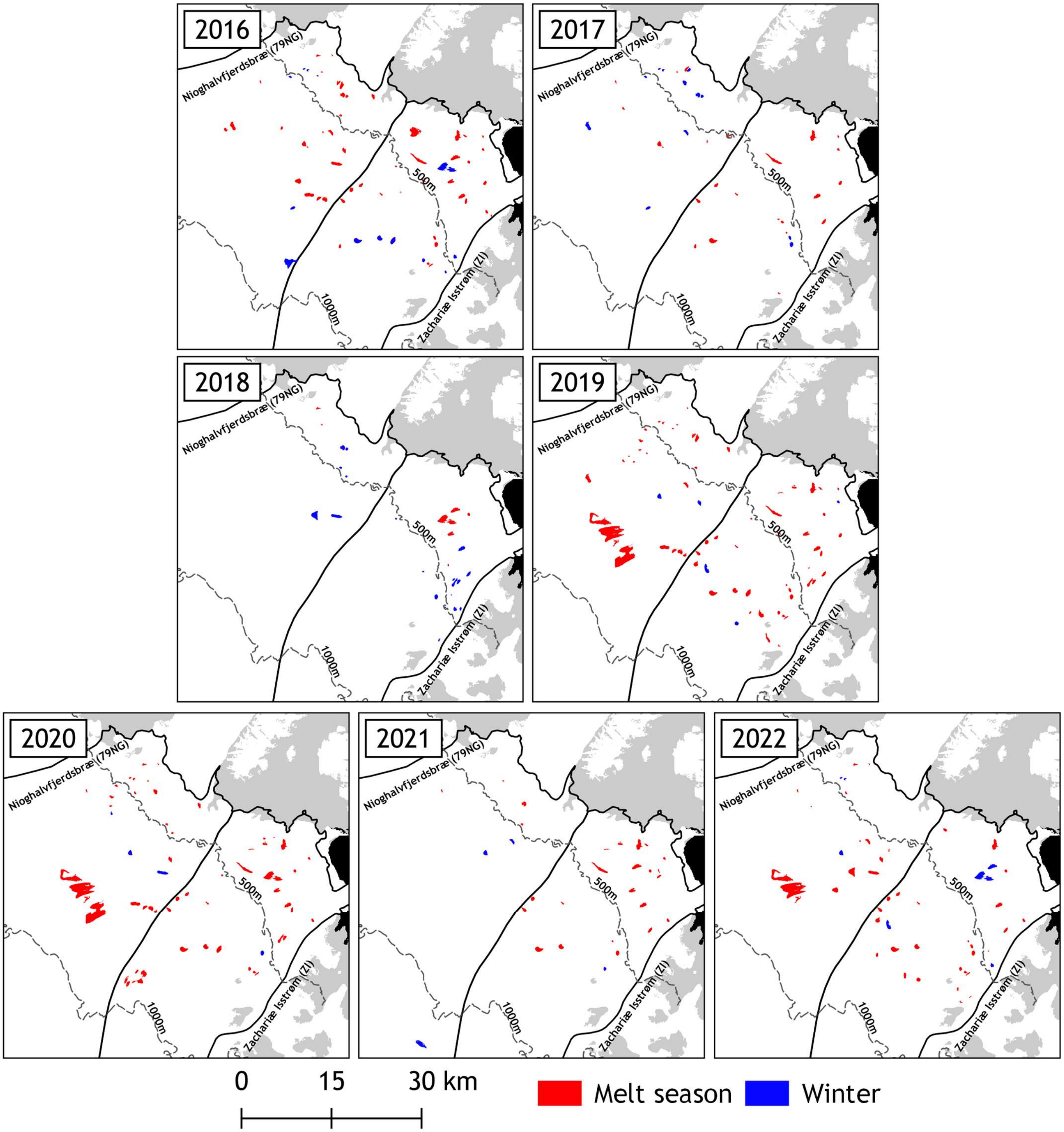


**Figure A.3.** Locations of melt season (red polygon) and winter (blue polygon) rapid drainages from 2016 to 2022. Melt season rapid lake drainages are from Lutz et al., (2025). Gray shading indicates land areas, and black represents an ocean mask, both derived from the GIMP lake, ice, and ocean classification dataset (Howat, 2017).

# Appendix B. Supplementary figures for Chapter 3

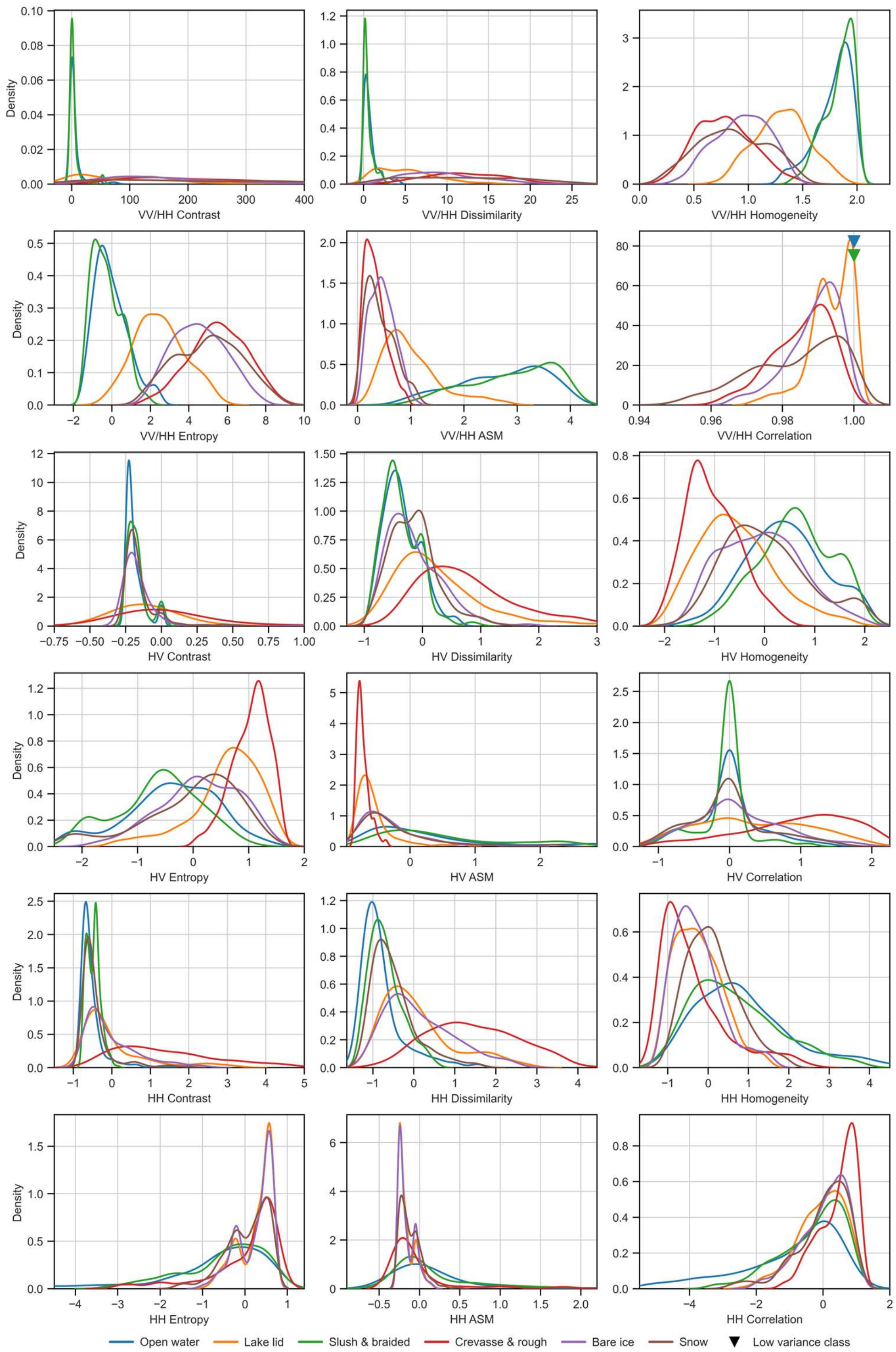


**Figure B.1.** Probability density curves for six GLCM texture metrics including contrast, dissimilarity, homogeneity, entropy, ASM, and correlation, derived from C-band RCM backscatter acquired on 12 July 2024. Rows are grouped by input backscatter type including VV divided by HH, HV, and HH. Colored lines represent the six surface classes: open water, lake lid, slush and braided, crevasse and rough, bare ice, and snow. Black triangles indicate classes with low variance in a given texture metric.

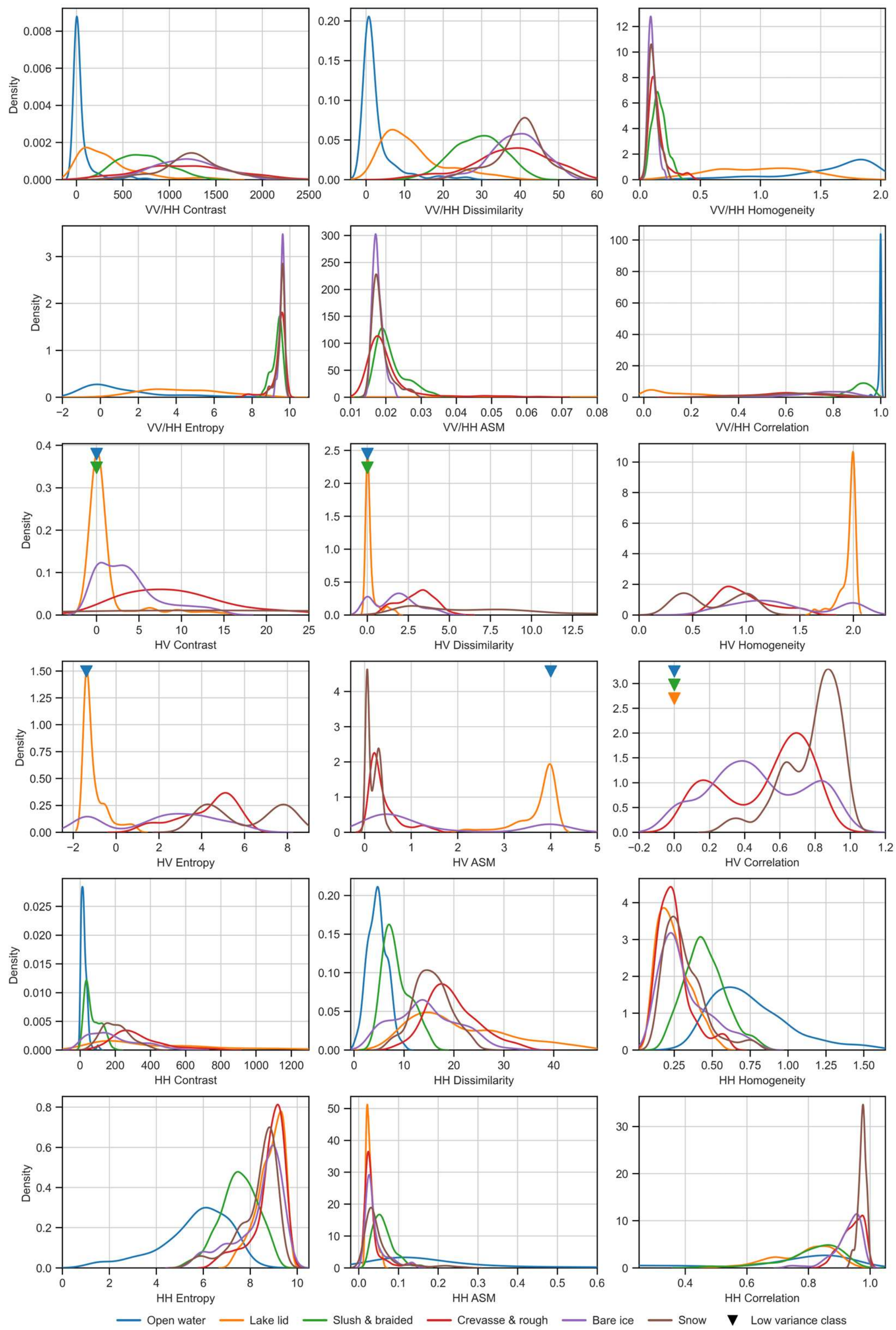


**Figure B.2.** Probability density curves for six GLCM texture metrics including contrast, dissimilarity, homogeneity, entropy, ASM, and correlation, derived from L-band SAOCOM backscatter acquired on 12 July 2024. Rows are grouped by input backscatter type including VV divided by HH, HV, and HH. Colored lines represent the six surface classes: open water, lake lid, slush and braided, crevasse and rough, bare ice, and snow. Black triangles indicate classes with low variance in a given texture metric.

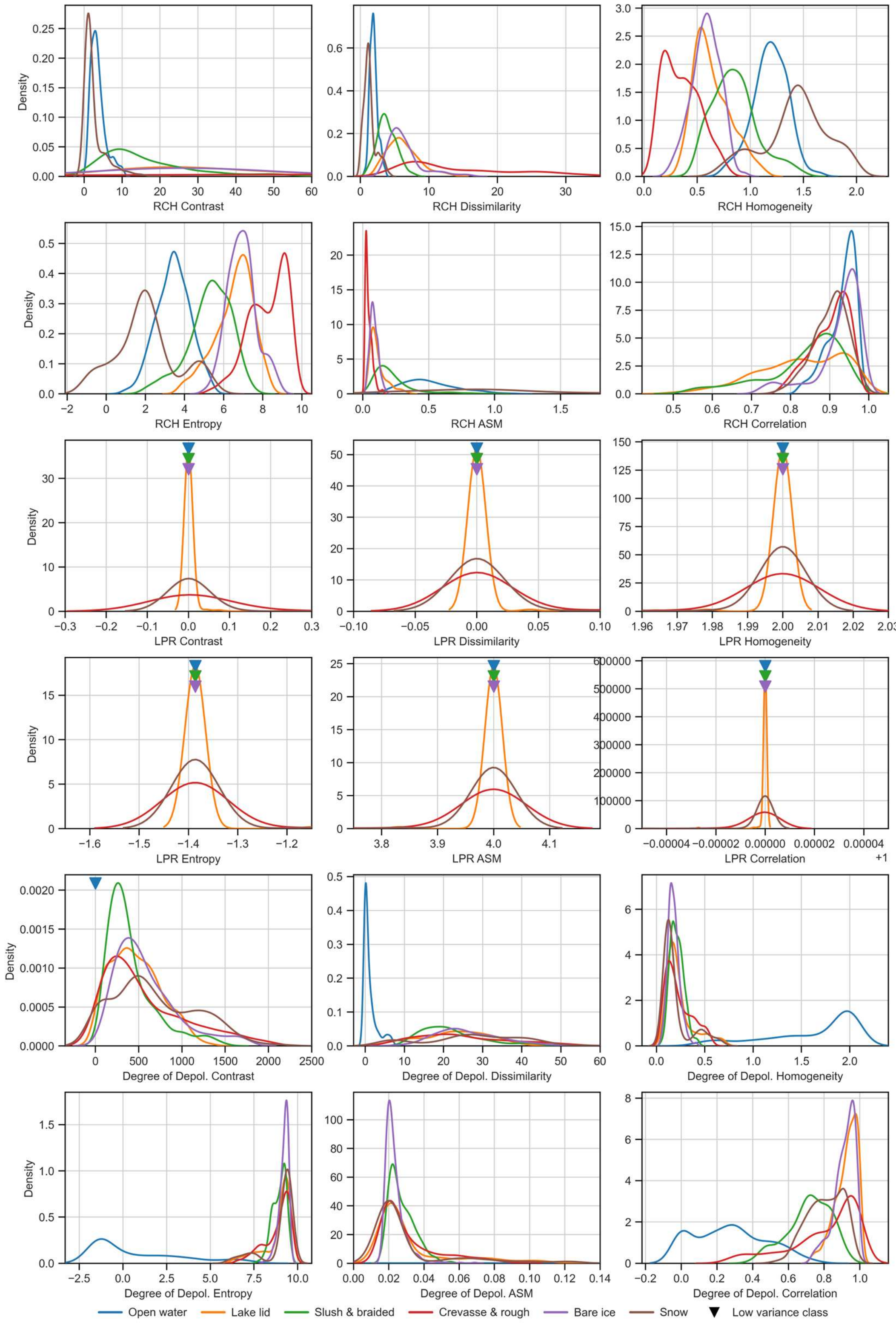


**Figure B.3.** Probability density curves for six GLCM texture metrics including contrast, dissimilarity, homogeneity, entropy, ASM, and correlation, derived from C-band RCM compact polarimetric image acquired on 21 July 2024. The first two rows show textures calculated from RCH, the next two rows show textures from the LPR, and the final two rows show textures from DoD. Coloured lines represent the six surface classes open water, lake lid, slush and braided, crevasse and rough, bare ice, and snow. Triangles indicate classes with very low texture variance.

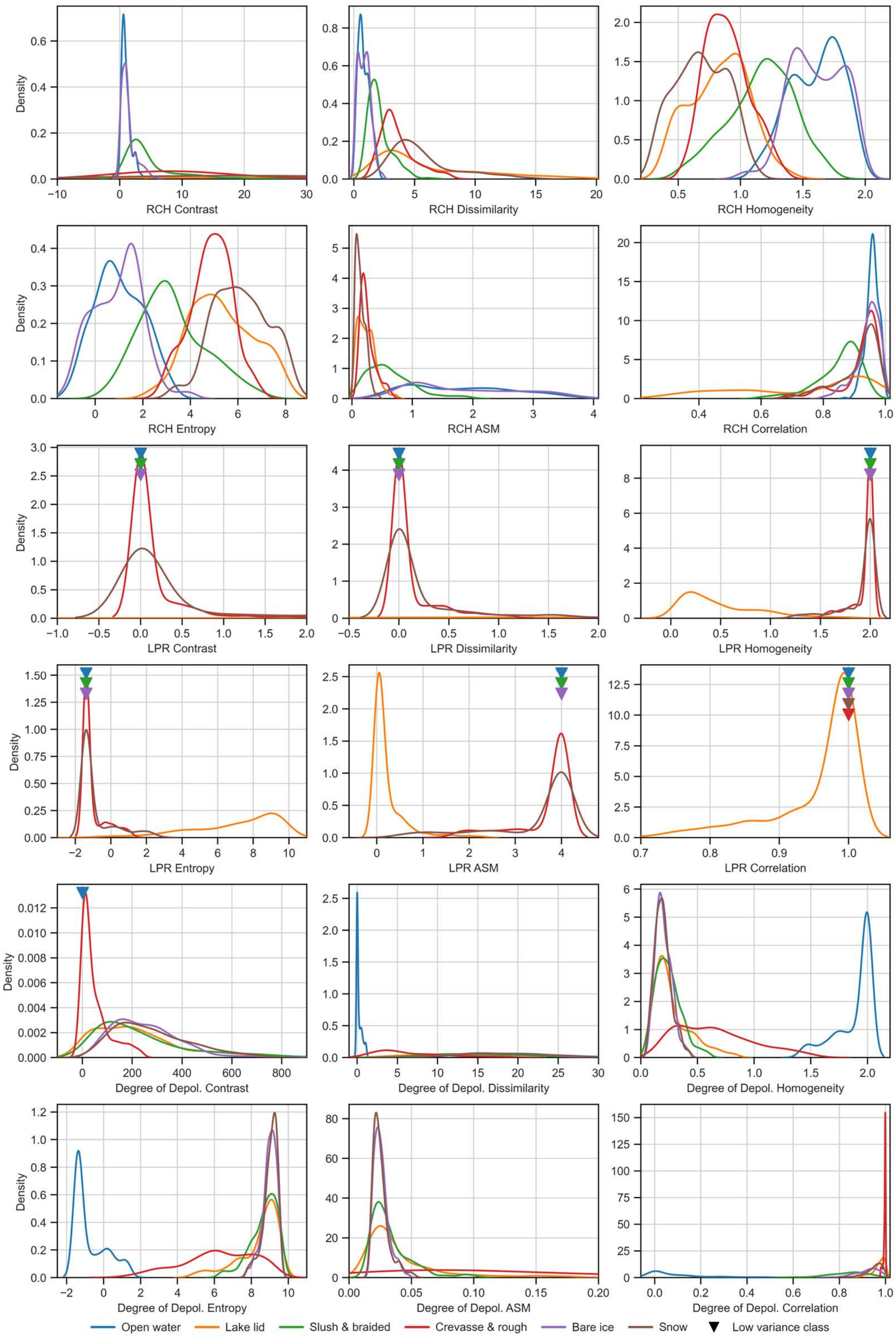


**Figure B.4.** Probability density curves for six GLCM texture metrics including contrast, dissimilarity, homogeneity, entropy, ASM, and correlation, derived from L-band SAOCOM simulated compact polarimetric image acquired on 21 July 2024. The first two rows show textures calculated from RCH, the next two rows show textures from the LPR, and the final two rows show textures from DoD. Coloured lines represent the six surface classes open water, lake lid, slush and braided, crevasse and rough, bare ice, and snow. Triangles indicate classes with very low texture variance.

## Data acknowledgments

I would like to thank Alexander Komarov from Environment and Climate Change Canada for supplying and aiding with the tasking of RCM images used in the Chapter 3 analysis. SAOCOM-1 SAR data © CONAE 2024, was provided by the European Space Agency under ESA's SAOCOM Announcement of Opportunity.

## Chapter 2 author contributions

I led the conceptualization of the study. R. Scharien supported both the conceptualization and the methodology, and I. Willis contributed to the conceptualization. I carried out all data processing and formal analysis, with guidance from K. McDougall on processing and analyzing the ASCAT data. R. Scharien and I. Willis reviewed and edited the original draft.

## Chapter 3 author contributions

I led the conceptualization of the study. R. Scharien, as principal investigator, aided with preparation of the ESA Third-Party Mission proposal for SAOCOM-1 data and supported the study's conceptualization and methodology. R. Dell provided guidance in developing the methodology. I performed the data processing and formal analysis. R. Scharien reviewed and edited the original draft.